Surface Pressure Measurements Using Coaxial Volumetric Velocimetry

K. Patil

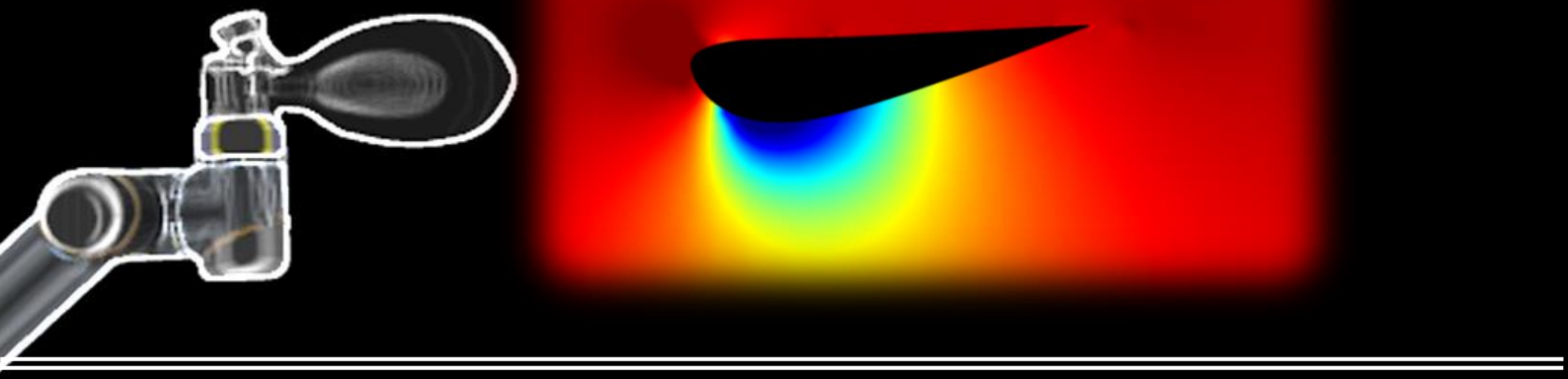

TU Delft

Surface Pressure Measurements using Coaxial Volumetric Velocimetry

Investigation on an Inverted Wing in Ground Effect

by

K. Patil

to obtain the degree of Master of Science
at the Delft University of Technology,
to be defended publicly on Monday April 29, 2019 at 02:00 PM.

Student number:	4614372	
Project duration:	May 1, 2018 – April 29, 2019	
Thesis committee:	Dr. Ir. B. W. van Oudheusden,	TU Delft, chair of assessment committee
	Dr. A. Sciacchitano,	TU Delft, supervisor
	Dr. D. Ragni,	TU Delft, committee member
	Ir. E. Saredi,	TU Delft, daily supervisor

TU Delft

Preface

"Never give up"

The words defining my journey so far, as I finish this project and my M.Sc. studies. These last couple of years were challenging, but allowed me to grow the most and taught me a lot more than just aerodynamics. Often, times were difficult but there were people always ready to help and the following is my expression of gratitude towards them.

Firstly, I want to thank *Dr. Andrea Sciacchitano* for his support and valuable guidance throughout the project. Through our various interactions, I got to learn a lot about experimental aerodynamics, but more than that, about the sort of human I want to become. I also thank *Edoardo Saredi* for his advice and sharing his expertise during the experiments. I also extend my thanks to *Constantin Jux* for sharing his valuable knowledge and expertise. I also express my sincere gratitude towards *Peter Duyndam, Dennis Bruikman, Nico van Beek, Stefan Bernardy, Frits Donker Duyvis and Colette Russo* for their help throughout the project.

Looking back, coming to Delft indeed was a step into the unknown and tough in many ways. But I want to specially thank *Rahul*. From flatmates to brotherhood, thanks for keeping my spirits high. And similarly for those who were there to help whenever I called: *Saurabh, Raj and Shantanu*; thank you for your support. I am also glad and thankful to meet a few amazing people in Delft; specially *Francesco Mitrotta* for always keeping things cheerful and *Yuyang Luan* for the ever-interesting chats. Also, being an introvert, I spent a lot of time just staying indoors finding ways to relax watching YouTube and I want to particularly thank *Felix Kjellberg*, more commonly known as *PewDiePie*. Your videos have always brightened my mood and were the best way to take a break.

Finally, and most importantly, all of this would not have been possible without the constant support and love from my parents: *Sunil and Surekha*. My sincerest gratitude for always supporting me and believing in me to achieve my ambitions.

K. Patil
Delft, April 2019

Abstract

In experimental aerodynamics, pressure is an important parameter which provides insight into the various features of the flow around the test object. By obtaining the surface pressure information, various inferences can be drawn such as flow separation, local flow velocity etc. Traditionally, the most common method of obtaining pressure has been through direct measurements by incorporating the test model with pressure taps, which makes the model expensive and complicated. However, often there arises a requirement to obtain qualitative information and visualise the aerodynamic features during the test. Particle Image Velocimetry (PIV) solves provides this qualitative information as well as quantitative information in the form of a flow field. Pressure can be further computed using this velocity field. This technique holds a number of advantages over traditional wind tunnel measurements, especially with reduction in resources for manufacturing, ease of handling and non-intrusiveness. However, the conventional PIV technique came with the disadvantage of only having 2D2C information. Other techniques like stereo PIV and tomographic PIV were developed to tackle these limitations and the most recent development was that of Coaxial Volumetric Velocimetry (CVV). Along with the advent of Helium Filled Soap Bubbles (HFSB), this novel technique allows for large scale 3D3C measurements. This research is conducted to assess the feasibility of this promising technique to obtain surface pressure.

The flow field around an inverted wing in ground effect is investigated using CVV by robotic manipulation. Using HFSB as tracer particles, the experiment was carried out in the W-Tunnel of TU Delft. The wing was tested at two angles of attack, $\alpha = 5^\circ$ and $\alpha = 8^\circ$ and three ground clearance configurations ($h/c = 1, 0.6$ and 0.3 at $\alpha = 5^\circ$) at airspeed of 10 m/s. The wing is equipped with a total of 30 surface pressure taps along the chord-wise direction, both on the pressure and suction side. The velocity field is obtained using Lagrangian particle tracking algorithm, *Shake-the-Box* and time-averaged velocity field is obtained by ensemble averaging of the obtained particle tracks. Static pressure is calculated using Poisson's equation using the information obtained from velocity field. The pressure thus obtained is then compared with the readings obtained from pressure taps.

Such an assessment not only shows the feasibility of the technique but also highlights the shortcomings and potential improvements. To the best of the author's knowledge through a literature study, this particular technique has not been used to obtain surface pressure information. Most of the work published in the field of CVV is to study flow features, mostly in the wake. Hence, it is expected that this research and the recommendations help to further development of such a technique in the future.

List of Tables

List of Figures

Nomenclature

Abbreviations

CCD	Charge Coupled Device
CFD	Computational Fluid Dynamics
CMOS	Complementary Metal-Oxide Semiconductor
CPU	Central Processing Unit
CVV	Coaxial Volumetric Velocimetry
DEHS	Di-Ethyl-Hexyl-Sebacat
ESA	European Space Agency
FSS	Full Scan Span
FSU	Fluid Supply Unit
HFSB	Helium Filled Soap Bubbles
HSC	High-accuracy Silicon Ceramic
IPR	Iterative Particle Reconstruction
MART	Multiplicative Algebraic Reconstruction Technique
MFG	Multiplicative First Guess
NASA	National Aeronautics and Space Administration
OTF	Optical Transfer Function
PIV	Particle Image Velocimetry
ppp	Particle per pixel
PSP	Pressure Sensitive Paints
PTU	Programmable Timing Unit
PTV	Particle Tracking Velocimetry
RAM	Random Access Memory
SSD	Solid State Disk
STB	Shake-the-Box
TRL	Technology Readiness Level

Symbols

α	Angle of attack	[°]
β_0	Tomographic aperture	[°]
β_x	X tomographic aperture	[°]

β_y	Y tomographic aperture	[°]
Δpx	Pixel pitch	$[\mu m]$
ϵ_x	Positional uncertainty along X-axis Positional	$[mm]$
ϵ_y	Positional uncertainty along Y-axis Positional	$[mm]$
ϵ_z	Positional uncertainty along Z-axis Positional	$[mm]$
λ	Wavelength of laser	$[nm]$
μ	Dynamic Viscosity	$[kg/s.m]$
ϕ	Angle of view	[°]
ρ_f	Fluid density	$[kg/m^3]$
ρ_p	Particle density	$[kg/m^3]$
σ	Standard deviation	$[-]$
b	Bit depth of sensor	$[bit]$
c	Chord	$[mm]$
C_A	Coefficient of axial force	$[-]$
C_L	Coefficient of Drag	$[-]$
C_L	Coefficient of Lift	$[-]$
C_N	Coefficient of normal force	$[-]$
C_P	Coefficient of Pressure	$[-]$
C_S	Scattering cross-section	$[m^2]$
d_p	Particle diameter	$[\mu m]$
d_z	Reconstructed in-depth particle size	$[mm]$
f	Acquisition frequency	kHz
$f_\#$	Numerical aperture	$[-]$
f_l	Focal length	$[mm]$
I_P	Intensity of light scattered by particles	$[counts]$
I_{min}	Minimum detectable intensity	$[counts]$
M	Magnification	$[-]$
p	Static pressure	$[Pa]$
p_0	Total pressure	$[Pa]$
q	Dynamic pressure	$[Pa]$
u	Velocity in X-direction	$[m/s]$
U_{slip}	Slip velocity	$[m/s]$
v	Velocity in Y-direction	$[m/s]$
w	Velocity in Z-direction	$[m/s]$
z_{max}	Maximum imageable distance	$[mm]$
z_{sat}	Distance at which sensor is saturated	$[mm]$

Contents

1

Introduction

When Francis H. Wenham designed the first wind tunnel in 1871, he inadvertently started a revolution in aerodynamic studies. The wind tunnel was a solution to test and simulate real life conditions in a controlled environment. In the next century, it enabled a plethora of aviation research and humans could design, test and build airplanes. But being humans, driven by curiosity and hunger to know more, wind tunnels soon were being used to study and test aerodynamics of buildings, automotive, motorsports, sports etc.

In a typical wind tunnel test, many parameters are measured using different techniques and instruments. Most commonly, the forces and moments acting on the test model are measured using a balance. Often in aerodynamic development, the geometry or problem in consideration is developed using computational simulations in the initial phases. After a number of iterations developed using CFD, the validation is done in a wind tunnel test. Often it is the case that there is a mismatch between the results of CFD simulations and wind tunnel test data. This is mainly due the fact that in CFD, the flow is 'modelled', whereas wind tunnel testing is closer to 'real-life' conditions. To understand the differences, it is necessary to study the flow features on the different parts of the model. For visualizing the airflow, various techniques like smoke visualisation, oil flow visualisation, woolen tufts, schlieren etc. are commonly used. However, such techniques only give qualitative insight, raising the necessity of quantitative measurements.

1.1. Pressure Measurements in Aerodynamics

One of the most frequently measured parameters, is pressure. By measuring pressure, one can obtain other information like velocity of air, mass flow rate etc. This helps to determine the test conditions in the wind tunnel. The information of surface pressure also is helpful in understanding flow features like flow separation. Not only this information is useful in validating the CFD simulations as mentioned above, but also can be used to calibrate the CFD models and improve further simulations. By integrating the surface pressures, one can also estimate the loads acting on the surface. Apart from surface pressure, pressure measurement is also used to study the wake structure, typically by measuring total pressure.

To measure the pressure at a point in the flow, the most common device is the Pitot tube. By placing these tubes are locations of interest, one can obtain dynamics and static pressure at that point. This can be useful to understand the flow characteristics at that point. For instance, the flow velocity can be obtained from the dynamic pressure. However, the most significant measurements are that of the static pressure, to obtain flow phenomenon affecting the model. In Fig. 1.1, the surface pressure distribution on the upper and lower side of a $\frac{1}{4}^{th}$ scale model of a a sedan based race car is shown. Looking at the pressure distribution, one can understand flow phenomenon like stagnation near the nose, large suction produced by front wing, suction produced by the roof, separation in the wake etc.

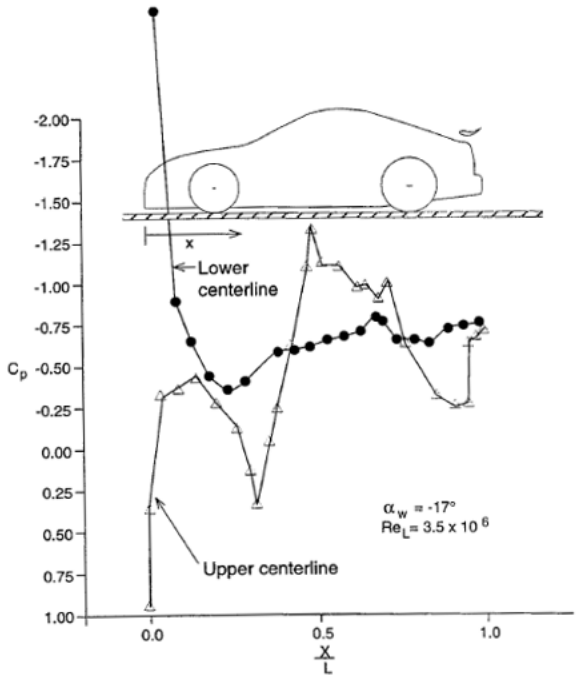

Figure 1.1: Pressure distribution on the center-line of a sedan-based race car, duplicated from Katz, (1995)

These measurements are typically done using various transducers like strain gauge transducers, piezoelectric transducers, pneumatic transducers, electronic transducers etc. The detailed working principles of these can be found in Russo, (2011). The most conventionally used are pressure taps or orifices on the surface of the model. These orifices are connected to electronic pressure transducers using thin flexible tubes. These are typically of the size of $0.4\mu m$-$0.6\mu m$ (Fig. 1.2b). A representation of the mounting of the pressure taps is shown in Fig. 1.2a. Compared to the other transducers, these are more versatile and accurate to use. High frequency (of the order of $\mathcal{O}$(10kHz)) pressure recording is also possible and is only limited by the acquisition frequency of the transducer.

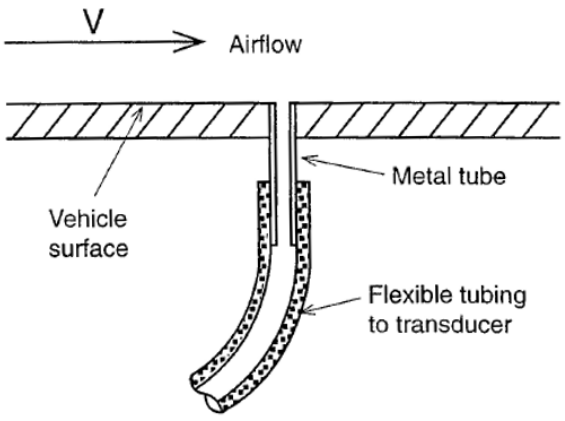

(a) Schematic representation of a pressure tap mounted on a vehicle, duplicated from Katz, (1995)

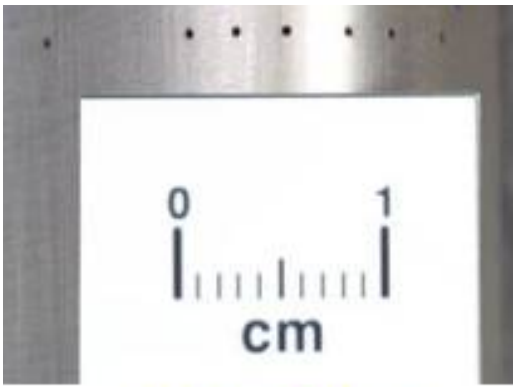

(b) Wind tunnel model showing the pressure taps on the surface along with a scale for reference, adapted from www.nasa.gov

Figure 1.2: Illustration of mounting of pressure taps

However, these taps need to be built into the model in pre-determined locations. These locations cannot be in close proximity and hence limit the spatial resolution of the pressure distribution. Apart from that, these orifices need to be designed carefully, considering that they do not affect the flow and subsequently the pressure measurements. Being on the surface, they are prone to getting clogged by

dirt and hence need to be cleaned from time to time. The tubes connecting the taps to transducer need to be handled carefully as they are delicate and can be damaged easily. Also, they have issues like tangling and are hassle to handle.

Figure 1.3: Wind tunnel model of an aircraft wing, showing the bunch of tubes connecting surface pressure taps to transducers

Considering these problems, an ideal solution would be to have completely non-intrusive measurement of pressure. One such technique is use of Pressure Sensitive Paints[1]. The working principle for PSP is based on the phenomenon of oxygen sensitivity of certain photo-luminescent materials applied like a paint-like coating. In such materials, when excited by a suitable radiation, photons with a different wavelength are emitted through a phenomenon called oxygen quenching. The intensity of this produced luminescence varies inversely with oxygen partial pressure, which in turn is directly related to air pressure as the mole fraction of oxygen in air is fixed. By taking images of this produced luminescence, the pressure distribution on the surface can be obtained through image processing. For this, however, the system needs to be properly calibrated. The detailed procedure and an overview of PSP is explained by McLachlan and Bell, (1995) and Nakakita et al., (2006).

(a) An aircraft model coated woth PSP (pink) mounted in the wind tunnel at NASA's Ames Research Center, duplicated from `www.nasa.gov`

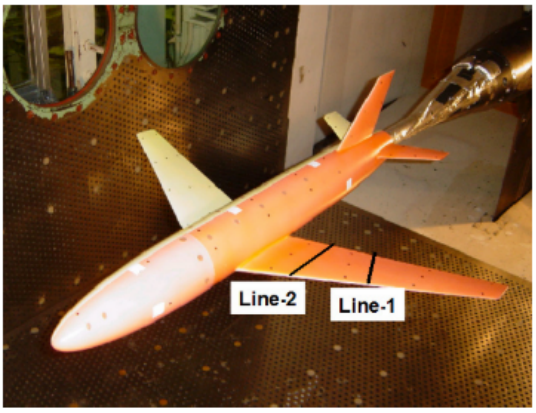

(b) ONERA M5 model coated with PSP, duplicated from Nakakita et al., (2006)

Figure 1.4: Wind tunnel models coated with PSP

Comparing with pressure taps, PSP have a number of advantages. The most significant being the spatial resolution. Pressure taps provide data only at specific points of the model whereas PSP can provide the pressure distribution on the entire surface of the model. Without, the need of building the

[1]hereafter referred to as PSP

pressure taps into the model, the model design can be much simpler. It will also cost a fraction as the pressure taps and ancillaries need to be built into every iteration of the wind tunnel model. With PSP, it is simply a matter of spraying the model with the coating. Fig. 1.5 shows the surface pressure contours obtained from PSP, compared against those obtained from CFD simulation.

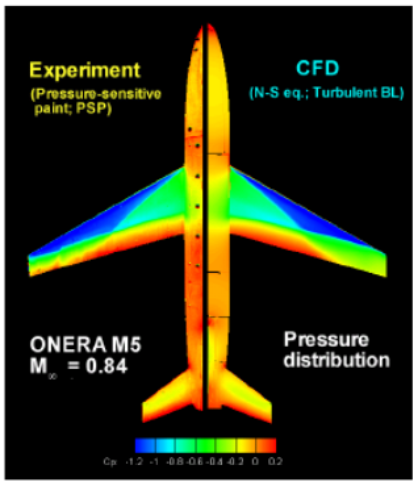

Figure 1.5: Comparison of pressure contours obtained from PSP(left) with CFD(right), duplicated from Jahanmiri, (2014)

Even though PSPs will improve productivity, they still have several limitations. The most important being high uncertainty in measuring pressure at low Mach number flows. This is because, at low speeds, the difference between the oxygen quenching in wind off and wind on conditions is very low and hence difficult to measure. In the context of this thesis, where the flow speeds will be as low as $10 m/s$, PSP are very undesirable in comparison to pressure taps. In flows with higher Mach numbers (transonic or supersonic), where the surface temperature of the model changes significantly, the use PSPs becomes even more difficult as the temperature has an effect on the energy state of the coating affecting the oxygen quenching process. Extra care also needs to be taken during the application of the coating in the sense that the coating does not cause problems of intrusiveness. Being directly applied on the surface, they can affect the aerodynamic characteristics of the model. Such coatings also undergo photo-degradation and their response time to excitation increases, limiting the useful time of the coating on the model.

An excellent technique which has advantages in the above aspects is Particle Image Velocimetry[2]. It is an optical technique and is non-intrusive. It is versatile and cost-efficient in the long run. The principles and its applications are discussed in Chapter 2. Images of tracer particles introduced in the flow, passing through a thin laser[3] sheet can be captured and processed, giving a 2D velocity field. This field can be then processed to obtain the static pressure field. The main drawback however, is the techniques ability to provide only planar and 2D information. In most modern day applications, the flows encountered are largely 3D in nature. Conventional PIV becomes inadequate or time consuming as the volume has to be divided into multiple planes and then stitched together. In highly turbulent regions, it also fails to capture the out of plane velocity components.

To solve this issue of volumetric measurements, Elsinga et al., (2006) developed the technique of tomographic PIV. It is a technique which involves at least three cameras and a relatively complex setup. The processing of the obtained images is also computationally expensive. The volume that can be measured is of the order of $\mathcal{O}(10\ \mathrm{cm}^3)$. Another limiting factor was the light scattering intensity of tracer particles. However, the introduction of Helium Filled Soap Bubbles[4] for large scale volumetric PIV applications by Scarano et al., (2015) enabled rapid expansion in size of measurement volumes of the order of $\mathcal{O}(50\ \mathrm{l})$. The HFSB are efficient in scattering light and hence illumination intensity required is much lower. However, tomographic PIV is insufficient to analyse flows around complex models where optical access is limited. The change in orientation of the cameras produces the need to re-calibrate

[2]hereafter referred to as PIV
[3]abbreviation for 'Light Amplification by Stimulated Emission of Radiation'
[4]hereafter referred to as HFSB

the system, which is a long procedure.

The desire to measure large volumes around complex geometries with the versatility of spatial manipulation led to Coaxial Volumetric Velocimetry[5]. The CVV probe with four cameras and illumination source mounted co-axially, is described in detail in Section 3.4.1. For easy and quick manipulation, the probe is mounted on a robot arm, described in Section 3.4.3. This allows to scan a domain by dividing it multiple volumes and obtain 3D velocity field. In this case, Particle Tracking Velocimetry[6] was used to generate the velocity field. The obtained velocity field can be further processed to obtain a pressure field using the Poisson equation. The methodology and theory behind these is explained in Chapter 2. This technique is the core of this thesis with the research objective:

"Assess the feasibility of obtaining surface pressure using Coaxial Volumetric Velocimetry"

To satisfy this objective an experimental campaign was carried out. The test model was an inverted wing in ground effect, with constant span-wise cross-section having pressure taps for measuring static pressure. This is of particular interest in the field of motorsports where the wings experience ground effect. Also, the airfoil in general is an excellent test object as it shows deceleration (stagnation) as well as acceleration(suction) and adverse pressure gradient. The experimental setup and procedure is explained in detail in Chapter 3.

The obtained images from the experimental campaign were processed using Davis, a software developed by LaVision GmbH. A novel algorithm called 'Shake-The-Box'[7] is used to generate the particle tracks. The obtained tracks are then binned to obtain time-averaged velocity field. Pressure is reconstructed using this velocity information. This processing and the parameters used are explained in detail in Chapter 4.

In Chapter 5, the relevant data from the processed data is presented in the form of plots, comparisons and buttressed by proper explanations. Ensuring that the research objective has been satisfied an assessment regarding the technique can now be made. To conclude, inferences are drawn and the limitations of the technique are discussed in Chapter 6. The technique looks promising and can be the next industry standard, bearing in mind the current shortcomings of the system. Recommendations are given for further improvement of the system.

1.1.1. Wing in Ground Effect

In this section, the aerodynamics of inverted wing in ground effect is explained. In the context of this thesis, a cambered planar wing is used to obtain surface pressure using CVV. Inverted wings in ground and ground effect in general is extremely important for race cars and performance automotive. On a typical race car, the front wing is very low and hence is in the close proximity of the ground. Ground effect experienced by aircraft wings was studied in the early 20^{th} century. For lifting wings (aircraft), the principle of increased lift is increase in pressure on the pressure side of the wing. a high pressure 'cushion' is formed between the ground and the wing. However, for race cars, the objective of the wing is to generate downforce and hence are installed inverted. In spite of that, these wings experience a similar ground effect. Fig. 1.6 shows how close the front wing of a typical Formula One car is.

[5]hereafter referred to as CVV
[6]hereafter referred to as PTV
[7]hereafter referred to as STB

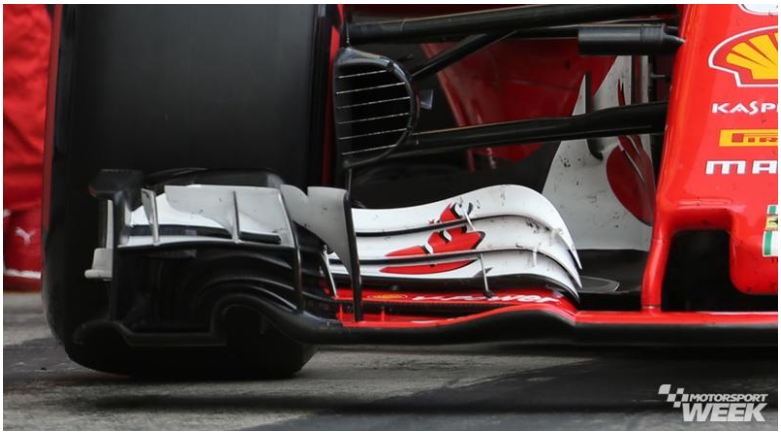

Figure 1.6: Front wing of a Formula One car

The downforce generated by the wing increases with the increase in proximity of the ground. The proximity is often referred as 'ride height' or 'ground clearance'. The aerodynamics of such a wing was studied and explained in Dominy, (1992). When the wing is closer to the ground, the air on the suction side is constrained by the ground and accelerates more than it would without the presence of grounds. This leads to reduced static pressure and increase in suction produced, thus more downforce. As the ride height is reduced, the suction becomes extreme until a point where it can no longer withstand the adverse pressure gradient and the wing stalls. The detailed study of a single element inverted wing in ground effect is presented by Zerihan and Zhang, (2000). The schematic of the experiment is shown in Fig. 1.7.

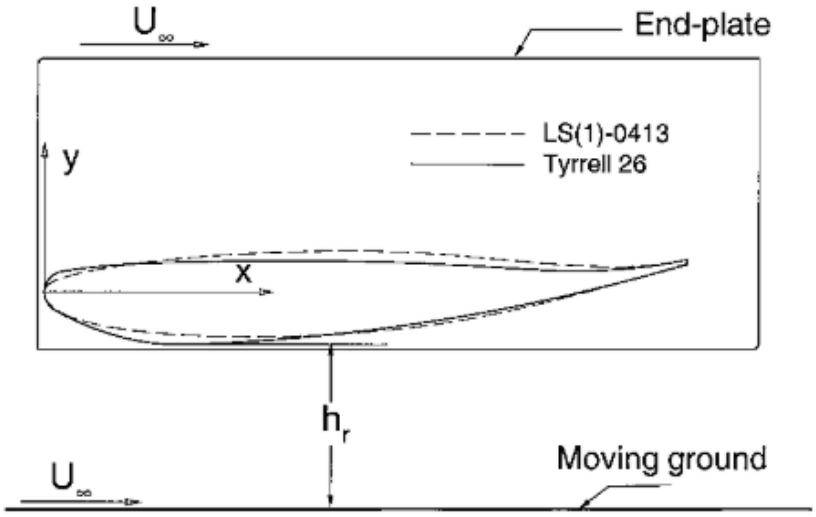

Figure 1.7: Schematic of the setup used for the experiment, duplicated from Zerihan and Zhang, (2000)

The wing was analysed at several angles of attack for various ride heights. The ride height h_r is non-dimensionalized in terms of the chord length c and described as a ratio $\frac{h_r}{c}$. Fig. 1.8 shows the variation of lift coefficient C_L with ride height.

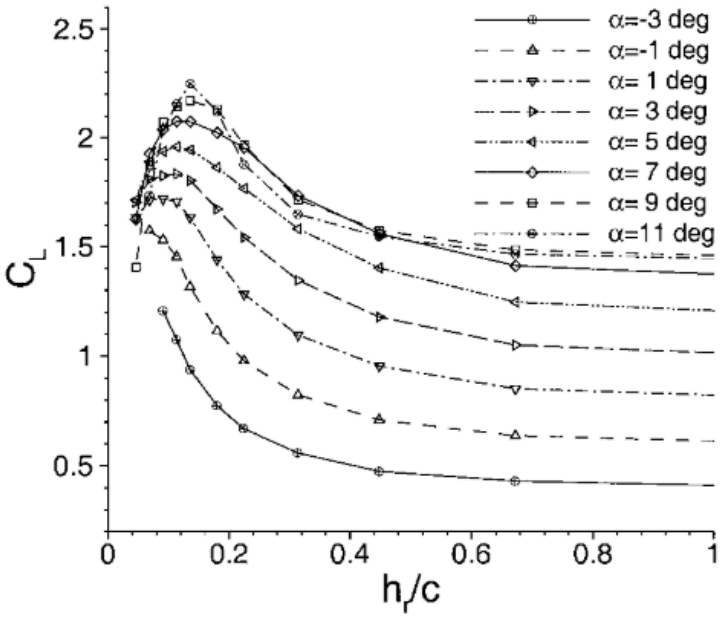

Figure 1.8: Variation of C_L at different angles of attack with change in ride height, duplicated from Zerihan and Zhang, (2000)

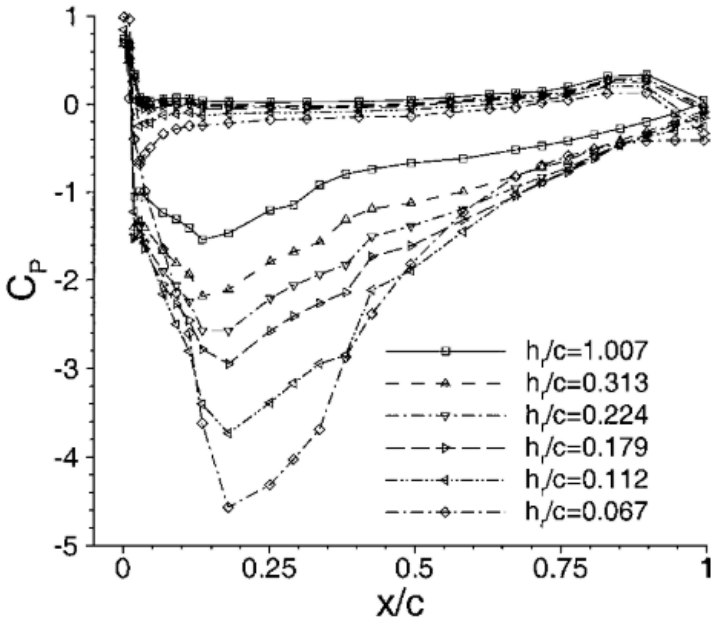

Figure 1.9: Variation of C_P at fixed angle of attack with change in ride height, duplicated from Zerihan and Zhang, (2000)

It is clearly seen from the plot that the C_L produced at any fixed angle of attack shows similar trend. Starting from around $\frac{h_r}{c}$=0.1, the value of C_L increases and a reaches a maximum at around $\frac{h_r}{c}$=0.2. As the $\frac{h_r}{c}$ increases further, the C_L keeps dropping until around $\frac{h_r}{c}$=0.7 after which it remains almost constant. This condition can be deemed similar to the wing facing freestream conditions (no ground effect experienced). The Fig. 1.9 shows the variation of pressure distribution C_P at a fixed angle of attack. It is observed that with reducing $\frac{h_r}{c}$, the suction peak increases extremely but experiences a strong adverse pressure gradient towards the trailing edge.

2

Particle Image Velocimetry - Principles and Applications

Particle Image Velocimetry is an extremely useful and common flow measurement technique widely used for industrial as well as research purposes. A brief overview of the necessities and methods of pressure measurement are presented in the beginning of this chapter. The development of PIV, from conventional planar PIV to tomographic PIV and CVV are explained sufficiently for the reader to have a generic understanding. The methodology of reconstructing pressure from velocity field is explained along with experiments found in literature employing PIV to obtain pressure.

2.1. Planar PIV

The earliest use of PIV dates back to 1977, where three independent research groups Barker and Fourney, (1977),Dudderar and Simpkins, (1977) and Grousson and Mallick, (1977), were using speckle particles illuminated using laser to study fluid motion. This method was further studied at the von Karmann institute by Meynart, (1983) focusing on instantaneous measurements of turbulent flow. However, the term 'Particle Image Velocimetry' was first formulated by Adrian, (1984). He came to the conclusion that in PIV the density of particles was not sufficient to produce a speckle pattern; however individual particles were visible. This sparked the development of PIV and the next twenty years of development have been documented in Adrian, (2005). Raffel et al., (2007) includes all the important stages of development as well as explanations for the technique.

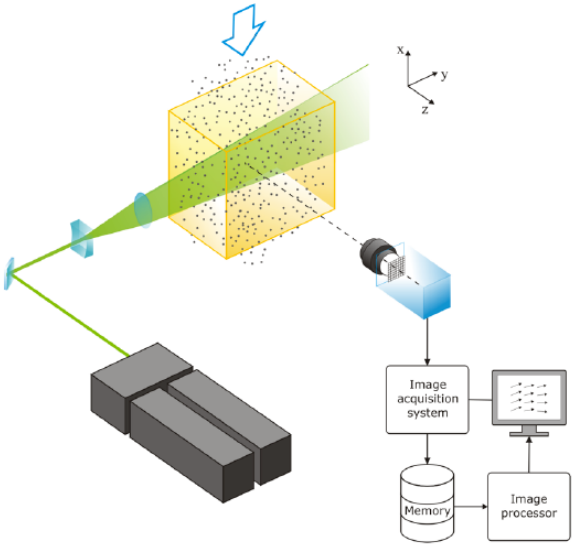

Figure 2.1: Schematic representation of a typical planar PIV setup, duplicated from Scarano, (2013b)

The conventional and most commonly known technique of imaging velocimetry is planar PIV. A schematic representation of a typical planar PIV setup is shown in Fig. 2.1. As the name suggests, the technique is used to measure flow in a plane of interest and provides 2D velocity vectors in that plane. The plane of interest is illuminated by a laser sheet. Tracer particles are introduced in the flow and carried with it. An ideal test particle will be neutrally buoyant and hence follow the flow without having its own effect. These tracer particles while passing trough the laser sheet scatter light. This is recorded by a Charge Coupled Device[1] or Complementary Metal-Oxide Semiconductor[2] sensor cameras. These images are recorded at a known time interval between successive images (frequency). The obtained images are divided into interrogation windows and subjected to cross-correlation analysis. This allows to calculate the average displacement of particles in each window of successive images. Knowing the time interval between these images, we can take the ratio of the displacement and the time interval, to obtain velocity. Being a robust and relatively simple technique, PIV has applications in research wind tunnels as well is an industry standard. However, its biggest shortcoming is that it gives only 2D information of the flow. Hence, for flows of highly turbulent nature, the planar 2D information is insufficient. The particles moving out of the plane are cause issues for cross-correlation. Keeping this limitation in mind, the technique called tomographic PIV was developed and is explained in Section 2.2.

2.2. Tomographic PIV

Tomographic PIV is an approach to measure the flow properties in 3D. The working principle is similar to conventional planar PIV and was devised by Elsinga et al., (2006). It makes use of at least three cameras to take images which are then tomographically reconstructed to find their position in the volume of interest. The setup of tomographic PIV is represented schematically in Fig. 2.2.

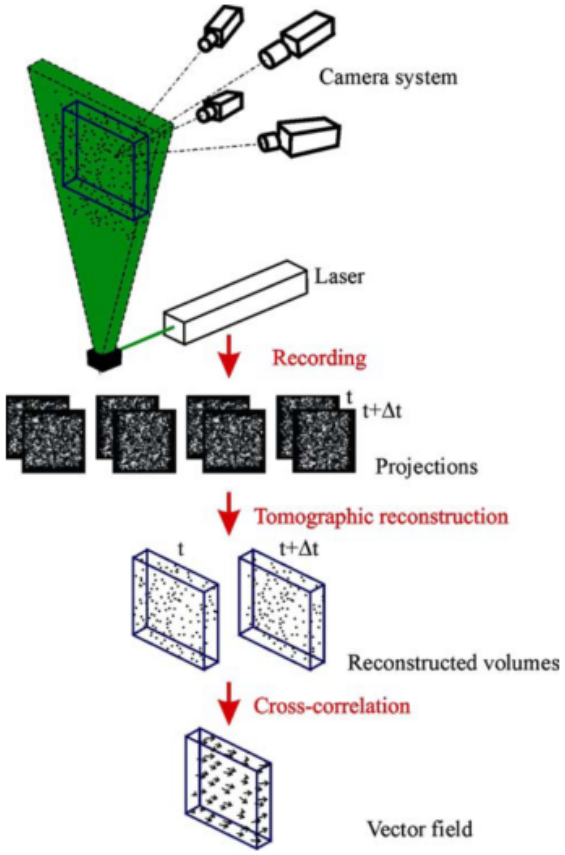

Figure 2.2: Schematic representation of a typical tomographic PIV setup, duplicated from Elsinga et al., (2006)

[1] hereafter referred to as CCD
[2] hereafter referred to as CMOS

The process of tomographic reconstruction of particles is complicated and computationally expensive. The most used method for this is the Multiplicative Algebraic Reconstruction Technique[3], developed by Herman and Lent, (1976). In this approach, the 3D light intensity distribution is computed from 2D image intensities, iteratively. In spite of this problem being underdetermined, MART algorithm works fine and has a good level of accuracy. This approach is the reference for further particle reconstruction methods. However, its biggest pitfall is the computational resources required. In an effort to reduce the resources required, Worth and Nickels, (2008) came up with Multiplicative First Guess[4] MART which improves the first guess of intensity distribution. Another similar approach is the Multiplicative Line of Sight by Atkinson and Soria, (2009). But a major breakthrough in this approach came in 2009, through the work of Wieneke, (2012). In this approach, called Iterative Particle Reconstruction[5], the 3D intensity distribution is calculated using standard triangulation. This is then projected on the 2D images to calculate residual images, providing more information about the particle position. This can be repeated to obtain very accurate positioning as well more and more particles can be triangulated. A flowchart representing this process is shown in Fig. 2.3. Apart from being accurate, this method works very well with high densities of information, necessary to obtain higher spatial resolution.

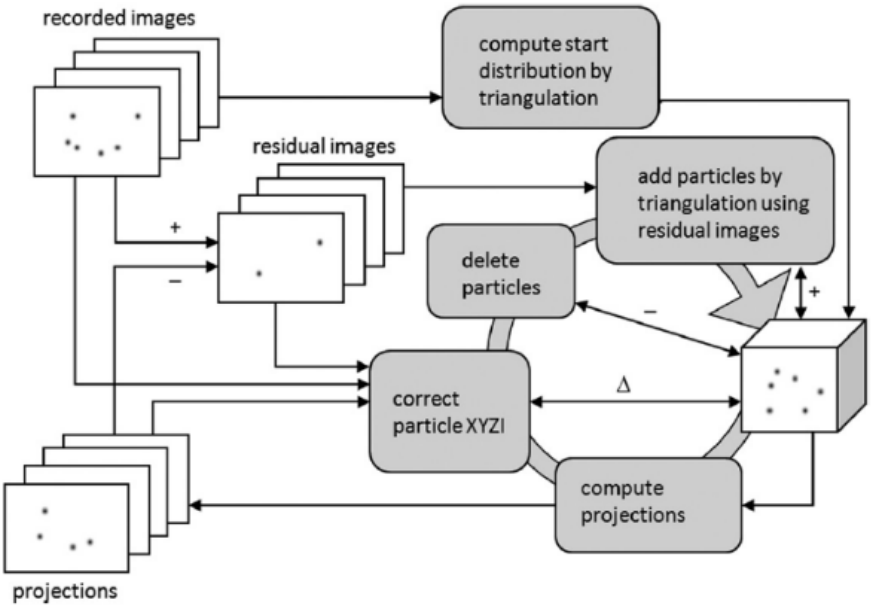

Figure 2.3: Flowchart showing the process of IPR, duplicated from Wieneke, (2012)

In spite of being state-of-the-art of volumetric PIV, its not adequate for large scale applications and is rarely used outside academic research. Apart from the problems of optical access and computational cost, the measurable volume is limited due to the illumination requirements and the scattering properties of conventional tracer particles.

2.3. Helium Filled Soap Bubbles for Large Scale PIV

As mentioned in Section 2.1, tracer particles are introduced in the flow in order to visualize the flow. These particles scatter light when illuminated by the laser. An ideal tracer particle will have negligible effects on the flow and will follow the flow accurately. This is evaluated by means of slip velocity, U_{slip} as prescribed by Raffel et al., (2007):

$$U_{slip} = -\frac{d_p}{18}\frac{(\rho_p - \rho_f)}{\mu}\frac{dU}{dt} \tag{2.1}$$

[3]hereafter referred to as MART
[4]hereafter referred to as MFG
[5]hereafter referred to as IPR

where d_p is the diameter of particles, ρ_f and ρ_p are the densities of fluid and particles respectively, μ is the dynamic viscosity and $\frac{dU}{dt}$ is the fluid acceleration. The above equation is valid under the assumption that the motion of particles is dominated by viscous forces and hence is only valid for small particles. The lower is the U_{slip}, the better it is for the particles to follow the flow. From Eq. (2.1), it is clear that this can be achieved by lowering d_p and the difference between ρ_f and ρ_p. The parameters ρ_f, μ and $\frac{dU}{dt}$ are properties of the flow. Though it might seem that lowering the d_p is the easiest approach, it is observed that the scattering capability, measured using scattering cross-section C_s is directly proportional to the ratio of particle diameter d_p to wavelength of the laser λ. The effect of particle diameter was studied in detail by Melling, (1997).

The tracer particles used conventionally(aerosol fog) have a typical size of $0.5< d_p <10\mu m$. The most common materials used to generate these particles are DEHS[6], TiO_2, vegetable oils, glycol-water solution etc. However, the low scattering intensity of smaller particles becomes insufficient for volumetric measurements. This is critical especially for large scale volumetric measurements Scarano, (2013). With an aim to solve this problem, Scarano et al., (2015) introduced a novel tracer particle - Helium Filled Soap Bubbles. They are a mixture of air,helium and a solution of water,soap and glycerine. The hardware used for the generation of these bubbles is explained further in Section 3.3. These bubbles have a diameter of approximately $300\mu m$ and a response time[7] of roughly $10\mu s$-$30\mu s$ and have been deemed suitable for large scale volumetric measurements. Due to their larger size, HFSB scatter 10^4-10^5 times more light. These characteristics make HFSB suitable for volumetric measurements in wind tunnels (Scarano et al., (2015)). However, these bubbles have a limitation of production rate, which has an effect on concentration in the volume of interest as explained by Caridi, (2017) and Schneiders, (2017). This limits the use of these HFSB in the conventional PIV technique(cross-correlation) due to decreased spatial resolution and hence they find their applications in PTV more suitable as suggested by Schneiders and Scarano, (2016). Even though the spatial resolution for instantaneous velocity measurements is of the order of the inter-particle distance, for time-averaged measurements, the spatial resolution can be as high as the size of the particles themselves. This can be achieved by simply increasing the size of the temporal ensemble as suggested by Kahler et al., (2012).

2.4. Coaxial Volumetric Particle Tracking Velocimetry

2.4.1. Working Principle

With the intention to solve the other limitation of optical access for tomographic PIV, the robotic CVV technique was developed by Schneiders, (2017). Schematic setup of such an arrangement is shown in Fig. 2.4.

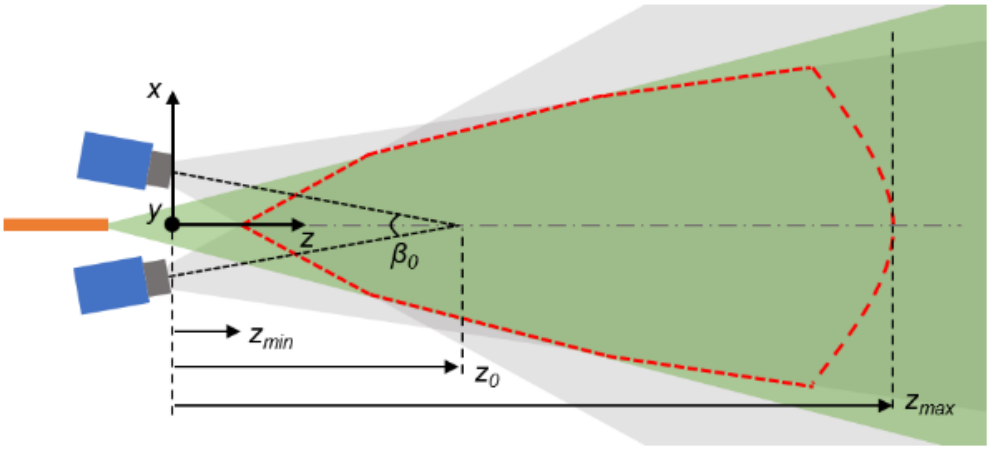

Figure 2.4: Schematic representation of CVV arrangement, showing cameras (blue), field of view (grey), optical fiber (orange), laser illumination (green), duplicated from Schneiders, (2017)

The advantages of such an arrangement are reduction of the tomographic aperture β_0 and a large

[6] abbreviation for Di-Ethyl-Hexyl-Sebacat
[7] This is the time required by the particles to respond to changes in flow velocity

depth of view z_{max}. Also, the cameras being fixed with respect to each other and their arrangement being compact, makes it easier to manipulate the probe using a robot. The parameter β_0 being an order of magnitude lower than tomographic PIV, the optical access of the domain is increased which is also further helped by the ease of robotic manipulation. However, this introduces some disadvantages. As shown by Scarano, (2013), the particle elongates in the diamond-like shape. This is illustrated in Fig. 2.5. Using simple trigonometric relations, give:

$$\frac{d_p}{d_z} \approx tan(\frac{\beta}{2}) \rightarrow d_z \propto \frac{1}{\beta} \tag{2.2}$$

This gives rise to uncertainty in the positioning of in-depth direction as studied in detail by Schneiders, (2017). Utilising the algorithm of Shake-the-Box for lagrangian particle tracking, the positioning of the particle can be improved through polynomial fitting. Schneiders, (2017) and Jux, (2017) found these uncertainties to be around $\epsilon_x = \epsilon_y \leq 0.1mm$ while that in-depth to be $\epsilon_z = 1mm$.

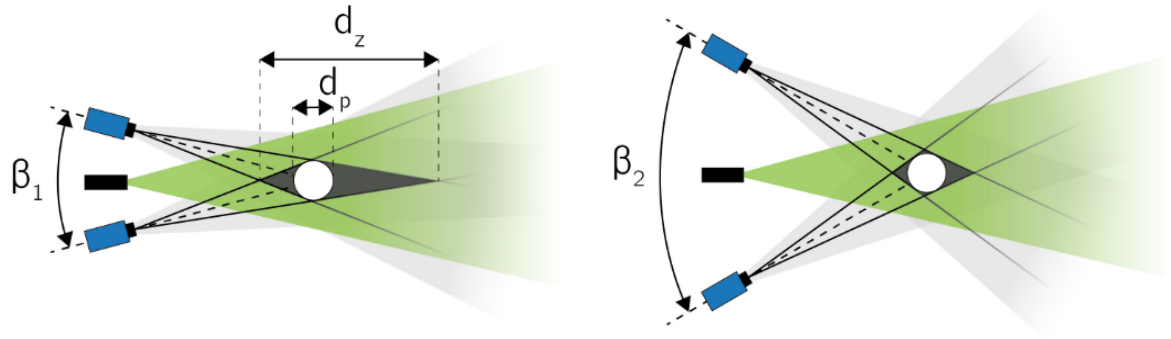

(a) Small tomographic angle β_1

(b) Large tomographic angle β_2

Figure 2.5: The effect of tomographic angle β_0 on the uncertainty of particle shape in depth. Figure duplicated from Giaquinta, (2018)

Other than the positional uncertainty, another factor limiting depth of imaging is the ability of the imaging sensor to collect the scattered light by the particle. According to Schneiders, (2017), this intensity of light I_p reduces with the fourth power of the distance z of the particle from the lens.

$$I_p \propto \frac{1}{z^4} \tag{2.3}$$

On the other hand, if the particles are too close to the sensor, they saturate the sensor due to the high scattering intensity. This minimum distance can be estimated using:

$$\frac{z_{max}}{z_{sat}} \propto \left(\frac{2^b}{I_{min}}\right)^{\frac{1}{4}} \tag{2.4}$$

where, z_{max} is the maximum measurable depth, z_{sat} is the minimum depth at which the particle saturates the sensor, I_{min} is the minimum detectable intensity and b is the bit depth of sensor. Considering these factors, the final measurement volume is of the shape of a truncated square pyramid. The shape is dependant on the angle of view ψ (approximately 50°) and the height equal to the difference between minimum and maximum imageable distance. The detailed calculations of dimensions and their governing equations can be found in Schneiders, (2017) and Jux, (2017). Typically the value for minimum imageable distance z_{min} is $10cm$ and maximum z_{max} is $50cm$. The measurement volume is approximately $30l$.

2.4.2. Lagrangian Particle Tracking - Shake-the-Box

With the advantages of HFSB, it is now possible to implement PTV, which in the past has been limited by seeding concentration. Using the new algorithm called Shake-the-Box by Schanz et al., (2016), seeding concentrations of 0.05 ppp[8] can be used achieving a sufficient spatial resolution. This algorithm

[8]abbreviation for particles per pixel

is explained briefly below.

For the initialization of this algorithm, particles are searched using IPR explained earlier(Section 2.2). Around three to four frames are enough to formulate a track. Once initialized, the positions of particles are then predicted using extrapolation of the available track information. It is then compared, using image matching, to the actual image of the next time step. The particle is moved around (shaked) until the actual particle is found and paired. The particle is then removed so that the remaining particles can be triangulated and processed in the same way. The process of this algorithm is shown in Fig. 2.6

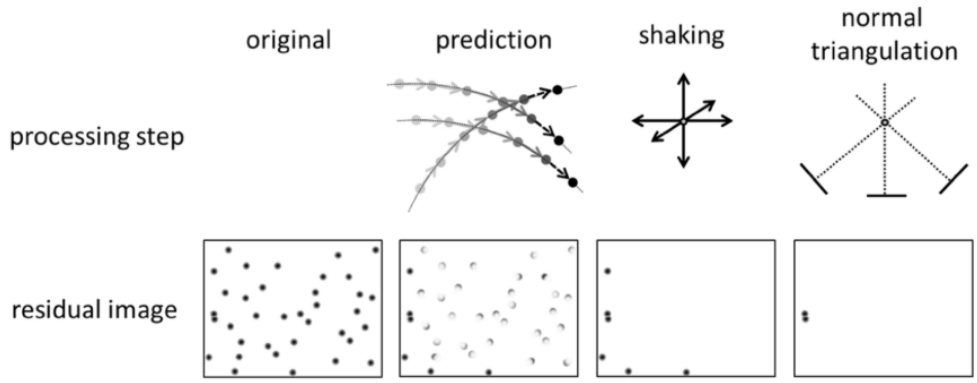

Figure 2.6: Schematic representation of the steps of STB, duplicated from Schanz et al., (2016)

2.5. Pressure Reconstruction

Pressure reconstruction from velocity data obtained from PIV has developed a lot in the last decade. A comprehensive review and comparison of various techniques to reconstruct pressure is presented by Blinde et al., (2016).The review article by van Oudheusen, (2013) summarizes these developments and explains the theory behind for pressure reconstruction from velocity fields obtained from PIV. The advantages of such a technique have been discussed above.

Starting with the Navier-Stokes equations, the pressure gradient can be computed from the momentum equation.

$$\nabla p = -\rho \frac{Du}{Dt} + \mu \nabla^2 u \tag{2.5}$$

Assuming the values of fluid density ρ and viscosity μ, are known, u is obtained from PIV and material acceleration $\frac{Du}{Dt}$ can be obtained by:

$$\frac{Du}{Dt} = \frac{\partial u}{\partial t} + (u \cdot \nabla)u \tag{2.6}$$

Substituting Eq. (2.6) in Eq. (2.5),

$$\nabla p = -\rho \left(\frac{\partial u}{\partial t} + (u \cdot \nabla)u \right) + \mu \nabla^2 u \tag{2.7}$$

In most of the applications of large scale PIV and in this thesis, time-averaged pressure field is sufficient. Reynolds averaging of Eq. (2.7) leads to the mean pressure gradient:

$$\nabla \overline{p} = -\rho(\overline{u} \cdot \nabla)\overline{u} - \rho \nabla \cdot (\overline{u'u'}) + \mu \nabla^2 \overline{u} \tag{2.8}$$

According to van Oudheusen, (2013) and Murai et al., (2007), the contribution of viscous term is negligible for sufficiently high Reynolds number. A comparison of the contribution of fluctuation terms and viscous terms is shown in Fig. 2.7, clear shows that viscous terms are negligible.

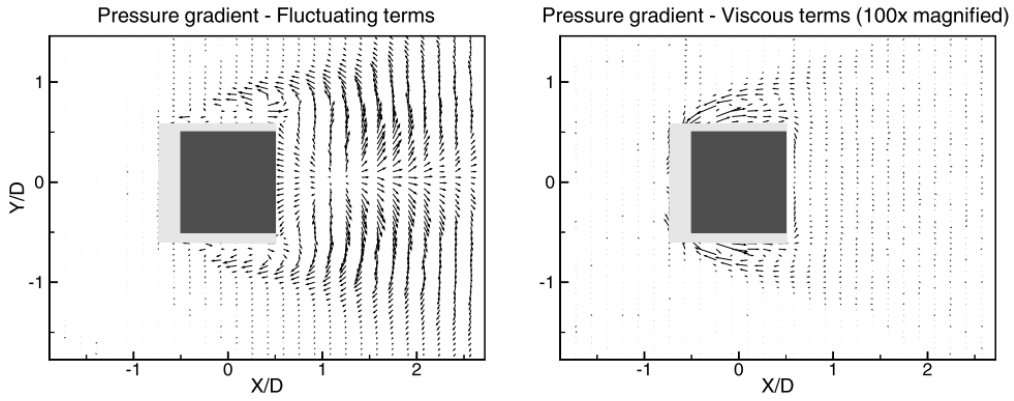

Figure 2.7: Comparison of contribution of fluctuating terms and viscous terms to mean pressure gradient for flow around square cylinder, duplicated from van Oudheusen, (2013)

Eq. (2.8) can reformulated using a Poisson approach (van Oudheusen, (2013) and Gurka et al., (1999)) by taking the divergence:

$$\nabla^2\overline{p} = -\rho\nabla\cdot(\overline{u}\cdot\nabla)\overline{u} - \rho\nabla\cdot\nabla\cdot(\overline{u'u'}) \tag{2.9}$$

Eq. (2.9) is the Poisson Equation for Pressure. It is an elliptic partial differential equation requiring prescribed boundary conditions, typically mixed (Dirichlet and Neumann). The equation is then solved numerically by discretizing the domain in the form of a Cartesian grid and using a second order finite difference scheme implemented by five-point method. The formulation of such an approach is shown using Fig. 2.8 and Eq. (2.10).

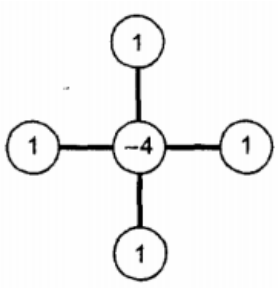

Figure 2.8: Five point method of finite difference scheme, duplicated from Hoffmann, (1992)

$$\nabla^2 p_{i,j} = \frac{1}{\Delta x^2}\left(p_{i+1,j} + p_{i-1,j} + p_{i,j+1} + p_{i,j-1} - 4p_{i,j}\right) = RHS_{i,j} \tag{2.10}$$

The $RHS_{i,j}$ in Eq. (2.10) consist of pressure gradients given by:

$$\frac{\partial\overline{p}}{\partial x} = -\rho\left(\overline{u}\frac{\partial\overline{u}}{\partial x} + \overline{v}\frac{\partial\overline{u}}{\partial y} + \overline{w}\frac{\partial\overline{u}}{\partial z} + \frac{\partial\overline{u'^2}}{\partial x} + \frac{\partial\overline{u'v'}}{\partial y} + \frac{\partial\overline{u'w'}}{\partial z}\right) \tag{2.11}$$

$$\frac{\partial\overline{p}}{\partial y} = -\rho\left(\overline{u}\frac{\partial\overline{v}}{\partial x} + \overline{v}\frac{\partial\overline{v}}{\partial y} + \overline{w}\frac{\partial\overline{v}}{\partial z} + \frac{\partial\overline{u'v'}}{\partial x} + \frac{\partial\overline{v'^2}}{\partial y} + \frac{\partial\overline{v'w'}}{\partial z}\right) \tag{2.12}$$

$$\frac{\partial\overline{p}}{\partial z} = -\rho\left(\overline{u}\frac{\partial\overline{w}}{\partial x} + \overline{v}\frac{\partial\overline{w}}{\partial y} + \overline{w}\frac{\partial\overline{w}}{\partial z} + \frac{\partial\overline{u'w'}}{\partial x} + \frac{\partial\overline{v'w'}}{\partial y} + \frac{\partial\overline{w'^2}}{\partial z}\right) \tag{2.13}$$

The fluctuating components of velocity are calculated by:

$$\overline{u'} = \sum_{i=1}^{n}\frac{u_i - \overline{u}}{n}, \qquad \overline{v'} = \sum_{i=1}^{n}\frac{v_i - \overline{v}}{n}, \qquad \overline{w'} = \sum_{i=1}^{n}\frac{w_i - \overline{w}}{n} \tag{2.14}$$

where n is the number of uncorrelated samples. Using Eq. (2.14), the Reynolds stress terms can be calculated:

$$RS_{xx} = \frac{1}{n}\sum_{1}^{n}\overline{u'^2}, \qquad RS_{yy} = \frac{1}{n}\sum_{1}^{n}\overline{v'^2}, \qquad RS_{zz} = \frac{1}{n}\sum_{1}^{n}\overline{w'^2}, \tag{2.15}$$

$$RS_{xz} = \frac{1}{n}\sum_{1}^{n}\overline{u'w'}, \qquad RS_{yz} = \frac{1}{n}\sum_{1}^{n}\overline{v'w'}, \qquad RS_{xy} = \frac{1}{n}\sum_{1}^{n}\overline{u'v'}, \tag{2.16}$$

The gradients of the Reynolds stress terms are given by:

$$\frac{\partial RS_{i,j}}{\partial x} = \frac{RS_{i+1,j,k} - RS_{i-1,j,k}}{2\Delta x} \tag{2.17}$$

Regarding the boundary conditions, typically it is seen in literature that at least one Dirichlet condition and Neumann conditions on domain boundaries are used to solve the Poisson equation.

- **Dirichlet (first-type) boundary condition:** Specifies the value of the solution (in this case, magnitude of pressure)

- **Neumann (second-type) boundary condition:** Specifies the value of the derivative of the solution (in this case, $\frac{\partial s}{\partial n}$)

2.6. Applications in Literature

Reading through the previous sections, one can understand the importance of obtaining 3D information from PIV and the importance of measuring pressure. The use of the technique of conventional PIV is commonly found in literature, in both academic research as well as industries. It is used in various sectors like aerospace, automotive, motorsport and sport aerodynamics. Nonetheless, the industries have not adopted the current state-of-the-art tomographic PIV, nor the technique of obtaining pressure from PIV. The major reasons for this are the complexity of such measurements and the added uncertainty of using newer, less tested approaches. One can say that, very few industries will undertake a risk of a failed experiment given its penalties in terms of resources, thus impacting profitability. Hence majority of the applications of volumetric PIV and pressure from PIV are found research carried out in an academic setting.

Focusing on the low speed domain, especially automotive and sports, numerous examples are found in the literature. In the automotive industry, wake flows hold a very important significance. Nakagawa et al., (2015) conducted measurements on 28% model of a passenger car in the facilities of Toyota in Japan. The measurement of flow topology in the wake provides an insight into the aerodynamic characteristics of the car in different driving conditions. It can be used to understand the stability and the vehicle dynamics affected by aerodynamics. The measurements were done suing stereoscopic PIV with the system mounted on a traverse to change the height of the measurement plane. The setup used and the results obtained are shown in Fig. 2.9a.

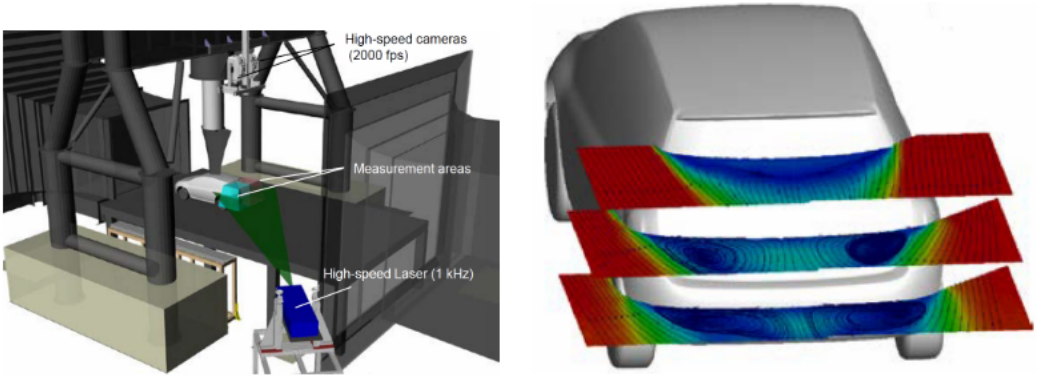

(a) Schematic of the experimental setup used

(b) Velocity contours on different planes in the wake

Figure 2.9: Illustration of the experiment conducted by Nakagawa et al., (2015) and the obtained results

An excellent piece of work regarding PIV usage in the automotive industry and its requirements is presented by Cardano et al., (2008). Some of the important requirements listed are, 3D information about flow, information on a large domain, quick and robust PIV system, remote control of the testing devices and homogeneous tracer particles. The experiments carried out in the wind tunnel of Pininfarina in Turin, Italy are also presented. One striking and unique system is the PF 3D PIV Probe (Cardano et al., (2008). It is stereoscopic PIV probe developed by Pininfarina Aerodynamic and Aeroacoustics Research Center. The probe and its mounting is shown in Fig. 2.10.

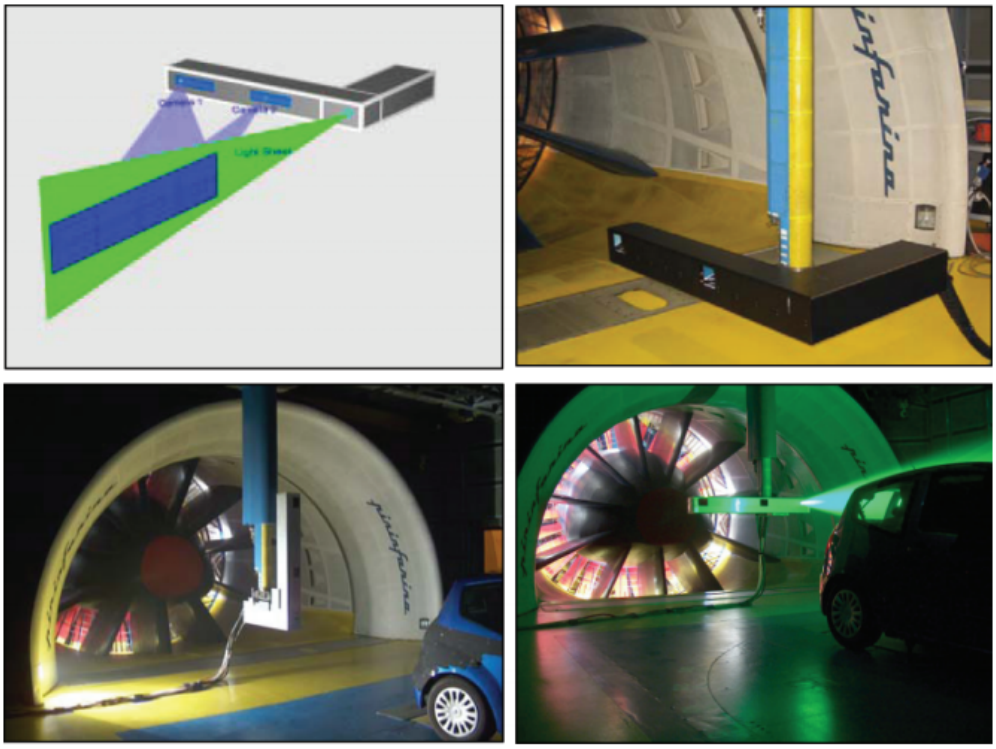

Figure 2.10: The PF 3D PIV Probe, duplicated from Cardano et al., (2008)

Another industry closely associated with automotive is the motorsport industry. Owing the competitive and highly confidential nature of the industry, very few works are published in literature. One such extensive experiment involving wake measurements of the wheel of a Formula One car is presented by Nakagawa et al., (2016). The experiments were conducted in the wind tunnel of Toyota Motorsport GmbH in Cologne, Germany. In these experiments, there was in interest to obtain 3D information.

However, due to some hurdles, conventional PIV was used. The interested region was divided into multiple planes and were measured using a traverse. Typical regions of interest and the planes used for measurement are shown below.

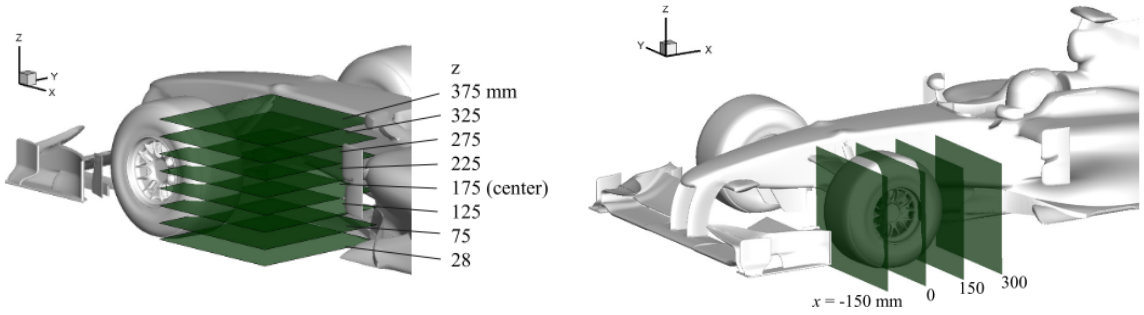

Figure 2.11: Measurement planes to obtain flow information around the front wheel, duplicated from Nakagawa et al., (2016)

In Fig. 2.11, the interest is to study the flow features around and in the wake of the front wheel. This is done by dividing the region into planes. The technique of volumetric PIV will improve the effectiveness of such an experiment.

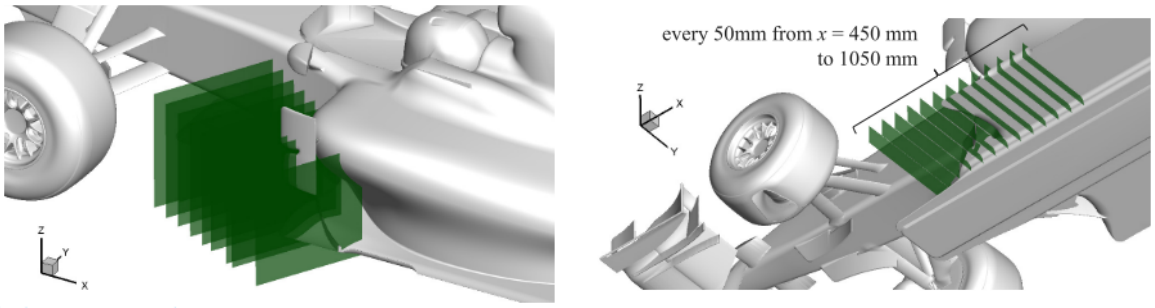

Figure 2.12: Measurement planes to obtain information in front of floor leading edge and between floor of the car and road

In Fig. 2.12, the objective is to study the flow characteristics, just in front of and in region of the leading edge of the floor. This part of the car produces most of the total downforce generated and is also most efficient. Obtaining the information of surface pressure in this region will be extremely useful, even though such a requirement is not presented.

Another similar study of large scale measurement was conducted by Casper et al., (2016). The experiment involves measurement of the wake of full size Volkswagen sedan in the Volkswagen wind tunnel at Wolfsburg, Germany. Tomographic PIV was used to analyse a region of $2m$ x 1.6 m x $0.2m$ with the use of HFSB and STB. These studies highlight the benefits of HFSB as well the requirement of such measurements in the industry.

Apart from the automotive industry, the large scale volumetric PIV has been used for a wide range of applications.In the area of sports aerodynamics, PIV is being used to improve athlete performance in sports like cycling, speed-skating, skiing etc. where aerodynamic effects are significant. Terra et al., (2016) conducted experiments to calculate drag on a full-scale cyclist by taking tomographic measurements in the wake. The drag was calculated using the conservation of momentum in a control volume approach and was found to be within 2% of the drag measured using force balance. A similar analysis was carried out by Sciacchitano et al., (2018) and Jux, (2017) , where CVV was used to study the flow topology around a full-scale cyclist. The setup and obtained result is shown in Fig. 2.13.

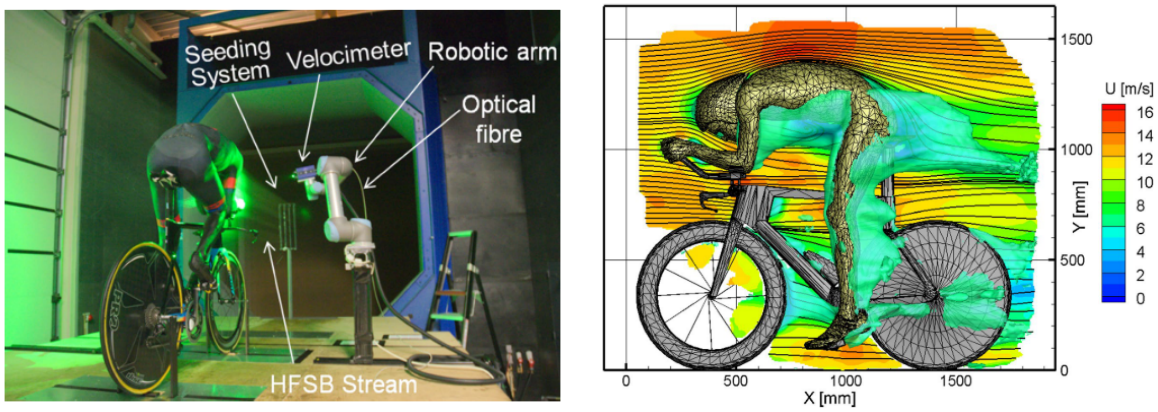

(a) Setup used for the experiment

(b) Time-averaged velocity contours and streamlines

Figure 2.13: Illustration of setup and obtained results of the full-scale cyclist experiment, duplicated from Sciacchitano et al., (2018)

An extremely useful study in terms of relevance to this thesis and highlighting the possibilities is the investigation by Ragni et al., (2009). In this investigation, aerodynamics loads on a transonic airfoil are calculated using the surface pressure reconstructed from stereo PIV. The obtained results are compared against conventional approaches. The results of this study, were comparable to those from the standard approaches, thus fueling the importance and potential of such a technique. Fig. 2.14 shows the contours of C_p obtained and Fig. 2.15 shows the comparison of C_L and C_D obtained using PIV and conventional methods (pressure taps and wake rake). However, the test model used in this case was simplistic and 2D in nature. For large scale investigations on complicated objects, the technique of planar PIV has limitations as the analysis needs to be done by taking measurements in multiple planes. Another major limitation is the opaqueness of the object to the laser sheet. Hence, even in the case of planar PIV, the entire 2D domain around the object cannot be analysed in one single measurement. The large scale CVV potentially holds advantages in this regard, but has not been proven (in literature) yet.

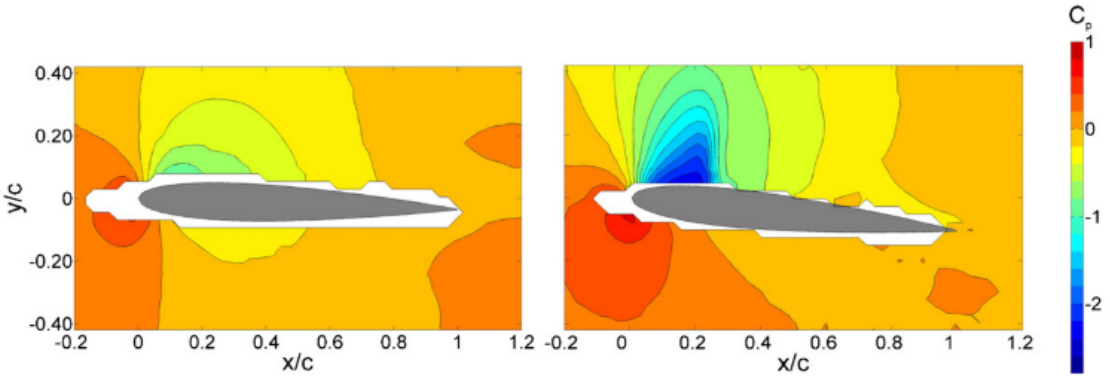

Figure 2.14: Contours of C_p at M=0.6; $\alpha = 2°$ on the left and $\alpha = 6°$ on the right, duplicated from Ragni et al., (2009)

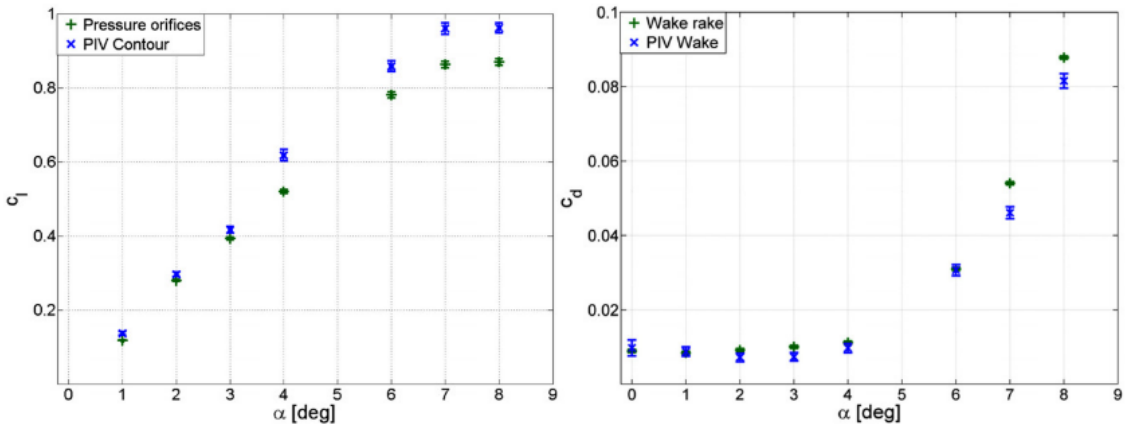

Figure 2.15: Comparison of lift(left) and drag(right) coefficients obtained using conventional methods versus PIV, duplicated from Ragni et al., (2009)

Another important domain apart from surface measurements is wake measurements as discussed towards the beginning of the section. Studying the flow topology in the wake can allow computation of drag and also help us understand the aerodynamic features of the objects. Schneiders et al., (2016) used tomographic PTV to obtain flow topology in the wake of a truncated cylinder. Poisson approach to reconstruct pressure was used and compared against the measurements from pressure transducers. The results of the measurements are shown in Fig. 2.16 and Fig. 2.17 and it can be observed that they are very much in agreement of each other.

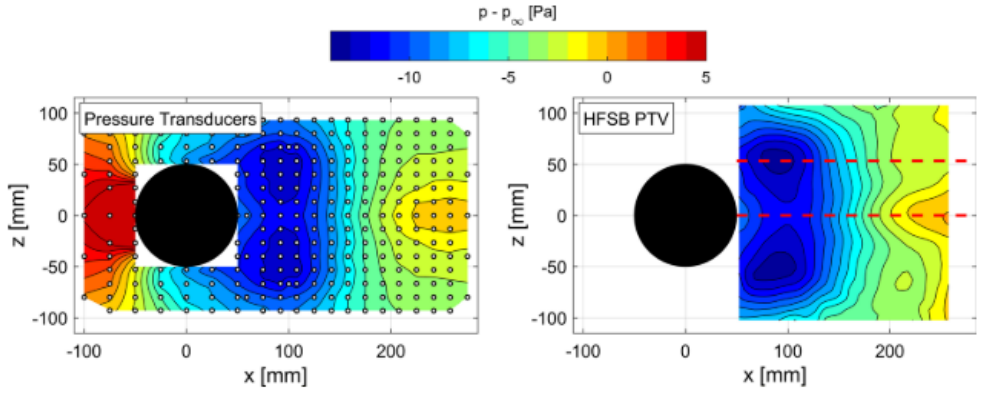

Figure 2.16: Comparison of surface pressure contours of $p - p_\infty$ generated using pressure transducers and HFSB PTV, duplicated from Schneiders et al., (2016)

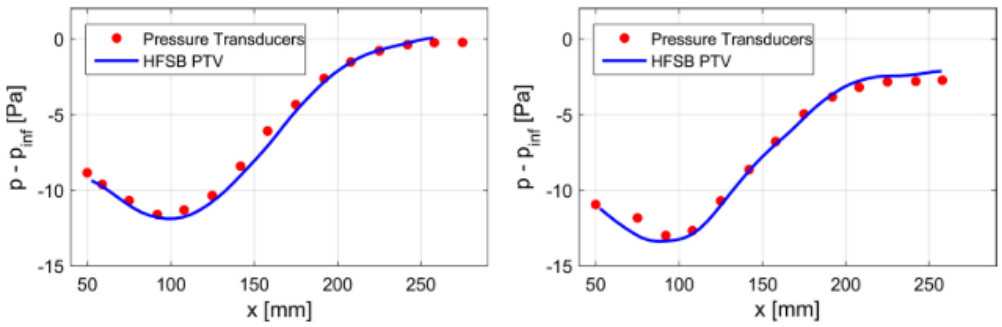

Figure 2.17: Comparison of time-averaged surface pressure along the red dashed lines shown in Fig. 2.16, duplicated from Schneiders et al., (2016)

A very similar study was conducted by Celaya, (2018), studying the wake of a truncated cylinder using CVV. By obtaining the volumetric velocity field, the pressure field was reconstructed using Poisson equation. The obtained pressure field is further processed to compute total pressure of the flow and compared against kiel probe. The comparison is shown in Fig. 2.18

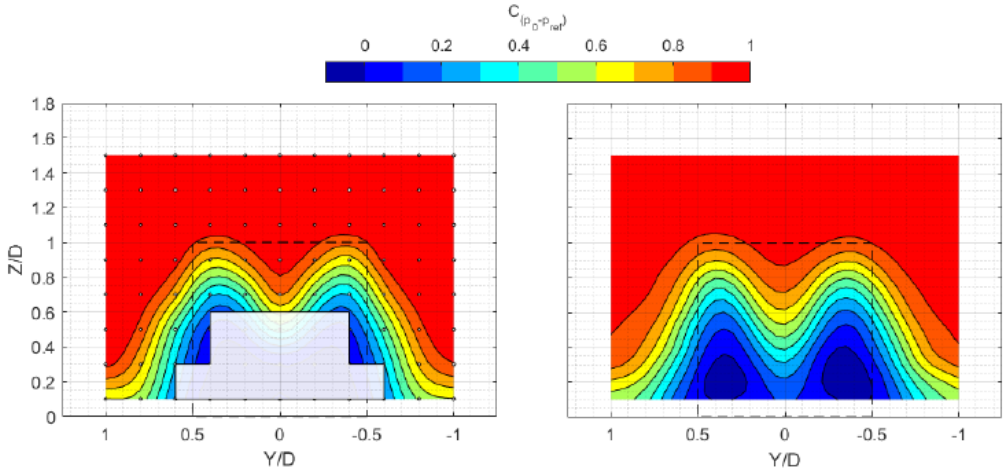

Figure 2.18: Comparison of total pressure obtained on a plane in the wake of truncated cylinder using keil probe(left) and CVV(right), duplicated from Celaya, (2018)

The static pressure is also compared against pressure taps on the floor in the wake region. The comparison is shown in Fig. 2.19.

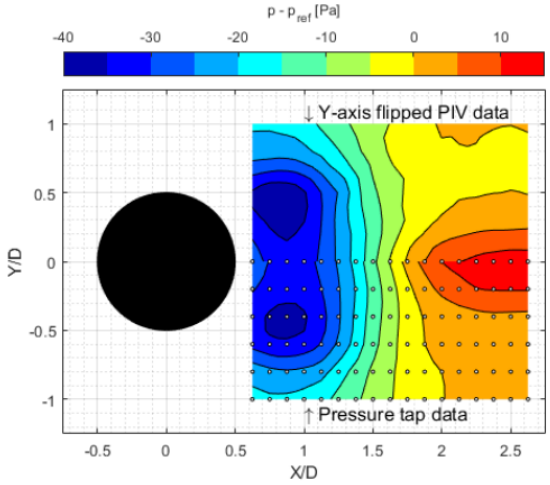

Figure 2.19: Comparison of surface pressure on the floor in the wake of truncated cylinder obtained using CVV(top) and pressure taps(bottom), duplicated from Celaya, (2018)

3

Experimental Setup and Procedure

In this chapter, the setup and the equipment used to perform the experiments are explained. The first part of the chapter deals with the facilities and equipment used specific to this experiment like the wind tunnel, test section, test model etc. The latter part describes the specifications of systems like CVV, robot, pressure transducers, software required etc. The purpose is to give the reader an insight into the hardware and software required to carry out a typical experiment using the CVV system.

3.1. Experimental Setup

3.1.1. Wind Tunnel

The experiment is carried out in the W-tunnel in the High Speed Laboratory of Delft University of Technology. It is a low speed, open circuit wind tunnel with the nozzle exit areas of 0.4 x 0.4 m^2, 0.5 x 0.5 m^2 and 0.6 x 0.6 m^2. In this experiment, the nozzle of 0.4 x 0.4 m^2 cross-section was used. The maximum velocity achievable is 35 m/s with a reported turbulence intensity of 0.5% (Delft University of Technology, (2018)). The wind tunnel is powered by a centrifugal fan driven by a 16.5 kWh motor. The velocity is measured and adjusted based on the information of dynamic pressure in the nozzle measured using a pitot tube.

3.1.2. Test Model

The model used is an inverted wing with a constant span-wise cross-section of a thick cambered airfoil. The span is 400 mm and chord length is 200 mm. The span being exactly equal to the width of the test section, prevents the formation of wing tip vortices. The material used for the model is aluminium and painted matte black in order to minimize reflections of the laser. The model is held at a constant angle using two M8 bolts on each side. The model is equipped with 30 pressure taps of approximately $\varnothing = 0.4\ mm$. The tubes connecting the pressure taps to transducer are routed through one of the sides of the wing. Fig. 3.1 shows the airfoil cross-section and the chord-wise location of the pressure taps.

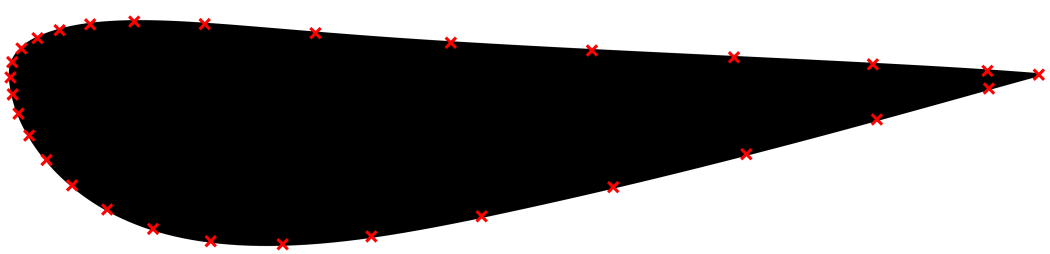

Figure 3.1: Cross-section of the wing; red crosses indicate the chord-wise position of the pressure taps

3.1.3. Test Section

The test section is fitted at the exit of the nozzle of the wind tunnel. The test section is closed with the cross-section same as that of the nozzle, 0.4 x 0.4 m^2 and length of 1.5 m. It is made out of 10 mm transparent plexi-glass and is shown in Fig. 3.2. The robot and the CVV probe(described in Section 3.4.1) are also shown. The imaging is done through the plexi-glass and hence is completely non-intrusive.

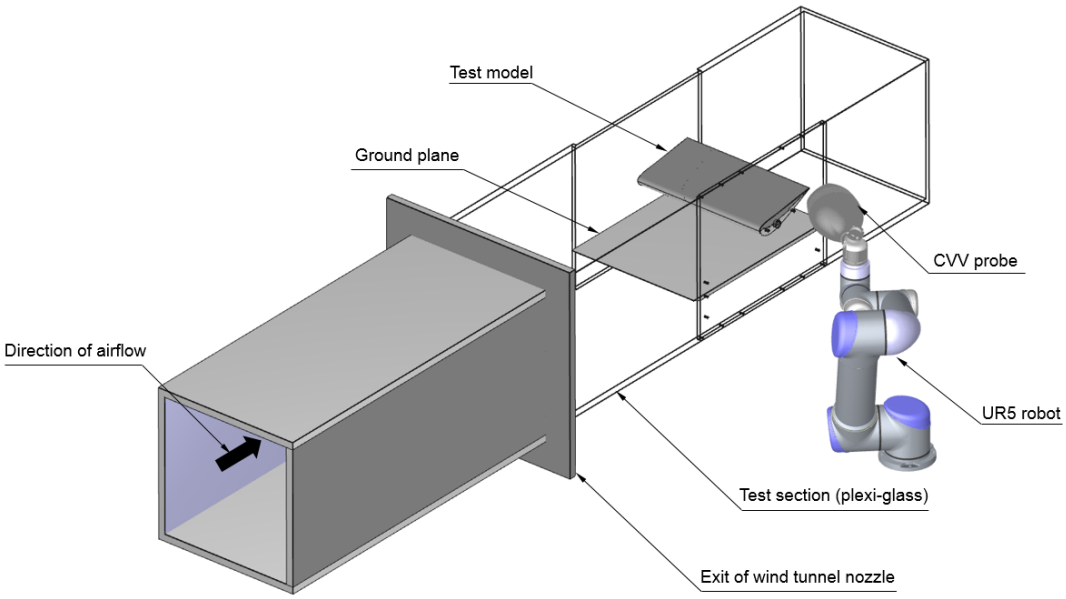

Figure 3.2: Schematic illustration of the setup used for the experiment, showing the wind tunnel exit, model mounting and the robot position

At a distance of 0.85 m from the exit of the nozzle, the test model of an inverted planar wing (described in detail in Section 3.1.2) is fitted using the side walls of the test section. The side walls of the test section had removable panels which can be used to mount the model onto and then fit into the test section. These panels were made specific to the mounting of the particular model and test configuration. Since the model will be tested in ground effect at different clearances, the panels had to accommodate for such an arrangement. The ground effect was produced by using a flat plate located below the wing. The ground plate had a sharp leading edge (12°) so that the boundary layer developed can be fed below the ground plane and wing does not experience its effect. Fig. 3.3 illustrates this phenomenon schematically.

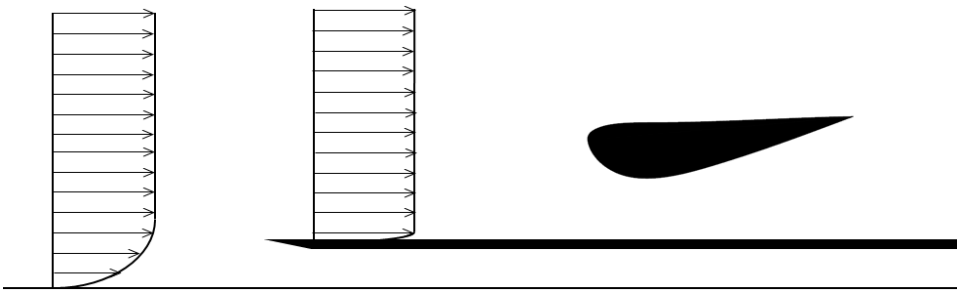

Figure 3.3: Schematic illustration of development of a fresh boundary layer using a sharp leading edge plate

3.2. Test Matrix

The configurations tested during the experiment are presented in Table 3.1. The ground effect is represented as a ratio (h/c) of the distance between the wing and ground plane (h) to the chord length (c).

Angle of Attack	Ground (h/c)
5°	(h/c) = 1 (No ground effect)
5°	(h/c) = 0.6 (Moderate ground effect)
5°	(h/c) = 0.3 (Strong ground effect)
8°	(h/c) = 1 (No ground effect)

Table 3.1: Configurations tested

3.3. Seeding System

The HFSB described in Section 2.3 are used as tracer particles in this experiment. The system to generate these consists of two main components: the Fluid Supply Unit[1] and seeding rake. The bubbles are generated by the nozzles of the seeding rake, designed by the Aerodynamics department of Delft University of Technology. The seeding rake is made up of ten wings, each having 20 nozzles. Each wing is 1 m in height and the spacing between two consecutive wings is 50 mm. It can be assumed that the 200 nozzles produce seeding particles in an area approximately 0.95 x 0.5 m^2. The estimated production rate per nozzle is 10000 bubbles per second and considering 150 reliably working nozzles, the production rate is 1.5x10^6 bubbles per second. The seeding rake is mounted in the settling chamber of the W-Tunnel as shown in Fig. 3.4. The contraction of stream tube implies that the seeding in the test section is approximately of 0.35 x 0.2 m^2(central part).

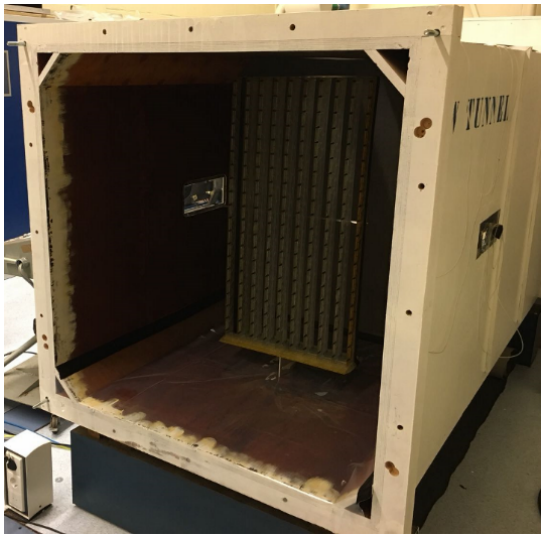

Figure 3.4: Seeding rake and its mounting in the settling chamber of the W-Tunnel

For production of bubbles the fluids required, namely air, helium and soap are supplied to the seeding rake at controlled pressures. This is done using the Fluid Supply Unit manufactured by *LaVision*, shown in Fig. 3.5. The soap is stored in a reservoir pressurized using compressed air. The helium is supplied through a standard pressurized bottle. The pressures can be controlled manually by adjusting the knobs or remotely via a computer. The pressures 2.5, 1.5 and 2.0 bar have been used in this experiment.

[1]hereafter referred to as FSU

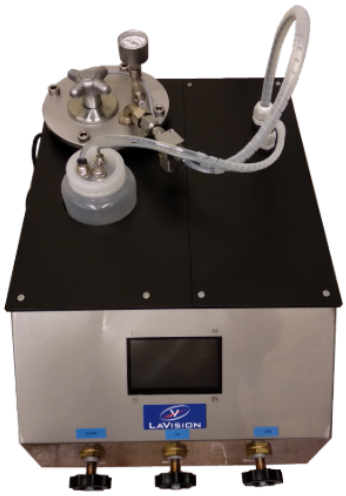

Figure 3.5: Fluid Supply Unit

3.4. CVV Equipment

The subsystems which are required for robotic coaxial volumetric velocimetry are described in detail below.

3.4.1. Coaxial Volumetric Velocimetry Probe

The CVV probe *MiniShaker Aero* developed by *LaVision*. It is an updated version of the *MiniShaker S*, with the primary intention to reduce the aerodynamic influence due to its intrusiveness, described in the work of Jux, (2017). The *MiniShaker Aero* consists of an egg-shaped case, housing 4 CMOS cameras at a fixed tomographic angle and co-axially mounted optical fiber delivering the illumination. This compact arrangement has an approximate volume of 132 x 106 x 276 mm^3 and is mounted on a robot for quick and precise positioning. The CVV probe is shown in Fig. 3.6 and its specifications are summarized in Table 3.2.

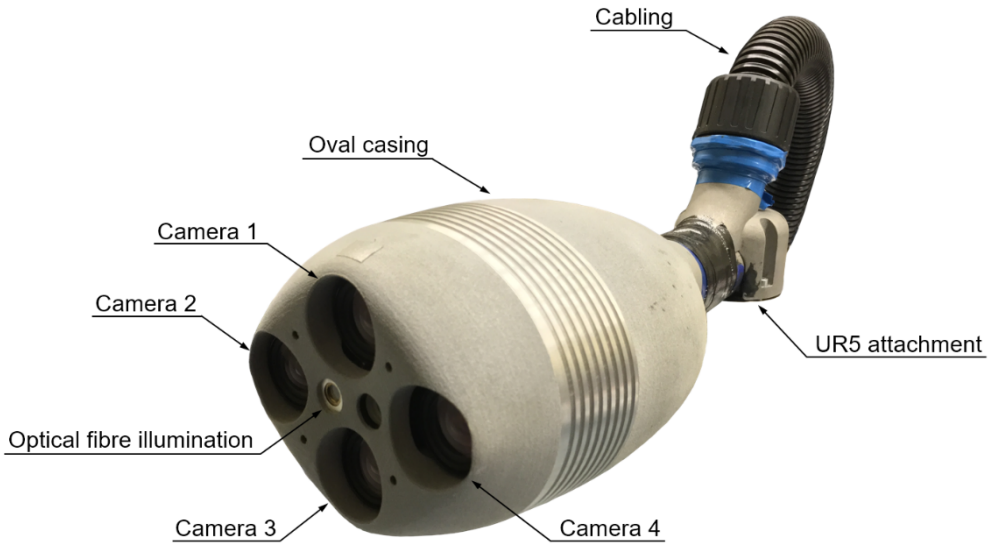

Figure 3.6: *LaVision MiniShaker Aero* probe, duplicated from Celaya, (2018)

	Parameter	Symbol	Value	Unit
Optics	Focal length	f_i	4	$[mm]$
	Numerical aperture (at z_0 = 400 mm)	$f_\#$	11	$[-]$
Imaging	X tomographic aperture	β_x	8	$[°]$
	Y tomographic aperture	β_y	4	$[°]$
	Sensor size	S_x x S_y	640 x 475	$[px^2]$
	Pixel pitch	Δpx	4.8	μm
	Magnification (at z_0 = 400 mm)	M	0.01	$[-]$
	Bit depth	b	10	$[bit]$
	Acquisition frequency	f	821	$[Hz]$

Table 3.2: Technical specifications of *LaVision MiniShaker Aero*

3.4.2. Illumination

The source of illumination for the experiment is a high-speed laser: *Quantronix Darwin Duo Nd:YLF*. The maximum power of the laser is 25 mJ when both oscillator cavities are triggered simultaneously. The working frequency range of the laser is 0.2 kHz - 10 kHz. Unlike conventional PIV, the laser head can be stored relatively further from the test section. The laser beam is focused on one end of the optical fiber using a combination of lenses in the fiber coupler unit. This light is then carried by the optical fiber and delivered to the CVV probe. On the CVV probe, the laser is expanded into a cone to illuminate the volume of interest using a spherical lens. The volume illuminated can be approximated as a truncated pyramid as shown in Fig. 3.7. The illuminated region has a volume of approximately 16 L. The closest imageable plane at 200 mm from face of the CVV probe has the dimensions of 100 x 100 mm^2 which expands upto an area of 310 x 254 mm^2 at a depth of 440 mm, which is the maximum imageable plane. The horizontal and vertical expansion angles are 13.5° and 9.5° respectively.

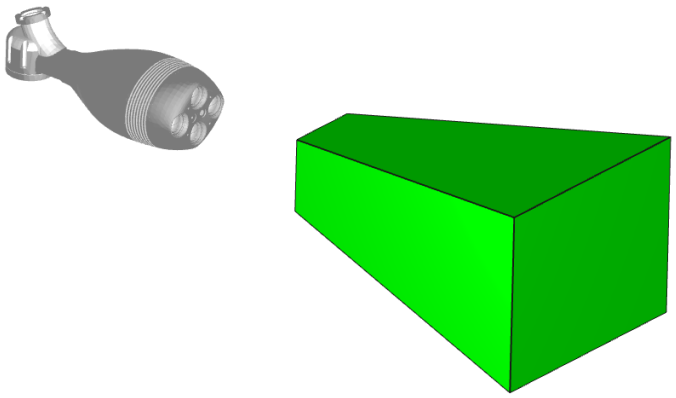

Figure 3.7: *LaVision MiniShaker Aero* probe with the illuminated volume represented by the green truncated pyramid

3.4.3. Robotic Arm

One of the biggest advantages of this system, is its ability for quick manipulation and precise positioning. This is achieved by mounting the CVV probe on the end of a robotic arm; *Universal Robots - UR5*[2] in this experiment. It consists of 6 joints:(i) Base (ii) Shoulder (iii) Elbow (iv) Wrist 1 (v) Wrist 2 (vi) Tool, working collaboratively with a maximum reach of 850 mm. It has a total of 6 degrees of freedom (one for each joint), with each joint able to rotate $\pm 360°$ at a maximum speed of $\pm 180°/s$. The specified

[2] https://www.universal-robots.com/products/ur5-robot/

accuracy of the robot is $\pm 0.01\ mm$ with a repeatability of $\pm 0.1\ mm$. The maximum payload that the robot can carry is 5 kg. The robot and its joints are shown in Fig. 3.8.

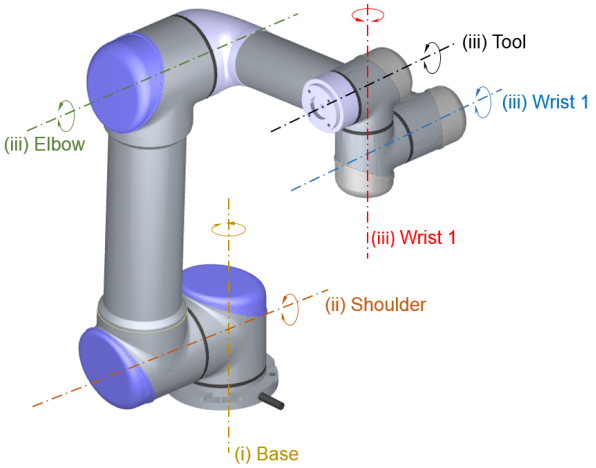

Figure 3.8: *Universal Robots - UR5*; showing rotation axes

Apart from the tablet that comes with the robot, it can be also be controlled remotely using the software called *RoboDK*[3]. This software allows to simulate the movement and positioning of the robot in 3D space. It also allows to program the robot and assign target positions for the robot. Thus, it can be used to prepare for the experiment beforehand, saving several wind tunnel testing hours.

3.4.4. Acquisition PC

Throughout the experiment, the Acquisition PC is used to perform various activities. The main task is to trigger the cameras and laser synchronously through *LaVision* Programmable Timing Unit X[4]. The software *Davis 8.4.0* developed by *LaVision* is used for this purpose. It is also used to perform further operations like image pre-processing, PTV tracks calculation, data conversion etc. Apart from that, the Acquisition PC is also used to control the FSU and the robot as mentioned above. The technical specifications of the PC are summarized in Table 3.3.

Operating system	Windows 7 professional Processor
Processor	2 x Intel(R) Xeon(R) CPU E5-2650 v3 @ 2.30 GHz
RAM	64 GB
Local disk	SSD 850 PRO 512 GB
RAID storage	AVAGO SMC3108 SCSI 4 TB disk

Table 3.3: Technical specifications of the Acquisition PC

3.5. CVV Data Acquisition

This section offers an insight into the different aspects of acquiring CVV data during a typical experiment.

3.5.1. Geometrical Calibration

Like any measurement system, the CVV system also requires calibration. The conventional pin-hole model (Soloff et al., (1997)) is used. The *LaVision - Type 30* calibration plate is used for this purpose. By taking images of the plate at different distances (150 mm, 250 mm, 350 mm, 450 mm and 550

[3] `https://robodk.com/index`
[4] hereafter referred to as PTU-X

mm), a right-hand co-ordinate system is defined with *X*- and *Y-axis* in plane of the plate and *Z-axis* normal to the plate. To improve the accuracy of the calibration, volume self-calibration is performed as explained by Wieneke, (2008). On the obtained calibration, an Optical Transfer Function[5] is calculated as given by Schanz et al., (2012). This function re-projects the particles from 3D-space to 2D image co-ordinates. This function is crucial for Shake-the-Box algorithm of particle tracking and hence holds a high importance in regards with quality.

3.5.2. CVV Probe Positioning

The positions of the various volumes measured for one configuration are shown in Fig. 3.9. The positions were simulated and targets were fixed in *RoboDK* with the objective to scan a large domain around the wing as shown. A total of 8 unique positions were used to measure the entire domain. 20000 images were taken at each position making it a total of 160000 images per configuration. The reason for the high number of images is to ensure sufficient spatial resolution and statistical convergence. The volumes measured can be re-positioned in 3D space with the help of a rotational calibration. The reader can is requested to refer to the work Jux, (2017) for the details of such a calibration.

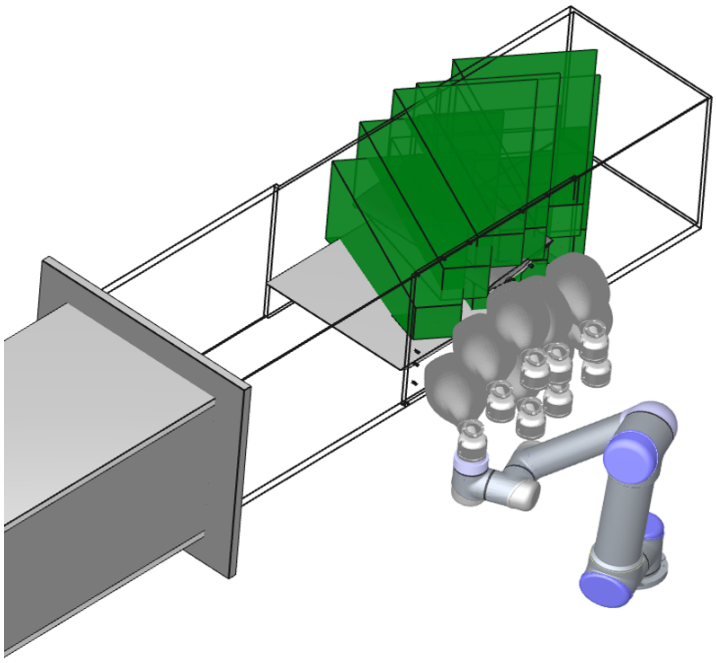

Figure 3.9: Illustration of the eight different positions used

Since the CVV system suffers from an increased uncertainty in the direction of depth, the positions are chose such that the freestream flow is perpendicular to the imaging axis of the CVV probe. This meant measuring through the side walls of the test section made out of 10 mm plexi-glass. This imposed a limitation on the positioning of the CVV, especially the angle between the CVV probe and plexi glass. The light passing through the plexi-glass refracts and hence has a finite offset with respect to the CVV. However, the axis of CVV is an imaginary axis used for positioning the data and hence does not account for the effects of refraction. This is illustrated in Fig. 3.10. The light scattered by the particle undergoes a change in its path due to the refractions at the interfaces of air and plexi-glass. However, the axis, which is obtained from the rotational calibration, is unaffected and hence the particle is perceived to be at a different location as shown. As long as the the angle of imaging is constant, the offset is a constant value and does not affect the positioning of data. As soon as the angle is changed, the offset is also affected and the data can no longer be placed in the correct location in space. Hence, the positions shown above are merely achieved by translation of the probe in *X*- and *Z-direction* and the distance between the test section and CVV probe in *Y-direction* is kept constant throughout.

[5]hereafter referred to as OTF

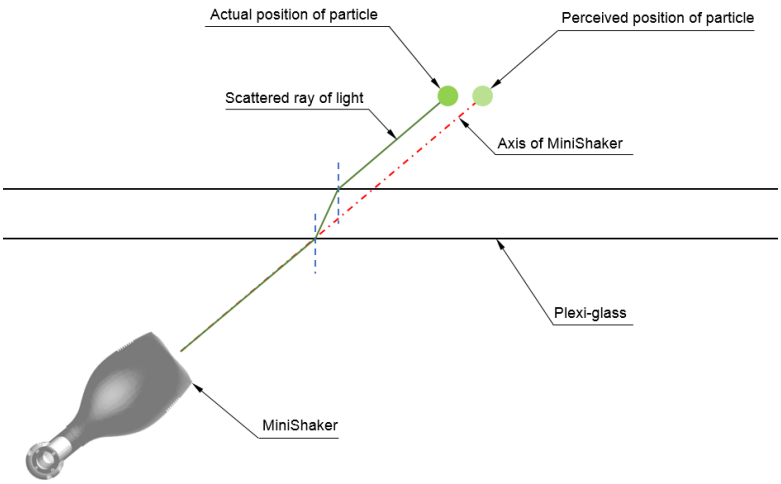

Figure 3.10: Illustration of the effect of refraction due to imaging through the plexi-glass (dimensions exaggerated for clarity)

3.6. Pressure measurements

To measure the static pressure from the pressure taps, the NUB pressure measurement system is used. This system is a state-of-the-art system, developed by NUB Systems in partnership with the Delft University of Technology. It consists of piezoresistive silicon pressure transducers of High Accuracy Silicon Ceramic[6] Series developed by *Honeywell*. The system allows to measure pressure at 80 locations simultaneously. The measurement sensor units are available in three different FSS[7] ranges: $\pm 160\ Pa$, $\pm 600\ Pa$ and $\pm 2500\ Pa$. Each sensor unit has 16 lines to measure pressure .The data was aquired using a software called *LabView* developed by *National Instruments*[8].

Since the experiment is conducted at a speed of 10 m/s, the units with range of $\pm 160\ Pa$(S1) and $\pm 600\ Pa$(S2) are sufficient. The lines of the 16 pressure taps on the suction side of the wing are connected to the sensor S2 and the rest 14 of the pressure side are connected to S1. The characteristics of these sensors are summarized in Table 3.4

Sensor type [-]	FSS Range [Pa]	Total Error Band [% FSS]
S1	± 160	± 2.5 (4 Pa)
S2	± 600	± 1.0 (6 Pa)

Table 3.4: Characteristics of the sensors used

3.7. Pressure Data Acquisition

1. **Cleaning of pressure taps and lines:** The pressure taps and the tubes are susceptible to clogging by dust or other particulate matter. Hence, they need to be properly cleaned before taking any acquisition. It was also observed that, the pressure taps were completely blocked due the soap solution after a CVV acquisition run, making simultaneous CVV and pressure measurements impossible. The taps were cleaned by blowing compressed air at approximately 1 bar directly at the taps and also from the other end of the tube.

2. **Pressure taps and sensors test:** Before starting the actual measurements, it is important to also check whether the pressure taps as well as the sensors are working correctly. In certain cases, it is possible that pressure taps are still clogged, the tube has a leak or even the sensor is damaged.

[6] hereafter referred to as HSC
[7] abbreviation for Full Scan Span
[8] `http://www.ni.com/en-us/shop/labview.html`

To ensure everything was functioning correctly, every tap was connected to the respective sensor and real time data was monitored. By simply keeping a finger on the pressure taps, the sensor would respond accordingly indicating that both the tap and sensor were in working condition.

3. **Data acquisition and storage:** The pressure readings were recorded using a *LabView* program. Before starting the wind unnel, the sensors were set to null. Then the wind tunnel was started and after allowing the flow to be steady, pressure was recorded at a frequency of 2 kHz for a total of 20s.

4. **Checking the quality of data:** After the data is obtained, the mean and standard deviation is calculated using a *MATLAB* script. The distribution of pressure readings at the stagnation (sensor S1) and suction peak (sensor S2) is illustrated using a histogram along with the mean and standard deviation. It is seen that the value of standard deviation is much lower than the rated uncertainty (Table 3.4), indicating that the quality of data is acceptable since the flow is steady.

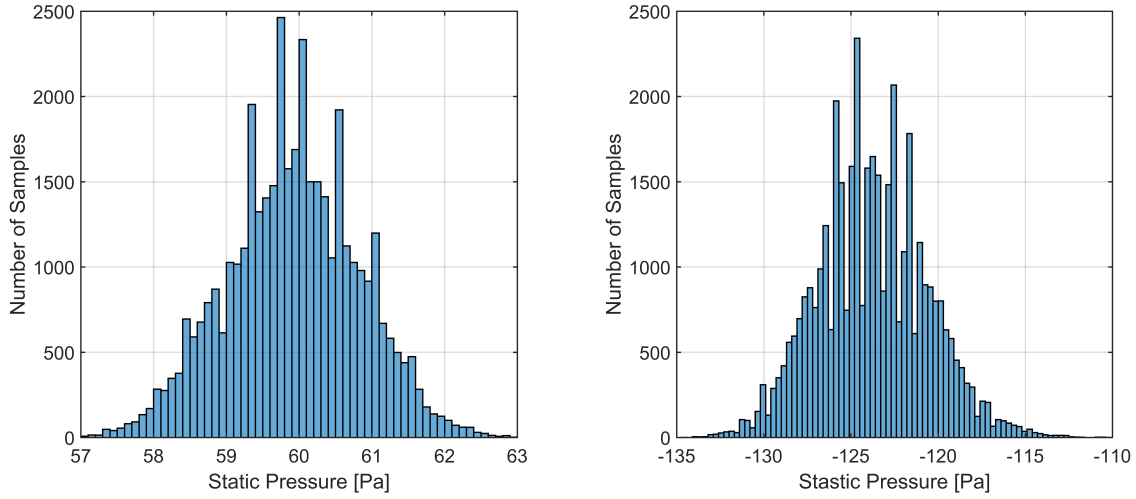

(a) Stagnation; $\overline{p} = 59.91Pa; \sigma = 0.91Pa$

(b) Suction peak; $\overline{p} = -123.76Pa; \sigma = 3.15Pa$

Figure 3.11: Histograms for pressure tap readings at stagnation and suction peak, accompanied by the mean($\overline{p}$) and standard deviation(σ); based on 40000 samples for angle of attack of 5° and no ground effect

4

Data Processing

In this chapter, the processing of the data obtained from CVV measurement is explained. Starting from raw images to obtaining pressure, each step is explained and the reasoning behind the steps taken is stated. After reading this chapter, the reader will have an idea about how the data was reduced to obtain meaningful results.

4.1. Image Pre-Processing

A very well-known step in any PIV technique is image processing. The obtained raw images are rarely in a condition that they can be directly used for computation. In conventional planar PIV, operations like masking of images comes under the step of pre-processing. In this case, the main objective is to get rid of large reflections caused by the laser and the background noise. This is important as it might cause wrong pairing of particles and increase the amount of ghost particles. The perfect case would be the one where the image consists of a high light intensity pixels at locations where the particles are present and everything has zero intensity.

For this purpose, a method introduced by Sciacchitano and Scarano, (2014) is used to eliminate reflections. A third order Butterworth High Pass Filter is implemented with a filter length of seven images. Observing pixels where reflections are present, the light intensity is constant or has a very low frequency of intensity variation. Contrary to reflections, the particles exhibit a high frequency intensity variation for a pixel. By subtracting the pixels exhibiting low frequency, only the pixels with particles can be retained. The implementation of such a filter is shown in Fig. 4.1. Further, the particles with intensity lower than 20 $counts$ are also filtered by using a simple arithmetic *AboveBelow* filter.

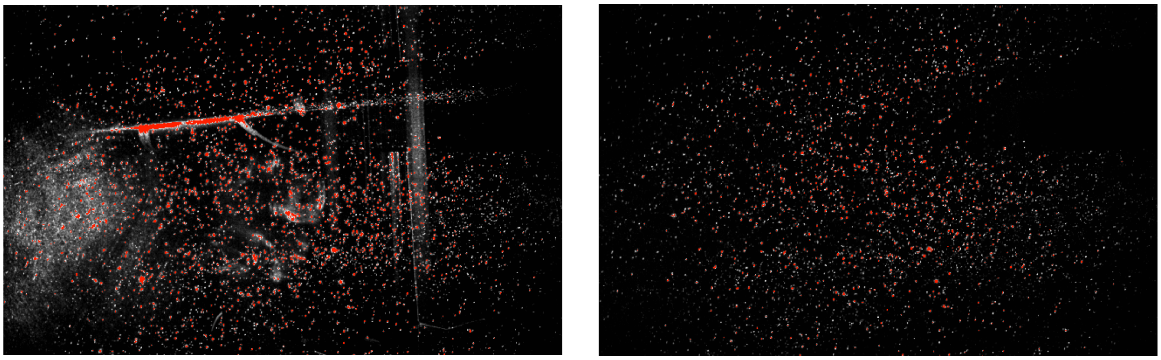

(a) Raw image showing the refelctions and background noise

(b) Image after applying the Butterworth filter, showing the elimination of reflections and background noise

Figure 4.1: Comparison of raw versus filtered image

4.2. Tracks Generation using Shake-The-Box

The Lagrangian particle tracking algorithm Shake-the-Box is used for generation of tracks. This is implemented in *Davis 10.0.5*. There a number of parameters that are associated with the generation of tracks from particle detection to filtering of noise. The parameters used for the generation of tracks are summarized in Table 4.1. The important parameters of those are explained in detail below.

- **Threshold for 2D particle detection:** This threshold determines what is noise and what are particles. This is an additional filter as in some cases, the images may still contain background noise after pre-processing. The particles with intensity value lower than this threshold, are not considered for generation of tracks. In this case, due to the *AboveBelow* filter, the threshold was also set to 20 $counts$ as the image did not have any pixels with intensity lower than that value.
- **Allowed triangulation error:** This is the error tolerated for matching particles from different cameras. A too small value means very few particles will be detected, whereas a too large value means too many particles will be detected, which might cause a problem for particle matching. According to Schanz et al., (2016), this value should lie in the range of 0.5 to 1.5 $voxel$.
- **Maximum abs. change in particle shift:** This parameter controls the allowed acceleration. The main function is to enable correct temporal matching of particles and eliminated ghost tracks.

	Parameter	Value	Unit
Volume	X_{min}	-166.133	$[mm]$
	X_{max}	136.466	$[mm]$
	Y_{min}	-104.731	$[mm]$
	Y_{max}	113.033	$[mm]$
	Z_{min}	-139.952	$[mm]$
	Z_{max}	200.067	$[mm]$
Particle Detection	Threshold for 2D particle detection	20	$[counts]$
	Allowed triangulation error	1	$[voxel]$
Shaking	Adding particles(outer loop)	4	$[-]$
	Refine particle position and intensity(inner loop)	2	$[-]$
	Shake particle position by	0.2	$[voxel]$
	Remove particles if closer than	9	$[voxel]$
	Remove weak particles if the intensity<	20	$[\%]$
Particle image shape and intensity	Make OTF smaller	1.5	$[-]$
	Residuum computation - increase particle intensity	5	$[-]$
	Residuum computation - OTF radius	1	$[pixel]$
Velocity limits	V_x	10 ± 12	$[m/s]$
	V_y	0 ± 8	$[m/s]$
	V_z	-8 ± 4	$[m/s]$
Acceleration limits	Maximum abs. change in particle shift	1	$[voxel]$
	Maximum rel. change in particle shift	20	$[\%]$

Table 4.1: Parameters used for Shake-the-Box algorithm

4.3. Ensemble Averaging and Outlier Filtering

The obtained data set from STB is unstructured and gives a Lagrangian description of the flow. However, it is much convenient to analyse the flow in the form of a structured Eulerian grid. Such a grid allows for easy calculation of gradients, especially important in this case as these gradients are used for pressure reconstruction. Hence the volume is discretized into a homogeneous grid with the data averaged per element[1] of this grid.

Agüera et al., (2016) have presented different ensemble averaging techniques, specifically for 3D PTV. A comparison of Top-Hat, Gaussian and Polynomial filter is shown in Fig. 4.2. It can be seen that the Gaussian filter is more accurate than Top-Hat as it weights the contribution of the particle velocity based on its distance from the bin center. It is slightly more expensive, computationally to the simple Top-Hat filter.

[1] also referred to as bins

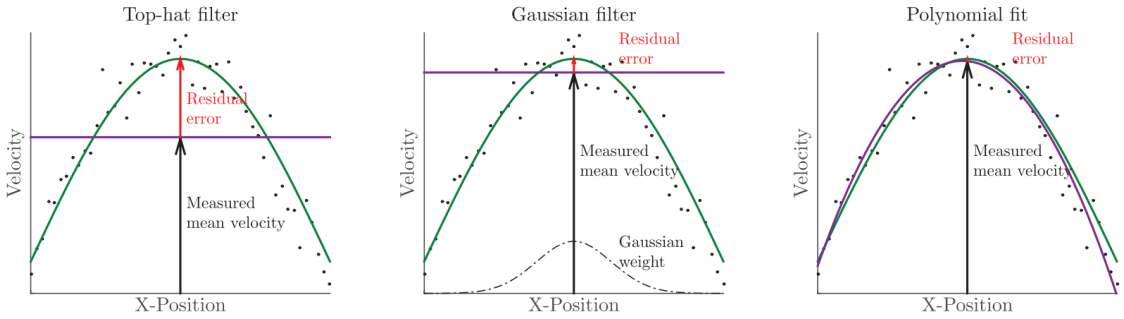

Figure 4.2: Comparison of the residual error by Top-Hat filter, Gaussian filter and polynomial fitting for an interrogation volume; black dots represent actual particle velocities, green line represents actual mean velocity and purple line represents filtered mean velocity. Figure duplicaed from Agüera et al., (2016)

Further improvement in accuracy can be obtained by implementing a polynomial fit. It can be implemented for a particle n with velocity u based on the following second order polynomial:

$$u_n = a_0 + a_1\Delta x_n + a_2\Delta y_n + a_3\Delta z_n + a_4\Delta x_n^2 + a_5\Delta x_n\Delta y_n + a_6\Delta y_n^2 + a_7\Delta x_n\Delta z_n + a_8\Delta y_n\Delta z_n + a_9\Delta z^2 \quad (4.1)$$

where $(\Delta x, \Delta y, \Delta z)$ are distances from the bin center. The system equations can be solved to obtain the coefficients a_i. From the value of this polynomial at the bin center, corresponding velocity can be obtained at an interrogation spot in that bin. These equations need to be solved at every bin and hence makes this technique computationally expensive. For the present study, a first order polynomial of the similar type is implemented.

Apart from the polynomial fitting, the ensemble averaging procedure also includes an additional filter to eliminate noise and false tracks. From the obtained statistical data from the averaging, the particles which have a deviation of more than three standard deviations are discarded.

$$u_{n_{valid}} \iff u_n \in \left[\overline{u_n} \pm 3\sigma\right] \quad (4.2)$$

4.4. Pressure Reconstruction

The methodology of pressure reconstruction is explained in Section 2.5. Based on this methodology a solver compiled by Ebbers and Farneback, (2009) is used to compute the pressure field. The domain is reduced and simplified in shape to ensure that it is simply connected and robust for the pressure computation. The solver applies Neumann boundary condition to the boundaries of the domain, to obtain an integration with a finite constant. The Dirichlet boundary condition is applied with an aim to eliminate the constant. This is applied at points upstream of the model (Fig. 4.3), in a region where Bernoulli's principle can be assumed to be valid:

$$p_0 = p + q = p + \frac{1}{2}\rho v^2 \quad (4.3)$$

where, p_0 is total pressure, p is static pressure, ρ is the density and v is the local flow velocity. In the freestream, p can be set as the reference (zero), making $p_0 = q$. Using the velocity field obtained from CVV, the value pf p at the points where Dirichlet condition is to be imposed can be estimated (p_D). These values are used to obtain the correct solution from the solver by applying the mean difference between the Dirichlet values (p_D) and the values obtained by applying the Neumann condition (p_N). The final pressure field can be obtained by:

$$p(x,y,z) = p_N(x,y,z) + \sum_{i=1}^{N} \frac{p_{D_i}(x_i,y_i,z_i) - p_{N_i}(x_i,y_i,z_i)}{N} \quad (4.4)$$

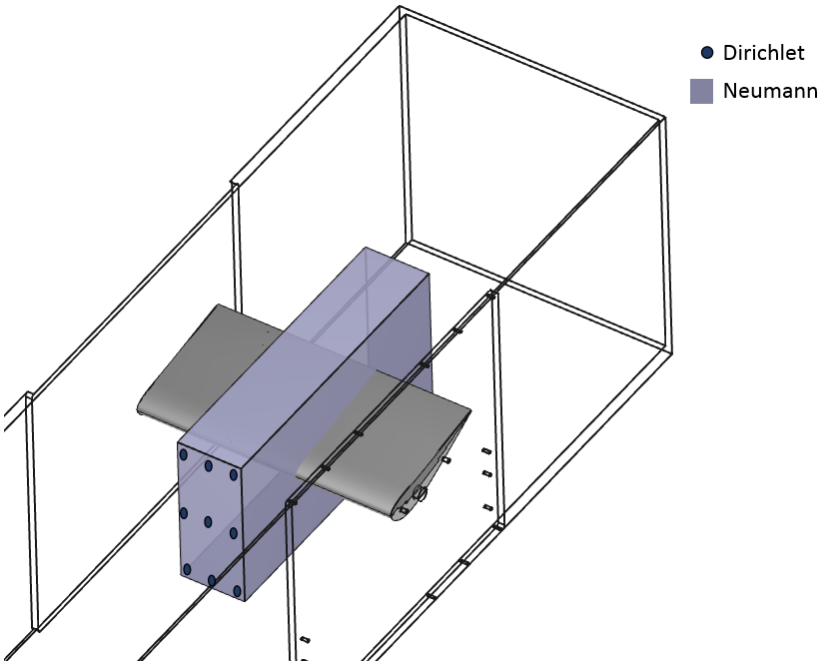

Figure 4.3: Illustration of the domain used to reconstruct pressure and the boundary conditions applied

4.5. Blockage Correction

Since the test section is of closed type, the model creates an obstruction to the flow, decreasing the cross-sectional area of the test section. For the mass flow to remain conserved, the airflow speeds up locally where the cross-section is reduced. This naturally has an effect on the velocity and pressure field and hence needs to be corrected. The modified velocity can be estimated by:

$$u_2 = u_1 \frac{L^2}{(L-d)^2} \tag{4.5}$$

where u_2 is the velocity in the vicinity of the model, u_1 is the set freestream velocity, L is the length of the side of the square test section and d is the maximum thickness of the model.

In this case, $L = 0.4m$, $d = 0.04m$ and $u_1 = 10m/s$, leads to $u_2 = 11.1m/s$. This is particularly important while setting the reference for calculating the pressure co-efficient.

4.6. Estimating Loads from Obtained Pressure

Since the model in this experiment is an airfoil with a constant cross-section and spanning the entire test section, it can be approximated as a 2D airfoil, rather than a finite wing. The normal force per unit span can be obtained by integrating the pressure distribution and is given by(Anderson, (2015)):

$$N = \int_{LE}^{TE} (p_l cos\theta - \tau_l sin\theta) ds_l - \int_{LE}^{TE} (p_u cos\theta - \tau_u sin\theta) ds_u \tag{4.6}$$

where the subscripts 'l' and 'u' are for lower and uppers surface respectively. Neglecting the shear stress contribution to normal force and rewriting the equation in dimensionless form:

$$C_N = \frac{1}{c} \int_0^c (C_{P_l} - C_{P_u}) dx \tag{4.7}$$

where, c is chord length as shown in Fig. 4.4. The lift co-efficient can be further computed by:

$$C_L = C_N cos(\alpha) - C_A sin(\alpha) \tag{4.8}$$

where, α is the angle of attack and C_A is the co-efficient of force in the axial direction, which multiplied by $sin(\alpha)$ is negligible for small angles and hence is not considered.

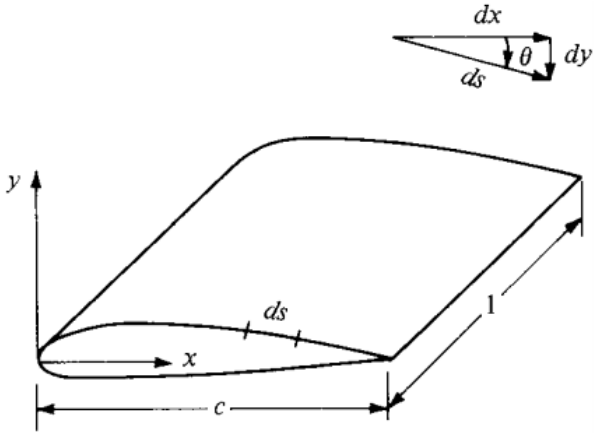

Figure 4.4: Illustration of the orientation used to calculate forces, duplicated from Anderson, (2015)

The obtained loads are compared against those obtained using *XFOIL*[2]. For the *XFOIL* calculation, the Reynolds number is set to 140,000 and N_{crit} is 9.0, with forced transition on the suction side at 5% of the chord length from the leading edge. The C_P distribution obtained from *XFOIL* is used to generate the loads using a *MATLAB* script, so that the methodolgy of load estimation from C_P is same. To ensure a comparison as close as possible, the C_P is sampled from CVV generated pressure field at exactly the same points as those of the *XFOIL* panels. Furthermore, the pressure distribution obtained from pressure taps is also used to estimate loads in a similar manner and the results are presented in Chapter 5.

[2] https://web.mit.edu/drela/Public/web/xfoil/

5

Results and Discussion

This chapter presents and discusses the results obtained from the experiment discussed in Chapter 3 and the data obtained through the techniques described in Chapter 4. The initial sections deal with convergence analysis and the spatial resolution the velocity fields obtained for each configuration and the choice of appropriate bin size. It is followed by the comparison of pressure. Towards the end of the chapter, the loads estimated are presented.

The axis system which is followed throughout the chapter is shown in Fig. 5.1. The origin is placed on the leading edge of the airfoil with X-axis in the streamwise direction, Y-axis in the spanwise direction and Z-axis as shown. Since the flow can be assumed to be largely two dimensional, the results presented are on the plane Y=0 mm.

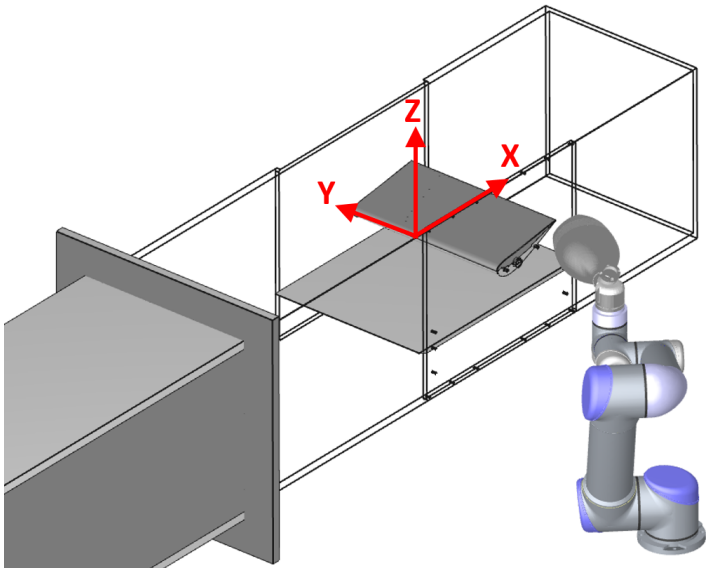

Figure 5.1: Representation of the axis system

5.1. Convergence Analysis

In this section, the statistical convergence of processed data is assessed by comparing the magnitude of velocity at a particular location in the domain obtained using different number of samples. The locations of the bins considered are shown in Fig. 5.2:

- Location 1 (X,Y,Z) = (-50,0,0) mm
- Location 2 (X,Y,Z) = (40,0,-30) mm
- Location 3 (X,Y,Z) = (300,0,25) mm

The velocities are obtained by considering 100, 500, 1000, 2500, 5000, 10000, 15000 and 20000 frames and bin sizes of 25 mm, 20 mm, 15 mm, 10 mm and 5 mm. The plots of velocity magnitude against number of frames for each bin size are discussed further.

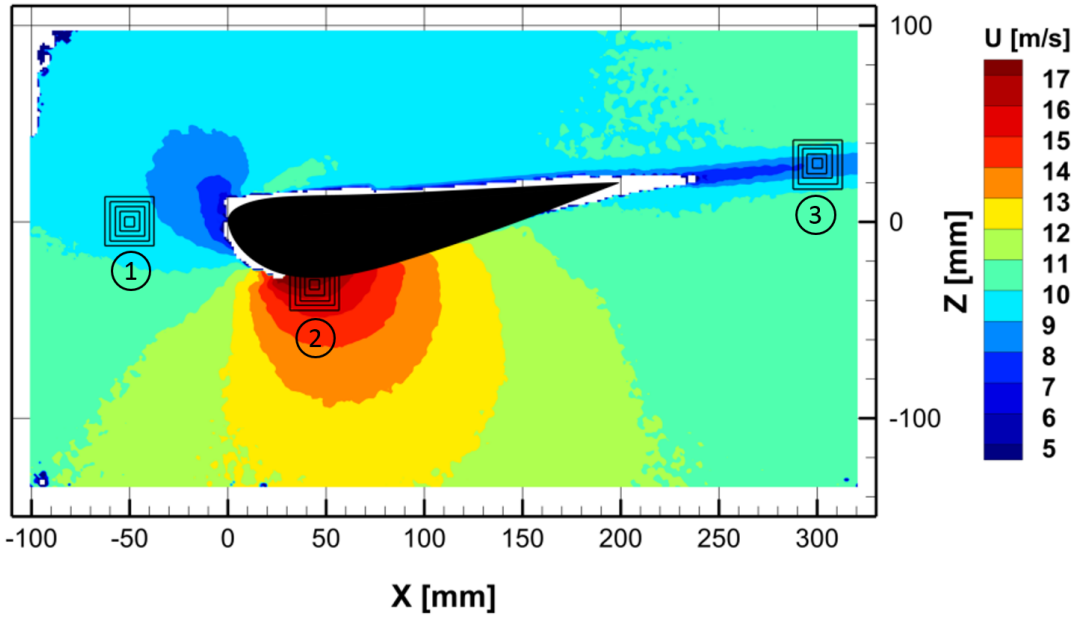

Figure 5.2: Locations of bins consider for convergence analysis

In Fig. 5.3, the bin at location 1 shown in Fig. 5.2 is considered. It can be observed that the velocity at this location does not vary significantly with number of samples considered. Even considering the maximum variation, which is seen for the bin size of 10 mm, it is approximately around 1%.

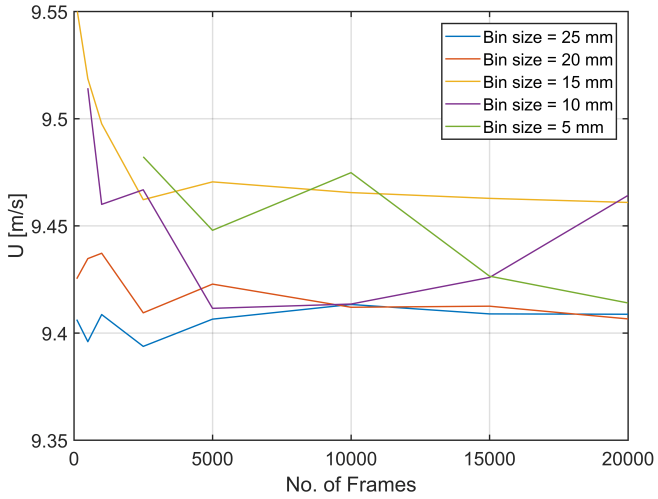

Figure 5.3: X-Velocity(u) measured at location 1 shown in Fig. 5.2

Similarly, in Fig. 5.4, the bin at location 2 is considered. For the larger bin sizes namely, 25 mm, 20 mm and 15 mm, the velocity computed using small number of images (<5000) is lower by about 8-10%, compared to that computed using higher number of images. For the smaller bin sizes of 10 mm and 5 mm, the maximum variation is 2.8%.

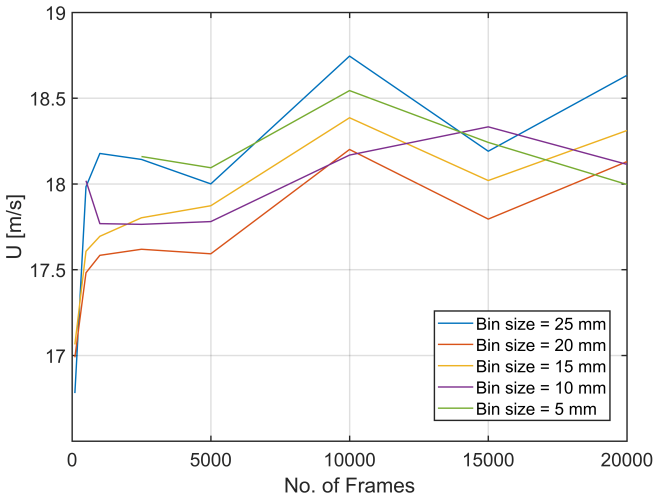

Figure 5.4: X-Velocity(u) measured at location 2 shown in Fig. 5.2

The most critical case in terms of convergence is the bin at location 3 as it is located in the region of wake-shear layer. In Fig. 5.5, the velocities computed are compared. One clear observation that can be made is that the larger bin sizes compute an average velocity higher than those by the smaller bins. This is due to the higher velocities outside the wake region being averaged in the same bin. However, considering any particular bin size, the variation in average velocity with different number of images is between 3-5 %.

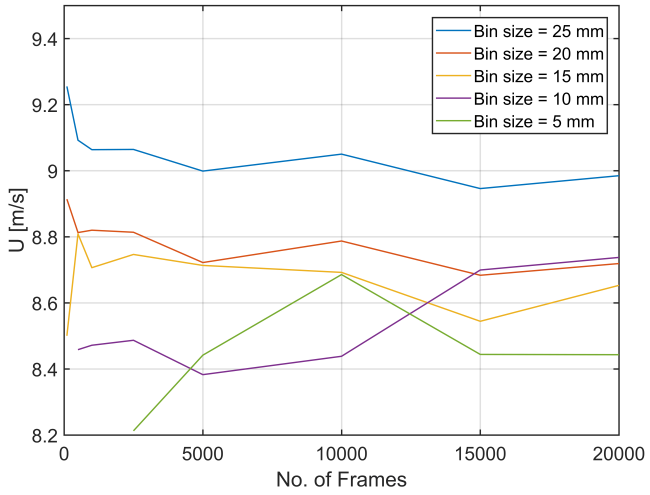

Figure 5.5: X-Velocity(u) measured at location 3 shown in Fig. 5.2

To sum up, it can be concluded that the acquisition of 5000 images permit to reduce the variation of average velocity magnitude to the range of $1-2\%$, considered acceptable. However, it affects the spatial resolution. In all of the above cases, the data processing did not yield results for smaller bins sizes of 10 mm and 5 mm using smaller number of images (100 and 500). The criteria of minimum number of particles found (5 particles per bin) was not satisfied and hence the bins were invalidated. As explained in Section 2.3, the instantaneous spatial resolution obtained by the HFSB is of the order of inter-particle distance, but the time-averaged resolution can be further improved by increasing the number of samples. The effects of spatial resolution are discussed further.

5.2. Spatial Resolution

In this section, the reasoning behind the choice of spatial resolution of the time averaged velocity data is discussed. Considering the kind of data acquired, the spatial resolution depends on two main parameters, the number of frames sampled and the bin size. For a fixed number of frames, bin size plays a major role in deciding the spatial resolution. A comparison of the velocity field obtained using bin sizes of 25 mm, 20 mm, 15 mm 10 mm, 5 mm and 3 mm is presented.

From the contour plots in Fig. 5.6, we observe the qualitative differences. Smaller the bin size, better is resolution of the velocity gradients. The case of bin size of 3 mm is shown in Fig. 5.6f. Major part of the domain, specially close to the model, did not satisfy the validity condition of 5 particles per bin and hence the final results presented are for the bin size of 5 mm. To understand the quantitative effects, velocity measured along different lines of the domain are studied.

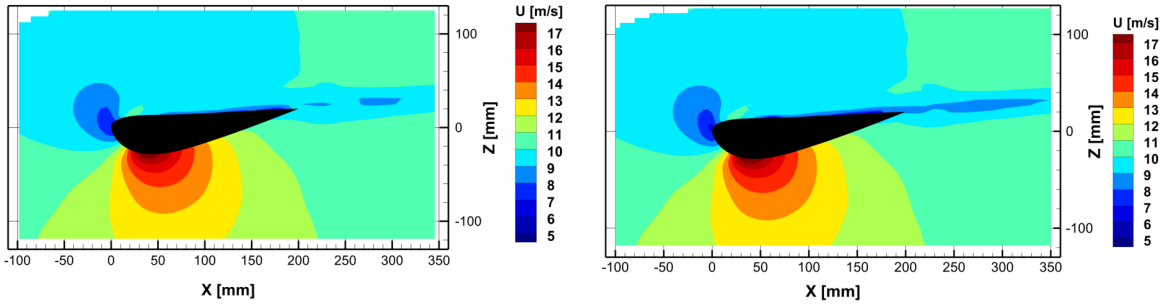

(a) Bin size = 25 mm

(b) Bin size = 20 mm

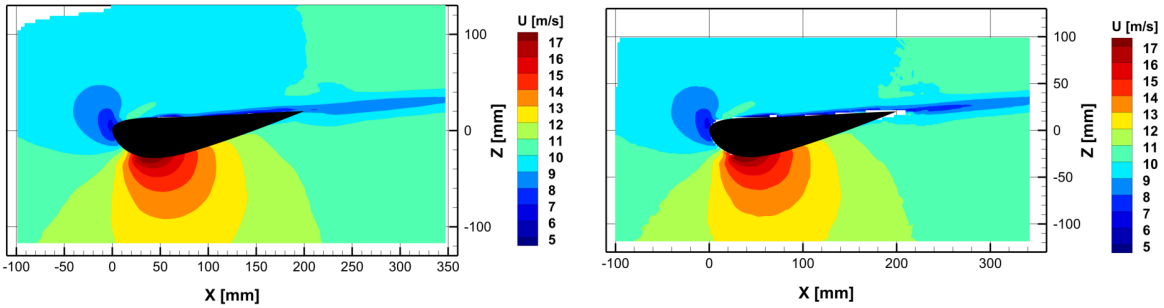

(c) Bin size = 15 mm

(d) Bin size = 10 mm

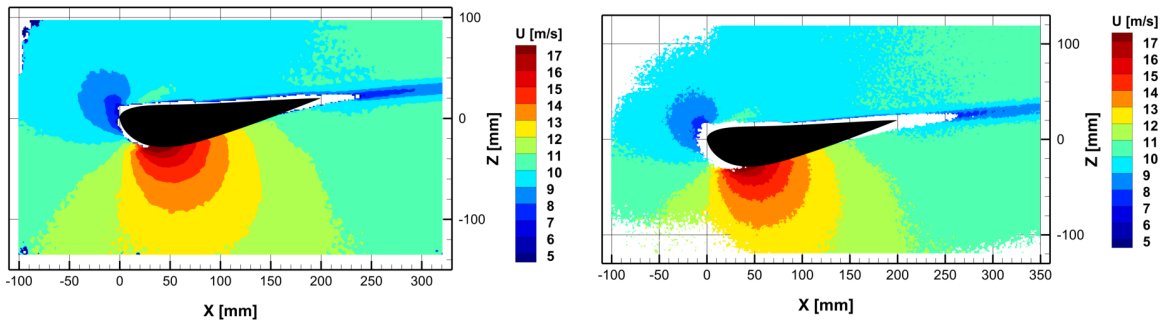

(e) Bin size = 5 mm

(f) Bin size = 3 mm

Figure 5.6: Illustration of differences in contour plots for different bin sizes

In Fig. 5.7a, information of velocity in the wake is extracted along a line in Z-direction at x=300 mm. This plot clearly depicts the effect of bin size on spatial resolution which also affects the magnitude

of velocity computed. It is observed that the wake is approximately 30 mm in thickness and shows strong variation of velocity. Considering a bin size of 25 mm, it will have particles with a higher range of velocities, which will be averaged in that single bin. Particles having velocity of 10 m/s and 8 m/s will be considered in a single bin and would affect the accuracy due to averaging. It is clearly seen from the plot that for the bin size of 25 mm, the minimum velocity is around 9 m/s. However, as the bin size reduces, the magnitude of minimum velocity computed also decreases. This is because smaller regions of the domain are considered for averaging. The minimum velocity computed for the case of 5 mm is around 8 m/s as can be seen. However, the bin size of 5 mm shows slight noisy behaviour due to spatial modulation effects. However, these variations are about 0.1 m/s, which is acceptable. But, these effects are significantly stronger for the bin size of 3 mm. They are in the range of 0.5 m/s, with no added benefit. The results obtained using the bin size of 5 mm capture the velocity deficit in the wake accurately.

Fig. 5.7b shows the number of particles in the wake. A common trend follows for all bin sizes. The number of particles is lower in the wake due to the lower velocity. Even in this plot, the smaller bin sizes show the noisy behaviour, especially for the bin size of 3 mm.

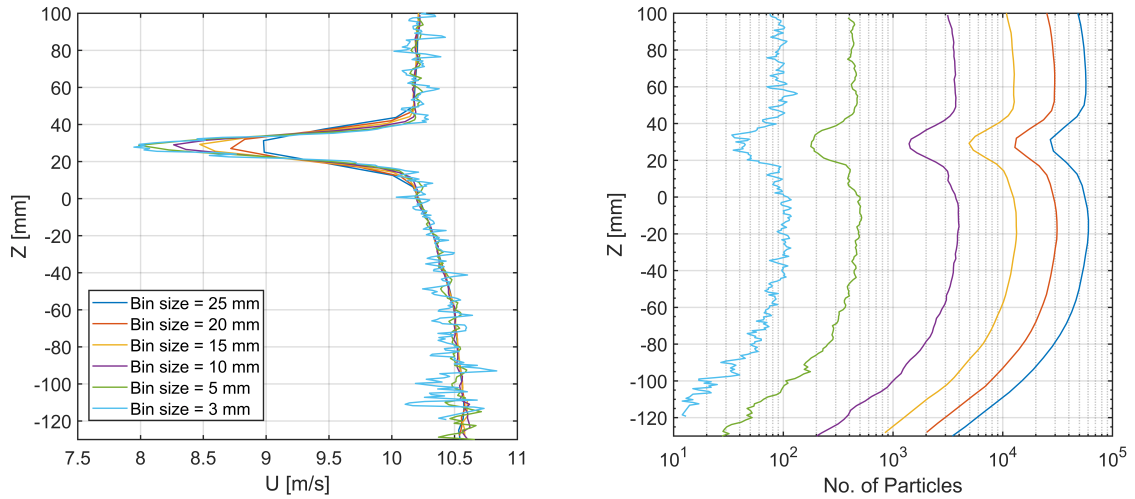

(a) X-Velocity(u) measured in the wake along Z-direction at x=300 mm

(b) Number of particles measured in the wake along Z-direction at x=300 mm

Figure 5.7: Illustration of differences in velocity profiles and number of particles detected for different bin sizes in the wake

The Fig. 5.8a shows the comparison of velocity profiles along a line in Z-direction at x=40 mm for different bin sizes. This is in the region of maximum velocity on the suction side of the airfoil. Due to the gradients being small, the differences are marginal compared to those in the wake. Nonetheless, the smaller bin size yields more information. As seen in the case of wake as well, the noisy fluctuations in velocity can be observed for bin size of 3 mm.

From Fig. 5.8b, it can be observed that the number of particles drops sharply towards the surface of the model. The plot for bin size of 3 mm is very noisy and does not yield results for the entire domain as can be seen in Fig. 5.6f.

In Fig. 5.9a, the velocity profiles along a line along X-direction at z=0 mm are compared for different bin sizes. This is the stagnation region of the airfoil. A clear trend that can be observed is that the minimum velocity decreases in magnitude with decrease in bin size. This is similar to the effect of averaging particles with significantly varying velocities, in the same bin as explained above. The averaging is further illustrated using Fig. 5.10 where bin sizes of 10 mm and 5 mm are compared. However, smaller bin sizes come with the disadvantage of noise, which can be seen in both Fig. 5.9a and Fig. 5.9b for the case of 3 mm.

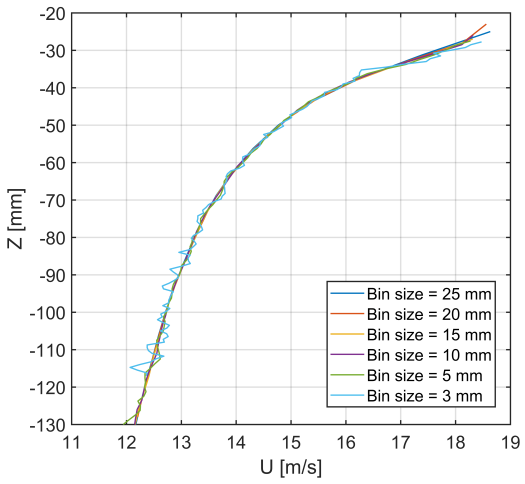

(a) X-Velocity(u) measured in the region of maximum velocity along Z-direction at x=40 mm

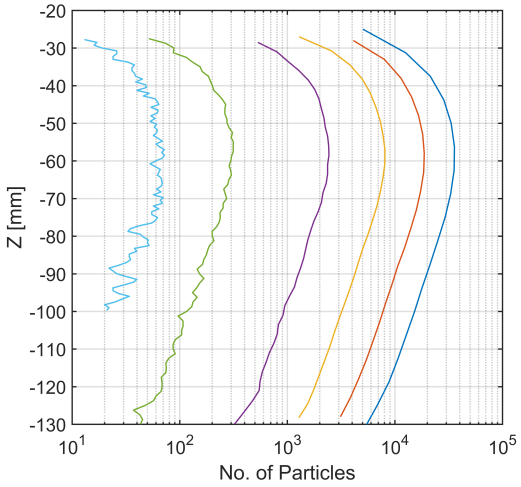

(b) Number of particles measured in region of maximum velocity along Z-direction at x=40 mm

Figure 5.8: Illustration of differences in velocity profiles and number of particles detected for different bin sizes in the region of maximum velocity

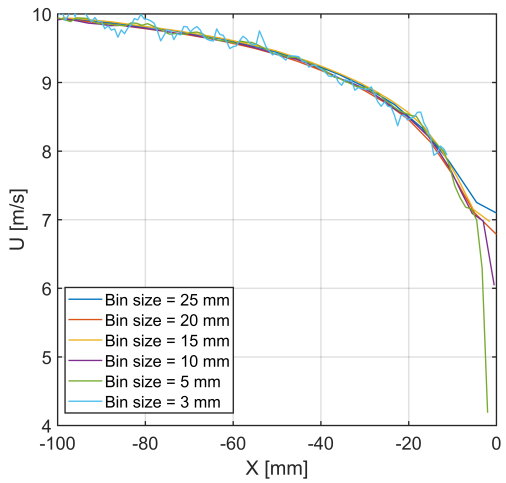

(a) X-Velocity(u) measured in the wake along X-direction at z=0 mm

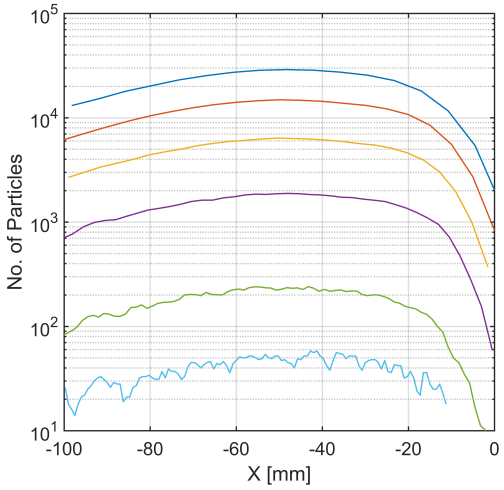

(b) Number of particles measured in the wake along X-direction at z=0 mm

Figure 5.9: Illustration of differences in velocity profiles and number of particles detected for different bin sizes along z=0

The radius of curvature of the leading edge itself is approximately 10 mm and the stagnation region is even smaller (illustrated in Fig. 5.10). Hence, a bin in that region, will have particles that stagnate as well as those which flow over the pressure side and accelerate towards the suction side. But these will be averaged into one single bin and hence will affect the accuracy of measurements. An improvement in this is seen for the bin size of 5 mm. However, in this case, the number of particles per bin is lower, especially close to the surface and hence do not satisfy the validity criteria of the bin. But these distances are in the region of 1 mm - 2 mm from the surface and only affect a small part of the velocity field. Hence, in the subsequent part of this chapter, bin size of 5 mm is used. Furthermore, an overlap of 75% is also used so that there is a data-point every 1.25 mm of the field.

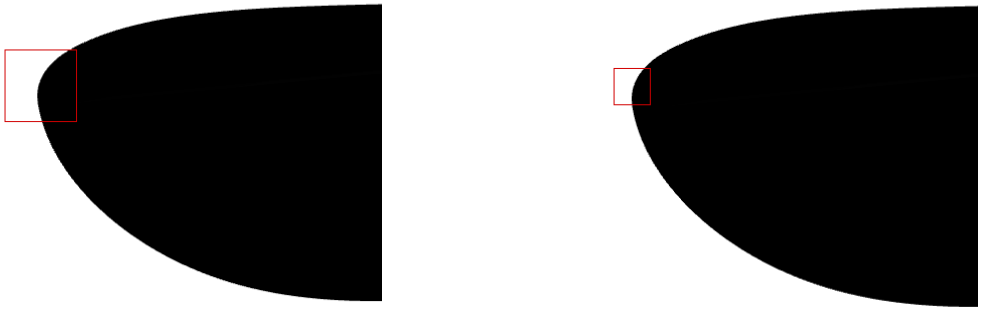

(a) Bin size = 10 mm (b) Bin size = 5 mm

Figure 5.10: Illustration of bin size compared against the leading edge curvature

5.3. Velocity Contours

In this section, the velocity fields for each configuration are discussed. The clearance h between the airfoil and the ground plane is normalized by the chord length c and expressed as h/c.

5.3.1. α=5°; No Ground Effect(h/c=1)

Fig. 5.11 shows the velocity field for angle of attack of 5° with no ground effect. The contour depicts the flow features around a typical airfoil very clearly, namely - leading edge stagnation, acceleration on suction side and velocity deficit in the wake. The upwash produced is shown by the streamlines.

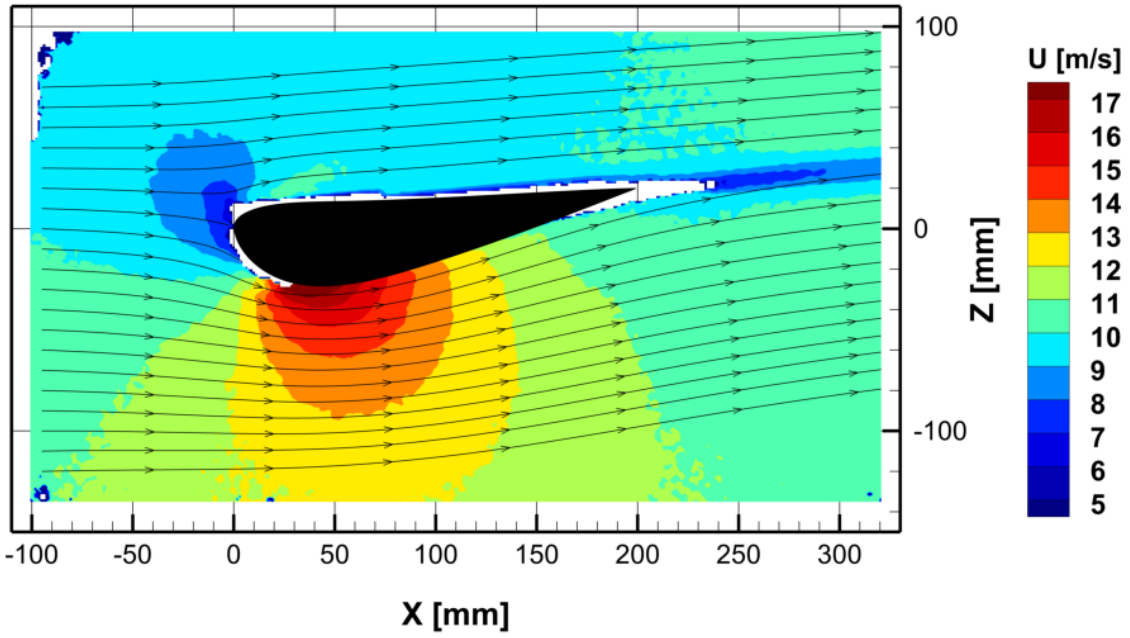

Figure 5.11: X-Velocity(u) contour for $\alpha = 5°$ and no ground effect

The blanked zone indicates the lack of particles found in the region. Near the leading edge, the blanking is approximately 2-3 mm from the surface. The quantitative information obtained from the above contour plot is discussed further.

In Fig. 5.12, the X-velocity(u) is plotted along a line in the Z-direction in the region of maximum velocity on the suction side of the wing. The maximum velocity, close to the surface is slightly over 18 m/s while the lowest is 12 m/s at Z=-130 mm. The gradient of velocity(u) in the 30 mm closer to the surface (Z=-60 to -30 mm), is much higher that the region further away. It is even more pronounced in

the initial 10 mm close to the surface (Z=-40 to -30 mm), where the velocity goes from 16 m/s to 18 m/s.

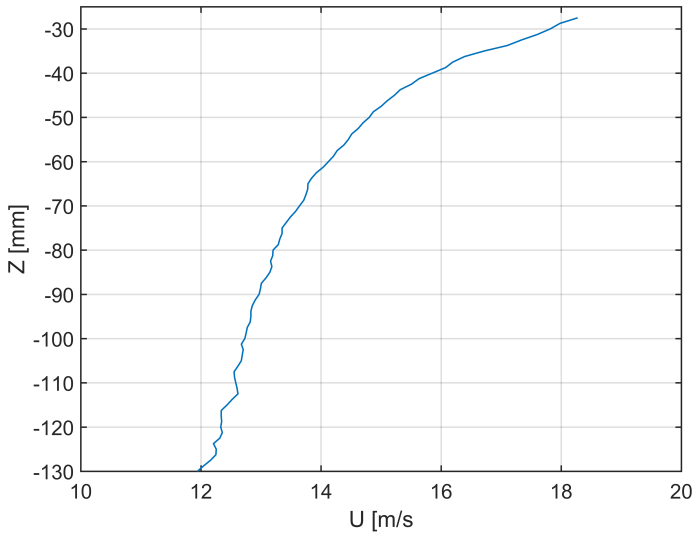

Figure 5.12: X-Velocity(u) profile at x=40 mm for $\alpha = 5°$ and no ground effect

A similar X-velocity(u) profile of the wake is plotted along Z-direction in Fig. 5.13. The velocity deficit is observed in a region with thickness of 20 mm, with minimum velocity of 8 m/s. Another distinct observation which can be made is that outside the wake, the velocity below it (suction side of the wing) is slightly higher than that above (pressure side), as expected.

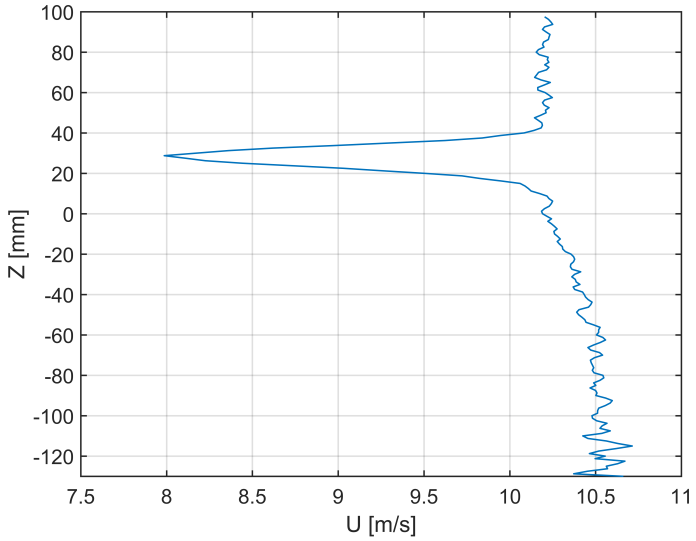

Figure 5.13: X-Velocity(u) profile at x=300 mm for $\alpha = 5°$ and no ground effect

5.3.2. α=5°; Moderate Ground Effect (h/c=0.6)

The Fig. 5.14 shows the X-velocity(u) contour for angle of attack of 5° and ground plane at $h/c = 0.6$. There are no significant qualitative differences compared to the no ground effect case. The blanked region towards the trailing edge is much larger due to the limitation of optical access. The quantitative features are discussed below.

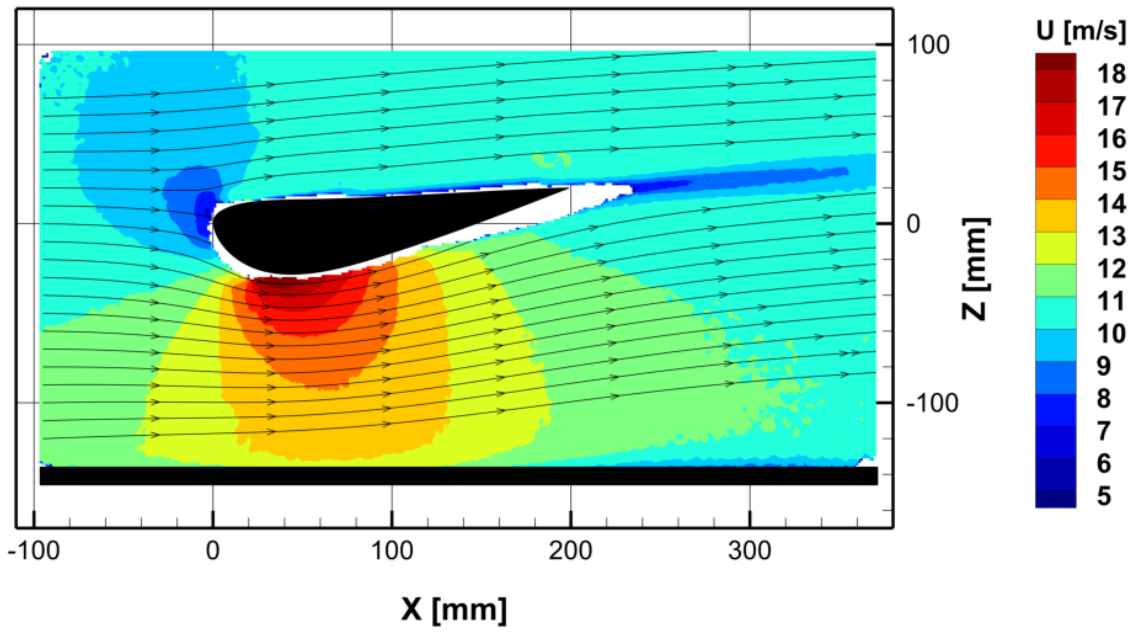

Figure 5.14: X-Velocity(u) contour for $\alpha = 5°$ and $h/c = 0.6$

The Fig. 5.15 shows the X-velocity(u) profile in Z-direction in the region of maximum velocity on the suction side. The trend of the change in velocity is similar to that of the no ground effect case. However, the velocities in both extremities of the plot are higher. The maximum velocity, close to the surface of the wing is 19 m/s in this case, whereas that at -130 mm is 13 m/s.

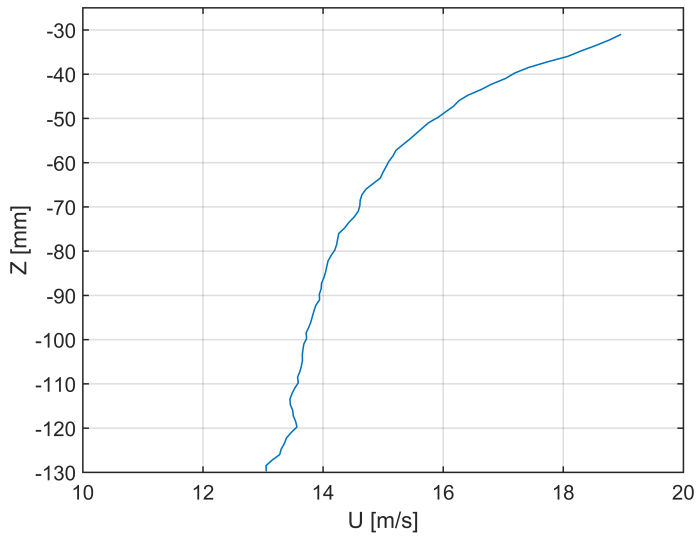

Figure 5.15: X-Velocity(u) profile at x=40 mm for $\alpha = 5°$ and $h/c = 0.6$

Fig. 5.16 shows the X-velocity(u) profile in the wake. The minimum velocity is approximately 8.5 m/s. Closer to the ground plane, the velocity deficit is clearly visible. This is due to the boundary layer growth as well as the upwash produced by the wing. This effect is more pronounced in the next configuration, where the ground effect is stronger.

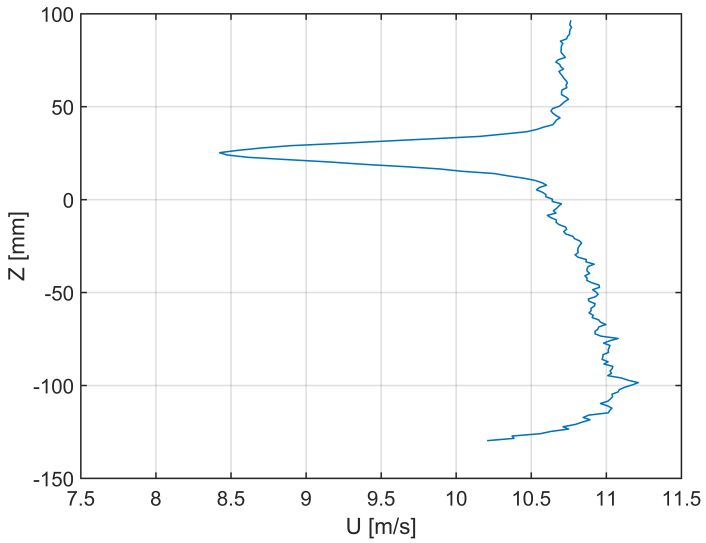

Figure 5.16: X-Velocity(u) profile at x=300 mm for $\alpha = 5°$ and $h/c = 0.6$

5.3.3. α=5°; Strong Ground Effect (h/c=0.3)

Fig. 5.17 shows the X-velocity(u) contour for $\alpha = 5°$ and $h/c = 0.3$, the strongest ground effect configuration in this experiment. Similar to the previous ground effect configuration, there is a lack of information close to the trailing edge of the wing due to limitation of optical access.

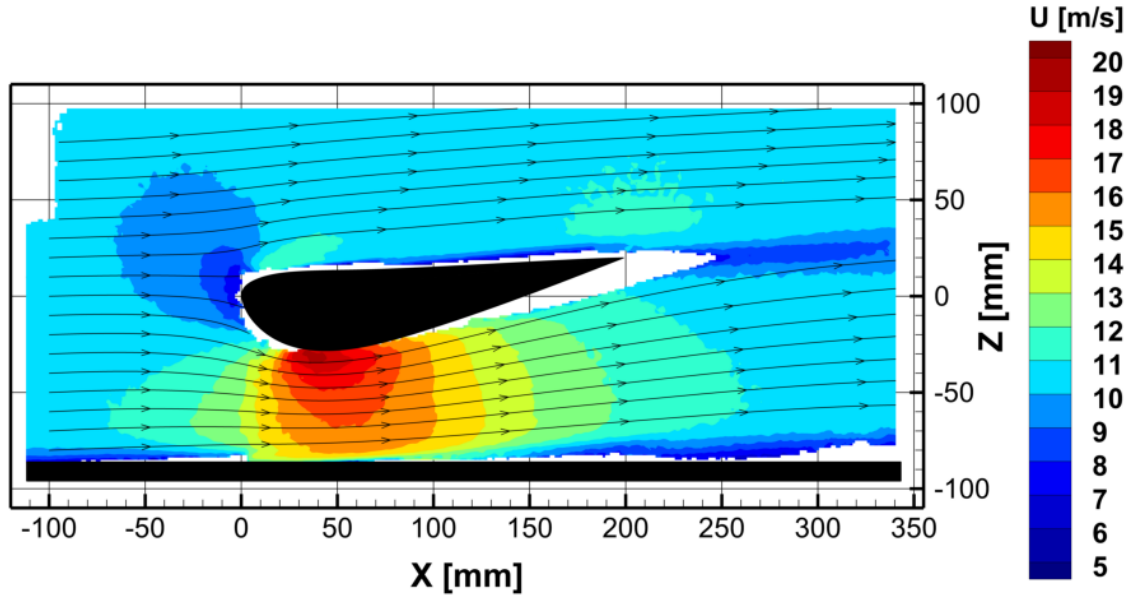

Figure 5.17: X-Velocity(u) contour for $\alpha = 5°$ and $h/c = 0.3$

Fig. 5.18 shows the X-velocity(u) profile for the strong ground effect ($h/c = 0.3$) configuration. A distinct feature of this plot, is the overall higher velocity between the wing and the ground plane. The maximum velocity close to the surface is approximately 19.5 m/s. The plot also shows a sudden reduction in velocity, reaching almost 10 m/s close to the ground plane. This is caused due to the growth of boundary layer on the plane, which is also seen in the contour plot. Outside this shear layer, the minimum velocity is 15 m/s, which is considerably higher compared to the other two configurations.

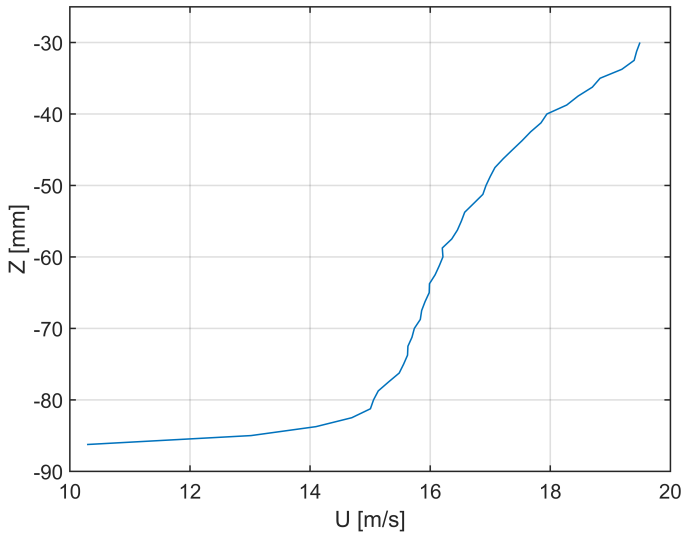

Figure 5.18: X-Velocity(u) profile at x=40 mm for $\alpha = 5°$ and $h/c = 0.3$

A plot showing the X-velocity profile(u) in the wake for $\alpha = 5°$ and $h/c = 0.3$. The boundary layer growth is clearly visible in this plot as well. The minimum velocity in the wake is 8.5 m/s. Unlike other configurations, the velocity on the lower side of the wake is slightly lower than that on the higher. This can be attributed to a double shear caused by the boundary layer as well as the wake. As the ground clearance is lowered further, this boundary layer eventually merges with the boundary layer growth on the wing, causing flow separation and an enlarged deficit region in the wake.

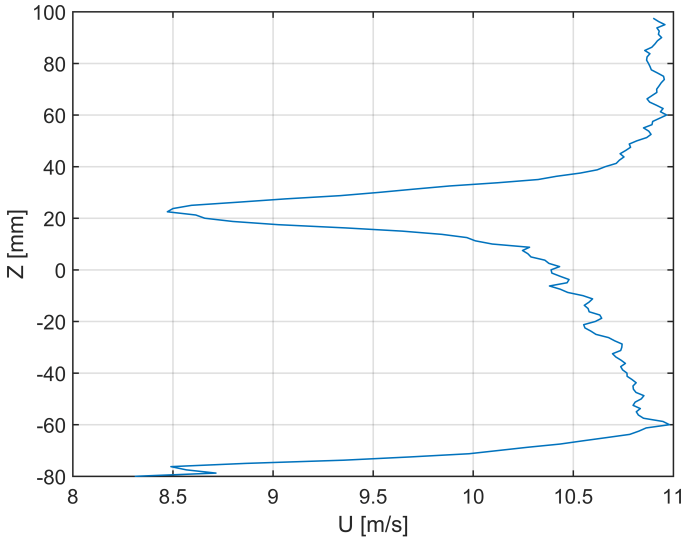

Figure 5.19: X-Velocity(u) profile at x=300 mm for $\alpha = 5°$ and $h/c = 0.3$

5.3.4. α= 8°; No Ground Effect ($h/c = 1$)

Fig. 5.20 shows the X-velocity(u) contour for the configuration of $\alpha = 8°$ and $h/c = 1$. The lower maximum velocity and a larger wake region indicate the presence of flow separation on towards the aft of the wing. This is further analysed using velocity profiles.

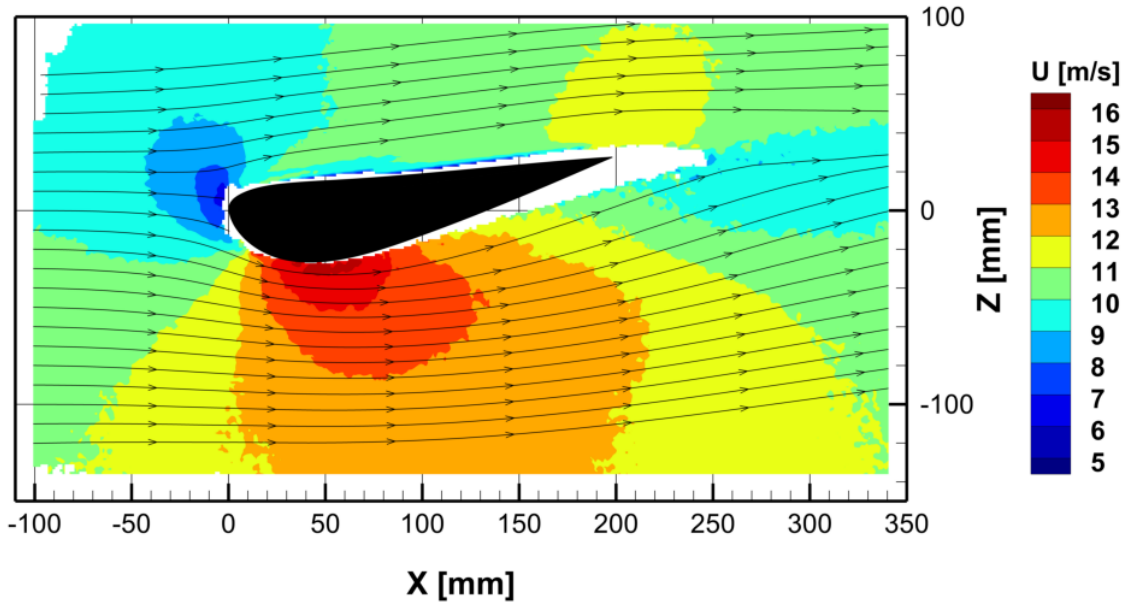

Figure 5.20: X-Velocity(u) contour for $\alpha = 8°$ and no ground effect

The velocity profile in the region of maximum suction is shown in Fig. 5.21. The maximum value close to the surface is 15.5 m/s and the minimum is 12 m/s. Compared to all the cases of $\alpha = 5°$, the maximum velocity is significantly lower.

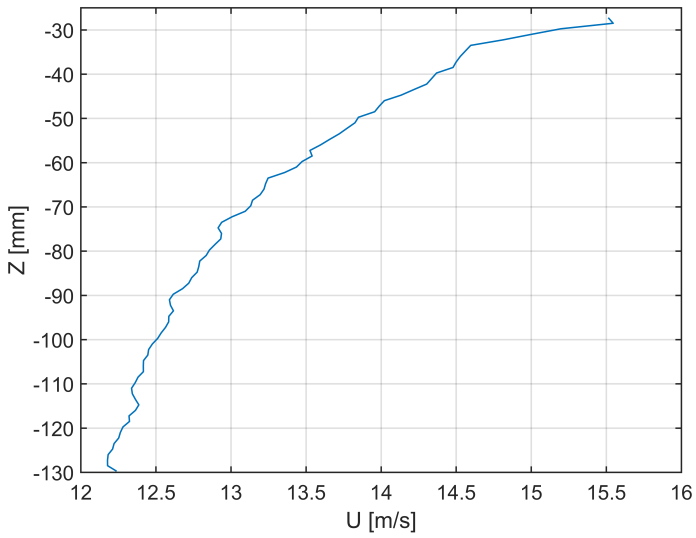

Figure 5.21: X-Velocity(u) profile at x=40 mm for $\alpha = 8°$ and no ground effect

Fig. 5.22 shows the plot of X-velocity(u) in the wake. A distinct feature of this plot is the thickness of the wake, which is approximately 100 mm; much larger as the flow is separated. The minimum velocity is around 9.5 mm but unlike the previous cases, shows a lot of variation as the flow is highly unsteady in this region. Outside the wake, especially in the lower part, the velocity is higher, around 11.25 m/s. This can be attributed to the effect of wake blockage, since the test section is of closed type.

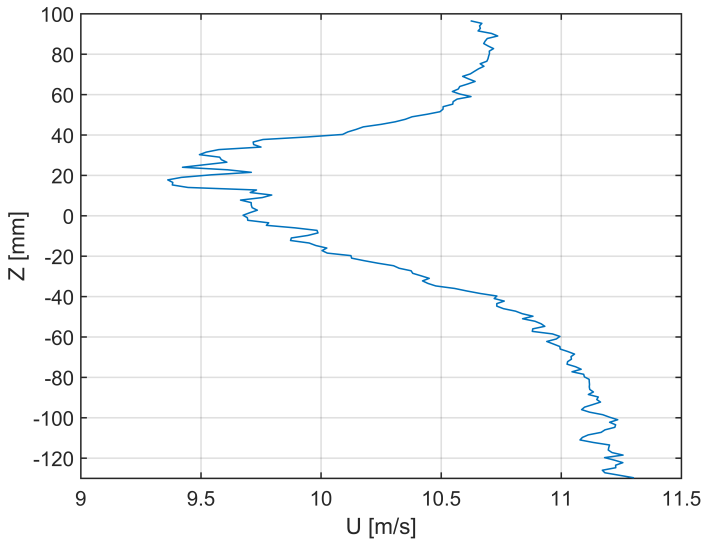

Figure 5.22: X-Velocity(u) profile at x=300 mm for $\alpha = 8°$ and no ground effect

5.4. Comparison of Pressure

In this section, the contours of pressure coefficient C_P for each configuration are presented. A further comparison between the direct pressure measurements and that from CVV by using Poisson and Bernoulli's equation, is also shown. In the region towards the trailing edge, the pressure from CVV is obtained by linearly extrapolating the data towards the surface. Also, it is worth noting that in this region, the gradients in the surface-normal direction are small and hence extrapolation will not affect the accuracy by a lot.

5.4.1. α=5°; No Ground Effect(h/c=1)

Fig. 5.23 shows the contour plot of the pressure coefficient(C_P for $\alpha = 5°$ and $h/c = 1$. In the stagnation region, the maximum value of pressure coefficient is close to 0.4. The minimum C_P in the suction region is around -1.75. The pressure side of the wing is very flat and hence there is no significant increase in pressure.

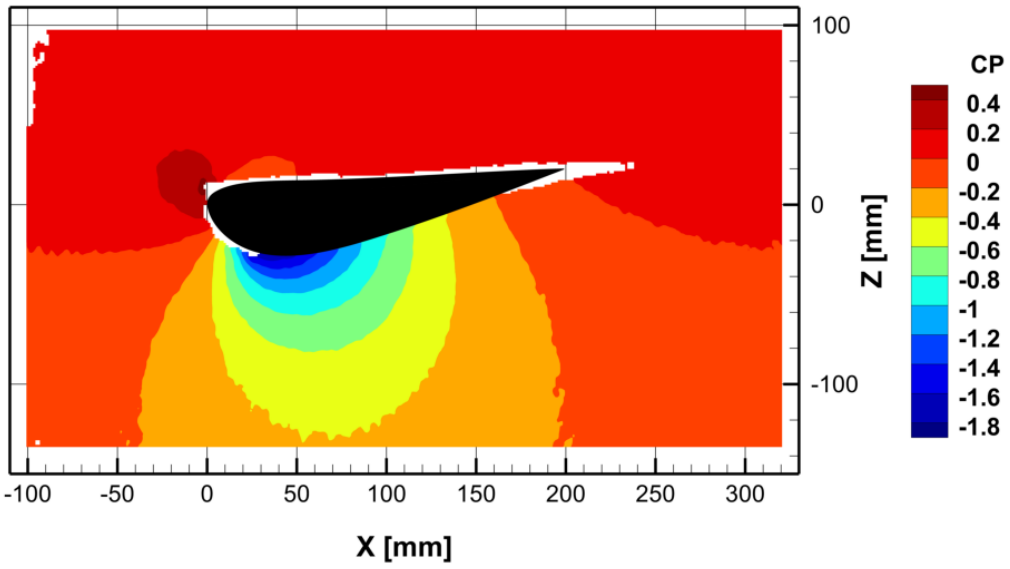

Figure 5.23: Coefficient of pressure C_P contour for $\alpha = 5°$ and $h/c = 1$

The comparison of surface pressure obtained using pressure taps and that reconstructed from CVV is shown in Fig. 5.24. The C_P computed using Bernoulli's equation is also shown by the scatter (green diamonds). The stagnation region shows the most disagreement, where CVV is not able to measure stagnating flow. However, using the same velocity field data, the C_P computed using Bernoulli's equation is higher (0.73) and hence more closer to the data obtained from pressure taps. The suction side, especially the suction peak region shows a very good agreement between pressure taps, CVV using Poisson's equation and also that using Bernoulli's equation. Aft of the suction peak region, there is difference between the measurements, where pressure taps indicate a separation towards the trailing edge. However, the CVV pressure does not indicate such a strong gradient and gradually approaches freestream pressure ($C_P = 0$) towards the trailing edge.

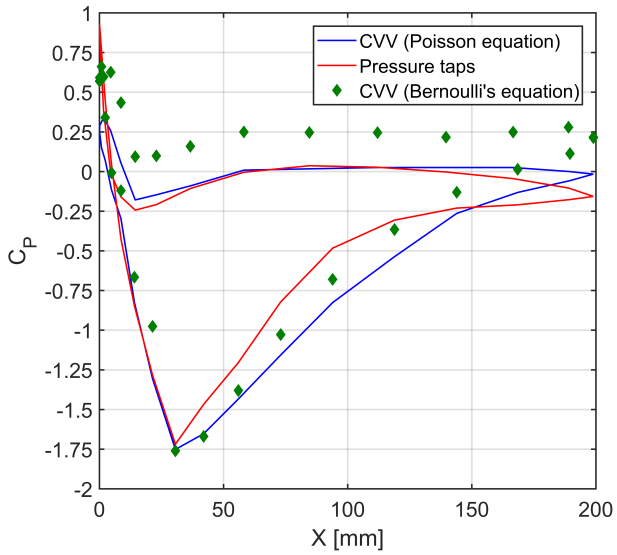

Figure 5.24: Comparison of point-wise static pressure measured by pressure taps and CVV pressure for $\alpha = 5°$ and $h/c = 1$

5.4.2. α=5°; Moderate Ground Effect (h/c=0.6)

The contour plot of pressure coefficient (C_P) for $\alpha = 5°$ and $h/c = 0.6$ is shown in Fig. 5.25. Similar to the previous configuration, the stagnation zone shows the max C_P between 0.3-0.4. The region of suction shows a slight increase, but overall no significant differences are observed.

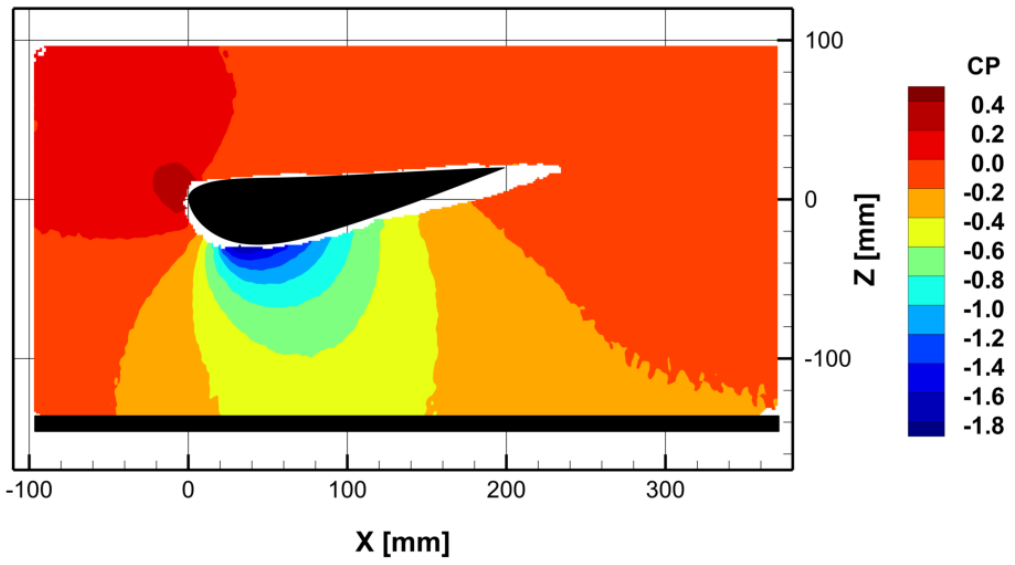

Figure 5.25: Coefficient of pressure C_P contour for $\alpha = 5°$ and $h/c = 0.6$

The surface pressure obtained using the pressure taps and CVV is compared in Fig. 5.26. Even in this case, the differences in the values C_P by pressure taps and CVV are mainly in the stagnation region and aft of the suction peak. The C_P has a value of approximately -1.9 at the suction peak. The pressure obtained by Bernoulli's equation shows a better agreement with that from pressure taps on the suction side. However, it shows relatively larger disagreement for the pressure side.

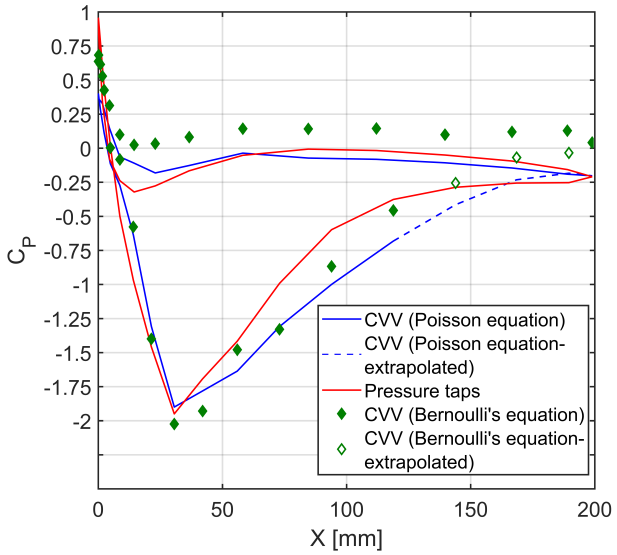

Figure 5.26: Comparison of point-wise static pressure measured by pressure taps and CVV pressure for $\alpha = 5°$ and $h/c = 0.6$

5.4.3. α=5°; Strong Ground Effect (h/c=0.3)

Fig. 5.27 shows the pressure coefficient(C_P) contour for the strong ground effect configuration. The overall increase in the region of low pressure below the wing can be clearly observed.

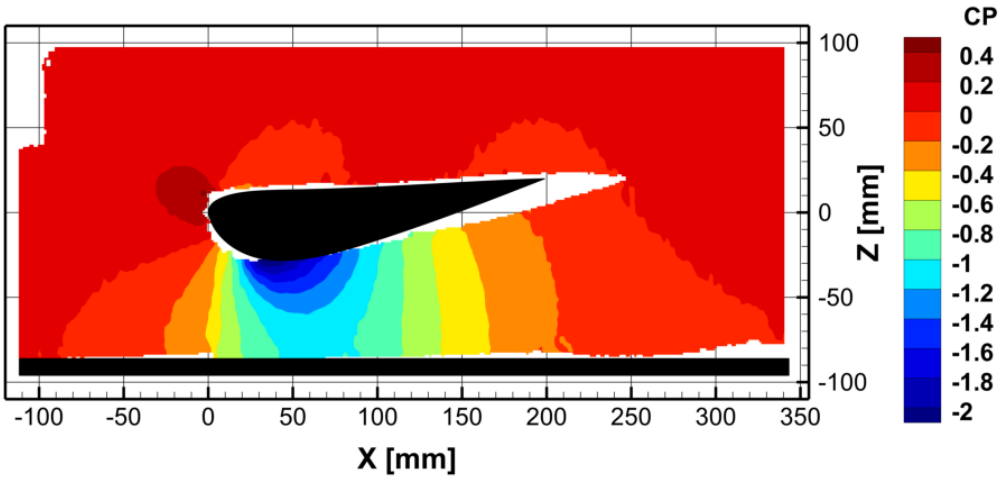

Figure 5.27: Coefficient of pressure C_P contour for $\alpha = 5°$ and $h/c = 0.3$

The comparison of surface pressures obtained using pressure taps and CVV is shown in Fig. 5.28. In this plot, the difference between the C_P values for the pressure side is noticeably higher than the previous configurations. Consistent with the previous cases, the pressure taps indicate a stronger adverse pressure gradient compared to that given by the CVV. However, the C_P values computed using Bernoulli's equation from velocities obtained from CVV show a better agreement with pressure taps.

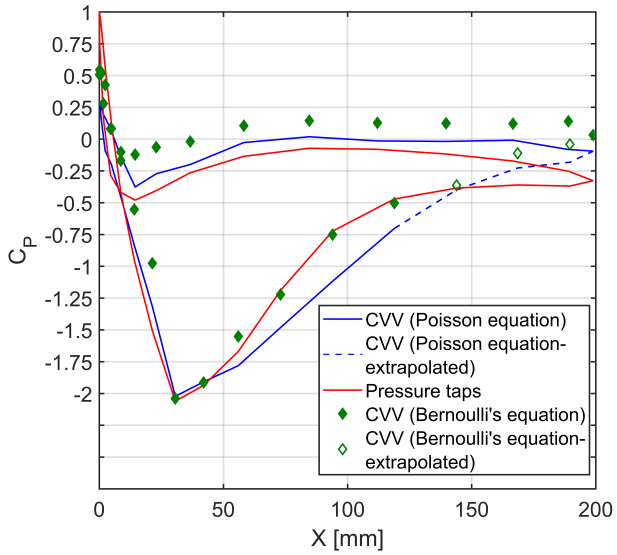

Figure 5.28: Comparison of point-wise static pressure measured by pressure taps and CVV pressure for $\alpha = 5°$ and $h/c = 0.3$

5.4.4. α=8°; No Ground Effect(h/c=1)

Fig. 5.29 shows the pressure coefficient(C_P) contour for $\alpha = 8°$ and $h/c = 1$.

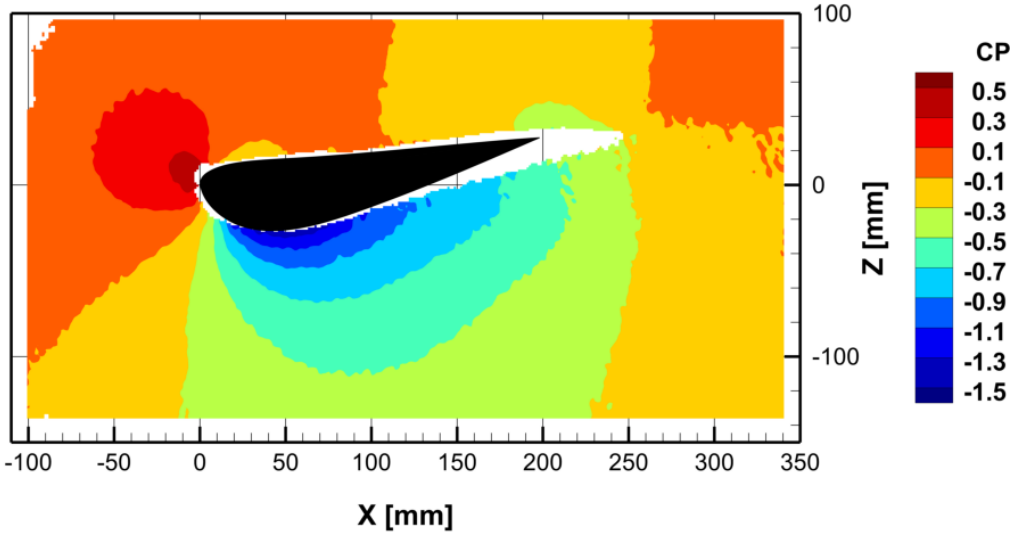

Figure 5.29: Coefficient of pressure C_P contour for $\alpha = 8°$ and $h/c = 0.1$

5.5. General Observations and Remarks

5.5.1. Velocity Plots

The velocity plots obtained using CVV show one common deficiency, compared to pressure taps measurement. The stagnation region is the one which suffers the most in terms of accuracy. In all of the analysed configurations, the minimum velocity barely drops below 5 m/s. The main cause of this is the lack of spatial resolution and method of ensemble averaging. As explained in Section 5.2, the stagnation zone is a very small region with strong velocity gradients. Hence, a single bin has particles with varying magnitude of velocities. All these velocities are averaged into one single bin, hence increasing the average value. Another cause which can possibly add to this issue is the large reflection caused by the leading edge of the wing, when illuminated by the laser. It is clearly seen in Fig. 4.1a.

Another distinct limitation can be seen towards the trailing edge of the airfoil. Apart from the case of $\alpha = 5°$ and $h/c = 1$, all other configurations have a lack of data points. This is mainly due to limited

optical access due to the ground plane. The *MiniShaker* also could not be rotated freely as it would affect the positioning of data as explained in Section 3.5.2. However, simply looking from the rear of the airfoil towards the trailing edge section can potentially eliminate this issue. It can be said that this issue is very specific to this particular experiment and the setup.

5.5.2. Pressure Plots

The surface pressure plots are comparable, however still show differences. The differences in the stagnation region can be attributed to the deficiency in the accuracy of the velocity obtained, which is propagated to pressure reconstruction. The other difference is to the aft of the suction peak region, where CVV indicates a higher overall suction. This might be due to the flows being slightly dissimilar. Simultaneous pressure taps measurement and CVV measurement are not feasible since the pressure taps are contaminated by soap. The initial data given by the pressure taps indicated a leading edge separation and hence a huge disagreement with that obtained from CVV. Hence, a planar PIV experiment was carried out to further investigate this phenomenon. The findings of this are presented in Appendix A. In case of CVV, the leading edge separation is absent and its most plausible explanation can be the accumulation of foam on the model, causing the flow transition and helping it to stay attached. To cause a similar transition, a zigzag strip was added on the suction side of the model at approximately 5% of the chord length from the leading edge. However, this does not ensure completely similar flow conditions.

The pressure computed using Bernoulli's equation shows a better agreement with the pressure taps, especially on the suction side. The disagreement is larger on the pressure side of the wing. From the velocity contours, a thick boundary layer can be observed and hence affects the accuracy of pressure computed using Bernoulli's equation.

5.5.3. Ground Effect

Considering the velocity as well as C_P plots, the ground effect appears to be a very weak. The behaviour of the wing and the trend of increase in the velocity and suction (lower C_P) with decreasing clearance is in-line with the literature. The comparison of the X-velocity(u) profile and surface pressure distribution is shown in Fig. 5.30a and Fig. 5.30b respectively. The overall increase in velocity with reduction in ground effect leads to higher suction peaks, which are clearly observed. However, the magnitudes of the differences is very low. This is mainly due to the fact that the wing is not optimised for the flow conditions (angle of attack, Reynolds's number etc.). The Reynolds's number especially is particularly low (approximately 140000) and hence the flow struggles to stay attached. It was a generic object that was decided to be subjected to this analysis as the aim is to assess the feasibility if surface pressure reconstruct on using CVV and not analysis of this particular wing.

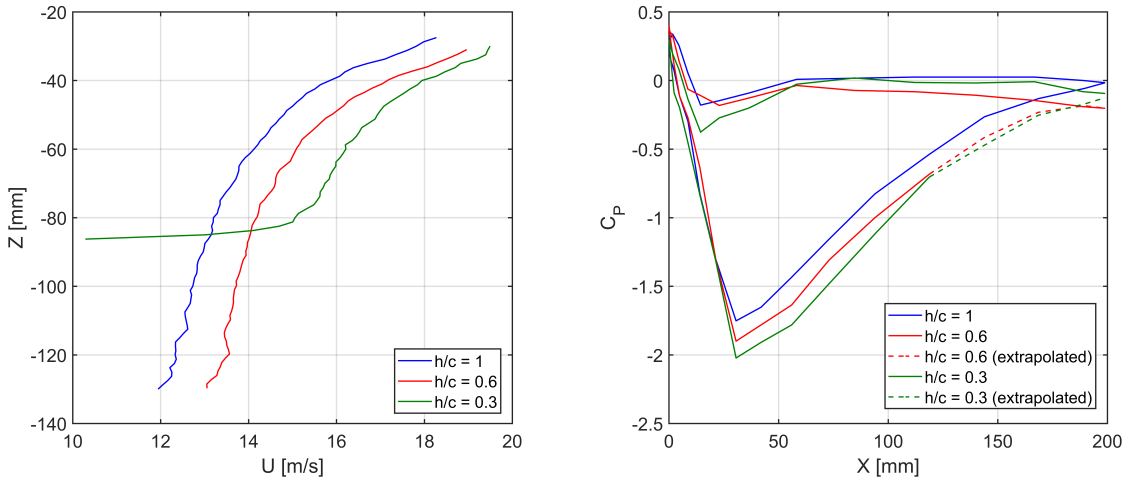

(a) Comparison of X-velocity(u) profiles measured along z=40 mm for different configurations

(b) Comparison of surface pressure (obtained using Poisson solver) for different configurations

Figure 5.30: Illustration of bin size compared against the leading edge curvature

5.6. Estimated Loads

The obtained pressure distribution around the wing allows to estimate for the negative lift generated by the wing as explained in Section 4.6. The loads thus estimate by using the direct pressure measurements and pressure from CVV are compared in Fig. 5.31.

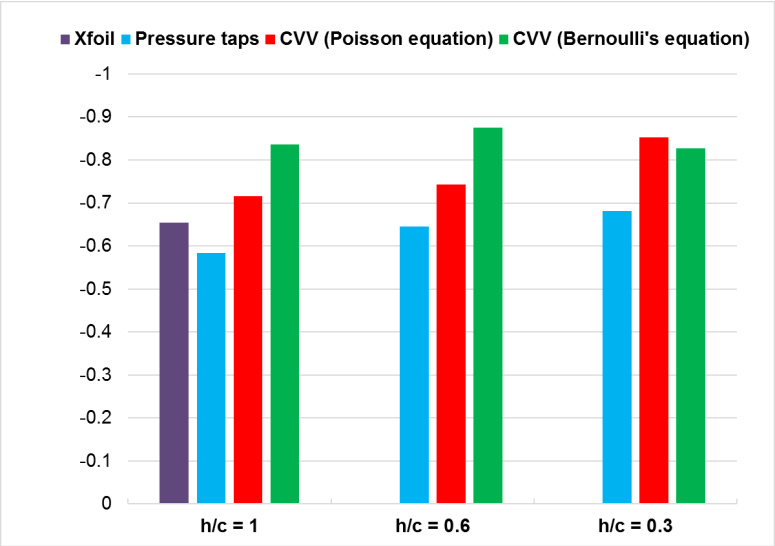

Figure 5.31: Comparison of C_L estimated from the pressure obtained by pressure taps and CVV pressure

We can observe that there is a discrepancy of about 15-20%, with the loads estimated from CVV being higher in all cases. This is also in agreement with the reasoning discussed above. The larger suction region in the case of CVV obtained pressure can be observed from the surface pressure distributions and is consistent for all configurations. The major contribution to this higher lift can be attributed to the region between 40-70% of chord length of the suction side. The pressure obtained using Bernoulli's equation is also higher on the pressure side of the wing, further adding to the loads generated and deviating from those calculated by the pressure taps data.

6

Conclusions and Recommendations

In this chapter, the concluding remarks for the work performed are summarized. Improvements to the technique and recommendations for further research in general are also suggested by the author.

6.1. Conclusions

A literature survey of aerodynamic experiments in wind tunnel emphasize on the importance of surface pressure measurements. Such measurements are helpful in giving an insight into the flow features around the model. The state-of-the-art technique for obtain surface pressure is direct measurements by incorporating pressure taps in the model and connecting them to pressure transducers. However, this makes the model design complicated and expensive. The pressure taps also need to placed appropriately in order to not have an intrusive effect on the flow and hence limit the spatial resolution of the flow. Apart from the direct pressure, a well-known indirect pressure measurement technique is by using PIV.

The use of planar PIV is widely reported in literature to reconstruct pressure from the obtained velocity field. By dividing the domain into multiple measurement planes, it is possible to obtain 2D3C velocity data. For obtaining volumetric 3D3C data, the technique of tomographic PIV was introduced by Elsinga et al., (2006). With the advent of HFSB(Caridi, (2017)), large scale measurements by particle tracking algorithms(Schanz et al., (2016)) became possible. Robotic CVV overcomes further obstacles of optical access and reduces the resources of time and computational power required to measure flow around large and complex geometries.

Making use of robotic CVV, a volumetric velocity field can be obtained, which can be further processed to obtain pressure using the Poisson equation. The present research was conducted with the following objective:

"Assess the feasibility of obtaining surface pressure using Coaxial Volumetric Velocimetry"

For fulfilling this objective, an experiment has been carried out using a wing in ground effect. The flow field is measured around the wing in different configurations of clearance using the robotic CVV system. The time averaged velocity field obtained is further processed to obtain the pressure field. For comparison and validation, direct pressure measurements are conducted using the pressure taps incorporated in the model.

The obtained results (surface pressure from CVV) are in good, but not complete agreement with those obtained from the pressure taps. The stagnation region is not represented accurately due to the bin size and ensemble averaging. The leading edge of the wing caused a significant reflection of the laser. The image processing based on Butterworth filter gets rid of the reflection, but also the slow moving particles in that region. The effect of this is clearly observed in the velocity field and is further propagated in the computation of pressure. Another problem observed is that of a slight difference in the flow. The soap bubbles making contact with the model, accumulate over the course of an acquisition and the deposition is observed to be enough to change the nature of boundary layer. However, these discrepancies are associated to the specifics of this experiment in particular and are not the attributes of the technique. A brief assessment of loads obtained by integrating the obtained pressure is also presented.

6.2. Recommendations

The conducted research gave a clear insight about the feasibility as well some limitations of the current technique. A few improvements for the same can be thought of and are presented.

This is the first experiment where this technique is used to obtain surface pressure. In the past the CVV system has been used mainly to study the flow features and wake flows. Hence, more work on the lines of obtaining surface pressure is encouraged for repeatability and versatility. Also, with hindsight and experience of the experiment, it is advised that extra care should be taken to avoid problems like those of reflections of laser, imaging through plexi-glass, slight differences in flow etc. For instance, a similar experiment can be conducted on a larger wing with high aspect ratio and placed in the open test section.

The process of binning can be improved in a number of ways. Most important change can be that of incorporating the model accurately to place the data accurately by making use of adaptive bins. Also, the computational efficiency can be improved by incorporating adaptive bins as larger bins can be used in regions of free stream flows while smaller ones can be used where there are sharp gradients in the flow.

With regards to the pressure reconstruction, the solver is found to be sensitive to boundary conditions. Even though the use of Neumann boundary conditions makes the solver robust and versatile for any type of flow, its particularly sensitive when the object is fully immersed as opposed to wake flows. A thorough study of the effect of such boundary conditions or even a different approach for pressure reconstruction is highly encouraged looking at the potential of the system. A method of defining the model in the volume for ensemble averaging will help to improve the application of boundary conditions at the surface of the model; something which can be incorporated while defining the adaptive bins mentioned above. The pressure obtained using Bernoulli's equation is in good agreement with the pressure taps data. It can also be concluded that if the flow conditions are known to be steady and irrotational and Bernoulli's equation remains valid, it is advisable to use it over the Poisson solver. Bernoulli's equation is free from issues like boundary conditions and is computationally much efficient. However, if the flow conditions are unknown, Poisson solver is suggested as it is robust for all types of flows.

Lastly, the HFSB hardware has been difficult to work with, especially in closed test section. The FSU has been unstable which in turn affects the quality of the bubbles produced. The seeding rake occasionally produces foam which is carried by the air and contaminates the model. This has an effect on the flow features around the model itself.

To conclude, the technique and the system is evaluated in terms of 'Technology Readiness Level'. Originally prescribed by National Aeronautics and Space Administration(NASA), it is a measure to judge the stage of development of a new system or technology. The technology readiness thermometer diagram is shown in Fig. 6.1, duplicated from European Space Agency, (2009). It describes the various levels of development in the life of a new technology, from conceptualisation to deployment in the market. The 'Technology Readiness Level Handbook' by European Space Agency, (2009) gives the detailed methodology behind such an assessment.

Using these guidelines, the readiness of the current technology can be said to be 'TRL 6'. The technique has been demonstrated in a few laboratory tests with various objectives(studying fow features, studying wake flows, reconstructing wake pressure and surface pressure). The pressure reconstruction part of the system has not been extensively tested and hence requires further tests in different applications to reach a certain confidence level to progress on the TRL scale.

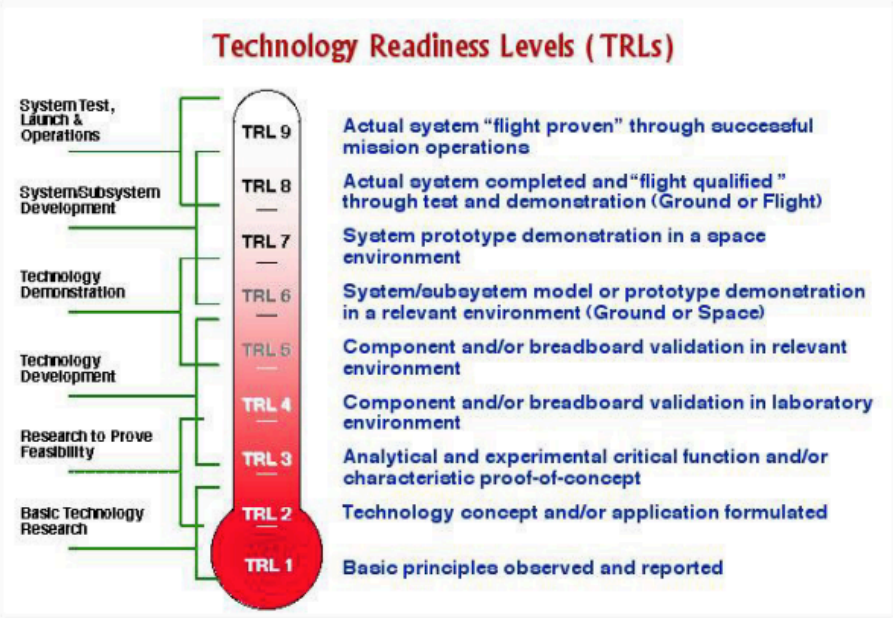

Figure 6.1: Technology Readiness Levels - Thermometer Diagram

Appendix A

Fig. A.1 shows the X-velocity contour obtained using planar PIV. In this case, the tracer particles were simply the minometric water-based fog particles. These particles have no effect on the surface of the wing (like contamination). It can be clearly seen that the flow separates after the region of maximum thickness.

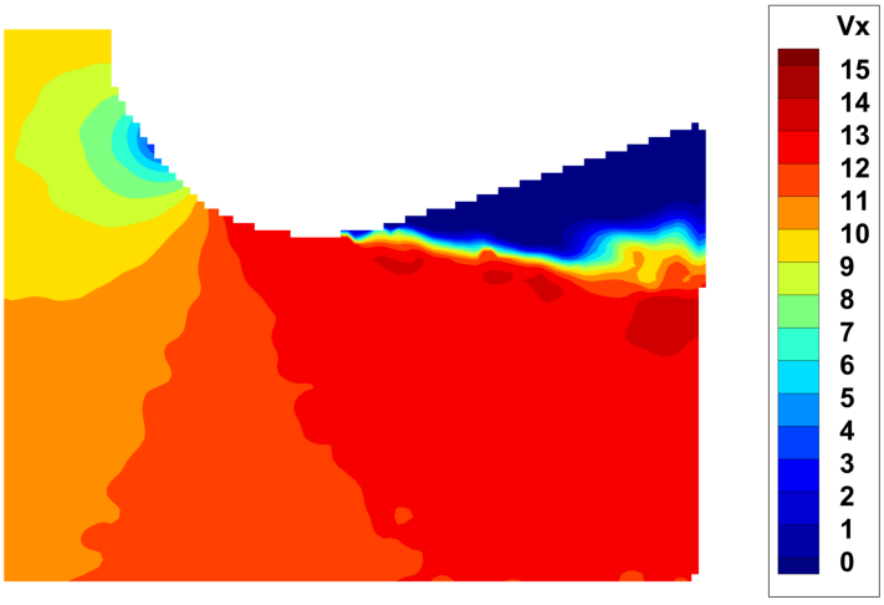

Figure A.1: X-velocity(u) contour obtained by planar PIV by simply using fog as tracer particles

However, when the same configuration is analysed when seeding HFSB and fog simultaneously, the flow is noticeably different and does not indicate any flow separation. Hence, to obtain comparable flows, the wing was equipped with a zigzag strip to trip the flow and help it to stay attached.

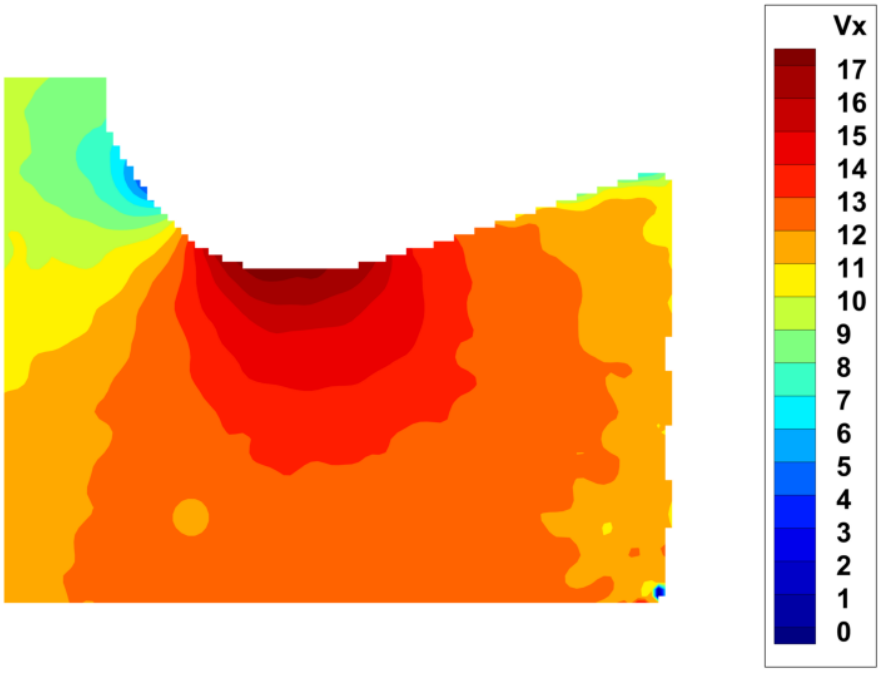

Figure A.2: X-velocity(u) contour obtained by planar PIV by simply using fog as tracer particles, but also seeding HFSB simultaneously

B

Appendix-B

The following table lists the normalised co-ordinates that define the airfoil cross-section of the wing used.

X	Y	X	Y
1.00000	0.00000	0.02915	-0.07484
0.96859	0.00234	0.04164	-0.08973
0.90789	0.00623	0.05738	-0.10490
0.83463	0.01024	0.07667	-0.11977
0.75555	0.01419	0.09973	-0.13353
0.67417	0.01809	0.12672	-0.14541
0.59195	0.02207	0.15794	-0.15475
0.51033	0.02626	0.19384	-0.16118
0.43004	0.03082	0.23480	-0.16428
0.35169	0.03605	0.28137	-0.16362
0.27623	0.04197	0.33407	-0.15886
0.20993	0.04738	0.39361	-0.14982
0.15891	0.05059	0.46043	-0.13686
0.12117	0.05136	0.53329	-0.12102
0.09265	0.05024	0.60874	-0.10358
0.07038	0.04776	0.68497	-0.08486
0.05249	0.04423	0.76160	-0.06513
0.03781	0.03994	0.83764	-0.04477
0.02563	0.03503	0.90959	-0.02500
0.01568	0.02923	0.96946	-0.00840
0.00803	0.02221	1.00000	0.00000
0.00280	0.01413		
0.00034	0.00535		
0.00010	-0.00358		
0.00127	-0.01313		
0.00347	-0.02359		
0.00699	-0.03500		
0.01222	-0.04734		
0.01949	-0.06064		

Bibliography

[1] R. Adrian. Scattering particle characteristics and their effect on pulsed laser measurements of fluid flow: speckle velocimetry vs particle image velocimetry. Applied optics, 1984.

[2] R. Adrian. *Twenty years of particle image velocimetry*. Experiments of fluids, 2005.

[3] European Space Agency. Technology readiness level handbook, 2009. URL `https://artes.esa.int/sites/default/files/TRL_Handbook.pdf`.

[4] N. Agüera, G. Cafiero, T. Astarita, and S. Discetti. Ensemble 3d ptv for high resolution turbulent statistics. Measurement Science and Technology, 2016.

[5] J. Anderson. *Fundamentals of Aerodynamics*. McGraw Hill Education Private Limited, India, 2015. ISBN 0-07-0070012-5.

[6] C. Atkinson and J. Soria. An efficient simultaneous reconstruction technique for tomographic particle image velocimetry. Experiments of fluids, 2009.

[7] D. Barker and M. Fourney. Measuring fluid velocity with speckle particles. Optics letters, 1977.

[8] P. Blinde, D. Michaelis, B. van Oudheusden, P. Weiss, R. de Kat, A. Laskari, Y. Jeon, L. David, D. Schanz, and F. Huhn. Comparative assessment of piv-based pressure evaluation techniques applied to a transonic base flow. 18th International Symposium on the Application of Laser and Imaging Techniques to Fluid Mechanics, Lisbon, Portugal, 2016.

[9] D. Cardano, G. Carlino, and A. Cogotti. Piv in the car industry: State-of-the-art and future perspectives. in: Particle image velocimetry. Topics in Applied Physics, vol 112. Springer, Berlin, Heidelberg. ISBN: 978-3-540-73528-1, 2008.

[10] G. Caridi. Development and application of helium filled soap bubbles for large scale piv experiments in aerodynamics. Delft University of Technology, 2017.

[11] M. Casper, C. Lemke, and U. Dierksheide. Piv in large wind tunnel by hfsb and stb. Topics in Applied Physics, vol 112. Springer, Berlin, Heidelberg. ISBN: 978-3-540-73528-1, 2016. URL `https://www.researchgate.net/profile/Uwe_Dierksheide/project/large-scale-particle-image-velocimetry/Accessedon29-11-2018`.

[12] D. Celaya. Time-averaged pressure from robotic volumetric piv. Delft University of Technology, 2018.

[13] R. Dominy. Aerodynamics of grand prix cars. Proceedings of the Institution of Mechanical Engineers, Part D: Journal of Automobile Engineering, 1992.

[14] T. Dudderar and P. Simpkins. Laser speckle photography in a fluid medium. Nature, 1977.

[15] T. Ebbers and G. Farneback. Improving computation of cardiovascular relative pressure fields from velocity mri. Journal ofMagnetic Resonance Imaging, 2009.

[16] G. Elsinga, F. Scarano, B. Wieneke, and B. van Oudheusen. Tomographic particle image velocimetry. Experiments in fluids, 2006.

[17] D. Giaquinta. The flow topology of ahmed body. Delft University of Technology, 2018.

[18] R. Grousson and S. Mallick. Study of flow pattern in a fluid by scattered laser light. Applied optics, 1977.

[19] R. Gurka, A. Liberzon, D. Hefetz, D. Rubinstein, and U. Shavit. Computation of pressure distribution using piv velocity data. 3rd Int. Workshop on Particle Image Velocimetry (Santa Barbara) pp671-6, 1999.

[20] G. Herman and A. Lent. Iterative reconstruction algorithms. Computers in biology and medicine, 1976.

[21] J. Hoffmann. *Numerical Methods for Engineers and Scientists*. McGraw-Hill Inc., New York, 1992. ISBN 0-8247-0443-6.

[22] M. Jahanmiri. Pressure sensitive paints : The basics & applications division of fluid dynamics. Chalmers University of Technology, 2014.

[23] C. Jux. Robotic volumetric particle tracking velocimetry. Delft University of Technology, 2017.

[24] J. Kahler, S. Scharnowski, and C. Cierpka. On the resolution limit of digital particle image velocimetry. Experiments of Fluids, 2012.

[25] J. Katz. *Race Car Aerodynamics : Designing for Speed*. Bentley Publishers, Cambridge, MA, USA, 1995. ISBN 0-8376-0142-8.

[26] B. McLachlan and J. Bell. Pressure-sensitive paint in aerodynamic testing. Experimental Thermal and Fluid Science, 1995.

[27] A. Melling. Tracer particles and seeding for particle image velocimetry. Measurement science and technology, 1997.

[28] R. Meynart. Instantaneous velocity filed measurements in unsteady gas flow by specle velocimetry. Applied optics, 1983.

[29] Y. Murai, T. Nakada, T. Suzuki, and F. Yamamoto. Particle tracking velocimetry applied to estimate the pressure field around a savonius turbine. Measurement science and technology, 2007.

[30] M. Nakagawa, F. Michaux, S. Kallweit, and K. Maeda. Unsteady flow measurements in the wake behind a wind tunnel car model by using high speed planar piv. Experiments of Fluids, 2015.

[31] M. Nakagawa, S. Kallweit, F. Michaux, and T. Hojo. Typical velocity fields and vortical structures around a formula one car, based on experimental investigations using particle image velocimetry. SAE International Journal of Passenger Cars - Mechanical Systems, 2016.

[32] K. Nakakita, M. Kurita, K. Mitsuo, and S. Watanabe. Practical pressure-sensitive paint measurement system for industrial wind tunnels at jaxa. Measurement Science and Technology, 2006.

[33] Delft University of Technology. W-tunnel. https://www.tudelft.nl/lr/organisatie/afdelingen/aerodynamics-wind-energy-flight-performance-and-propulsion/facilities/low-speed-wind-tunnels/w-tunnel/, 2018.

[34] M. Raffel, C. Willert, J. Werely, and S. Kompenhans. *Particle Image Velocimetry - A practical guide*. Springer Science & Business media, Berlin Heidelberg, second edition, 2007. ISBN 978-3-540-72308-0.

[35] D. Ragni, A. Ashok, B. van Oudheusen, and F. Scarano. Surface pressure and aerodynamic loads determination of a transonic airfoil based on particle image velocimetry. Measurement science and technology, 2009.

[36] G. Russo. *Aerodynamic Measurements*. Woodhead Publishing Limited, 80 High Street, Sawston, Cambridge CB22 3HJ, UK, 2011. ISBN 978–0–85709–368–8.

[37] F. Scarano. Tomographic piv: principles and practice. Measurement science and technology, 2013.

[38] F. Scarano. Experimental aerodynamics (course reader for flow measurement techniques). Delft University of Technology, 2013b.

[39] F. Scarano, s. Ghaemi, G. Caridi, J. Bosbach, U. Dierksheide, and A. Sciaccitano. On the use of helium filled soap bubbles for large scale tomographic piv in wind tunnel experiments. Experiments in fluids, 2015. ISSN 1432-1114.

[40] D. Schanz, S. Gesemann, A. Schröder, B. Wieneke, and M. Novara. Non- uniform optical transfer functions in particle imaging: calibration and application to tomographic re- construction. Measurement Science and Technology, 2012.

[41] D. Schanz, S. Gesemann, and A. Schroder. Shake-the-box: Lagrangian particle tracking at high particle densities. Experiments of Fluids, 2016.

[42] J. Schneiders. Bridging piv spatial and temporal resolution using governing equations and development of the coaxial volumetric velocimeter. Delft University of Technology, 2017.

[43] J. Schneiders and F. Scarano. Dense velocity reconstruction from tomographic ptv with material derivatives. Experiments of Fluids, 2016.

[44] J. Schneiders, G. Caridi, A. Sciacchitano, and F. Scarano. Large-scale volumetric pressure from tomographic ptv with hfsb tracers. Experiments of Fluids, 2016.

[45] A. Sciacchitano and F. Scarano. Elimination of piv light reflections via a temporal high pass filter. Measurement Science and Technology, 2014.

[46] A. Sciacchitano, C. Jux, J. Schneiders, and F. Scarano. Robotic volumetric piv of a full-scale cyclist. Experiments in Fluids, 2018.

[47] S. Soloff, R. Adrian, and Z. Liu. Distortion compensation for generalized stereo- scopic particle image velocimetry. Measurement Science and Technology, 1997.

[48] W. Terra, A. Sciacchitano, and F. Scarano. Evaluation of aerodynamic drag of a full-scale cyclist model by large-scale tomographic-piv. International Workshop on Non-Intrusive Optical Flow Diagnostics: Delft, The Netherlands, 2016.

[49] B. van Oudheusen. Piv-based pressure measurement. Measurement science and technology, 2013.

[50] B. Wieneke. Volume self-calibration for 3d particle image velocimetry. Experiments in fluids, 2008.

[51] B. Wieneke. Iterative reconstruction of volumetric particle distribution. Experiments of fluids, 2012.

[52] N. Worth and T. Nickels. Acceleration of tomo-piv by estimating the initial volume intensity distribution. Experiments of fluids, 2008.

[53] J. Zerihan and X. Zhang. Aerodynamics of a single element wing in ground effect. Journal of Aircraft, 2000.